
UNIVERSITEIT VAN PRETORIA
UNIVERSITY OF PRETORIA
YUNIBESITHI YA PRETORIA

SCHOOL OF ENGINEERING

DEPARTMENT OF MECHANICAL AND AERONAUTICAL ENGINEERING

# Local heat transfer coefficients in an annular passage with flow turbulation

By

Rowan Marthinus Steyn

Submitted in partial fulfilment of the requirements for the degree of

Master of Engineering

In the Department of Mechanical and Aeronautical Engineering in the Faculty of Engineering, Built Environment and Information Technology

UNIVERSITY OF PRETORIA

1 December 2019

Supervisors: Prof J Dirker and Prof JP Meyer

# Abstract


Author: Rowan Marthinus Steyn

Student number: 12067564

Supervisors: Prof J Dirker, Prof JP Meyer

Department: Mechanical and Aeronautical Engineering

Degree: Master of Engineering (Mechanical Engineering)



In this experimental and numerical investigation, the use of flow turbulation was considered as a method to increase local heat transfer coefficients in annular heat transfer passages. Experimental data was obtained for cases with and without inserted ring turbulators within a horizontal annular test section using water for average Reynolds numbers ranging from 2000 to 7500 and average Prandtl numbers ranging from 6.73 to 6.79. The test section was heated uniformly on the inner annular wall and had a hydraulic diameter of 14.8mm, a diameter ratio (inner wall diameter to outer wall diameter) of 0.648, and a length to hydraulic diameter ratio of approximately 74. A set of circular cross sectioned ring-type turbulators were used which had a thickness of 1mm, a ring diameter of 15.1mm and a pitch of 50mm. It was found that the presence of the flow turbulators increased the average Nusselt number by between 33.9% and 45.8%. The experimental tests were followed by numerical simulations to identify the response in the heat transfer coefficient by changing the geometry of the turbulators. For this, the turbulator diameters were ranged from 0.5 mm to 2 mm, and the gap size (between the inner wall and a turbulator ring) ranged from 0.125 mm to 4 mm at a pitch of 50 mm. The results showed that the use of turbulators increased the Nusselt numbers by a maximum of 34.8% and that the maximum can be achieved for a turbulator diameter of 2 mm and a gap size of 0.25 mm, for all the Reynolds numbers tested. From the numeric determined pressure drop values it was found that the smaller gap size had the lowest pressure drop and the smallest turbulators also produced the lowest pressure drop.

# Acknowledgments

A special thanks to the South African Centre for High Performance Computing (CHPC) for allowing the use of their facilities throughout the duration of this thesis.

I thank Professor Dirker for his time and patience in the course of this work.

# Table of Contents

# List of tables



# List of figures

# Nomenclature

| | | |
|---|---|---|
| $A$ | $m^2$ | Surface area |
| $a$ | - | Annular diameter ratio |
| $C$ | - | Coefficient in power law relation equations |
| $C_p$ | J/kg K | Specific heat capacity |
| $D$ | m | Diameter |
| $d$ | m | Turbulator diameter |
| $EB$ | - | Energy balance error |
| $G$ | m | Smallest gap distance between turbulator and wetted surface |
| $H$ | m | Channel height |
| $h$ | $W/m^2K$ | Convection heat transfer coefficient |
| $I$ | A | Electric current |
| $k$ | W/mK | Thermal conductivity |
| $L$ | m | Length |
| $m$ | - | Generic exponent in power law relation equations |
| $n$ | - | Generic exponent in power law relation equations |
| Nu | - | Nusselt number |
| Pr | - | Prandtl number |
| $\dot{Q}$ | W | Heat transfer rate |
| $\dot{q}$ | $W/m^2$ | Heat flux |
| $R$ | K/W | Thermal resistance |
| Re | - | Reynolds number |
| $T$ | K | Temperature |
| $U$ | $W/(m^2K)$ | Overall heat transfer coefficient |
| $u^+$ | - | Dimensionless velocity for wall bounded flow |
| $V$ | V | Electric voltage potential |
| $v$ | m/s | Velocity |
| $x$ | m | Local axial distance |
| $y^+$ | - | Dimensionless wall distance for wall bounded flow |

# Greek symbols

| | | |
|---|---|---|
| $\in$ | - | Heat transfer enhancement factor |
| $\mu$ | kg/m.s | Dynamic viscosity |
| $\rho$ | $kg/m^3$ | Density |
| $\nu$ | $m^2/s$ | Kinematic viscosity |
| $\Theta$ | degrees | Radial angle |

## Subscripts

| | |
|---|---|
| $a$ | Annulus |
| $avg$ | Average value |
| $b$ | Bulk fluid value |
| $cond$ | Conduction |
| $conv$ | Convection |
| $elec$ | Electric heater |
| $h$ | Hydraulic |
| $HS$ | Heated Surface |
| $in$ | Inlet |
| $loss$ | Lost energy |
| $N$ | Numerical value |
| $out$ | Outlet value |
| $s$ | Surface |
| $therm$ | Thermal |
| $wall$ | Wall location |
| $ws$ | Wetted surface in contact with fluid |
| 1 | Outer annular wall |
| 2 | Inner annular wall |
| $\infty$ | Free stream |

# 1. Introduction

## 1.1. Background

The study of sensible heat transfer in thermal systems is important due to its relevance to many industrial applications. In essence, sensible heat transfer can be defined as the transfer of energy due to the existence of a temperature gradient. Of the three heat transfer modes; namely conduction, convection, and radiation heat transfer; convection heat transfer is of specific importance in many thermal-flow devices which operate with moving fluids. This is of particular interest to heat exchangers where energy is transferred from one fluid to another without mixing. Several heat exchanger types exist, including, but not limited to plate, shell-and-tube, helical coil and spiral heat exchangers. Ideally heat exchanger should sustain desired heat transfer rates between the intended fluids while mitigating pressure drop losses and unintended heat loss to or heat gain from the environment. Due to the impact which heat exchanger dimensions have on material cost, small dimensional sizes are preferred. For this reason, high convective heat transfer coefficients (defined as the heat flux per temperature difference between the fluid and the heat transfer wall) is sought in order to reduce the required surface area within a heat exchanger. Such improvements are, however, often accompanied by an increase in the operational pressure drop which requires increased pumping power to maintain fluid motion. As such, thermal engineers might need to perform trade-offs between heat transfer efficiency and minimised pressure losses. Studies dedicated to the characterisation of these attributes could assist in providing information to better optimise heat exchanger designs.

The design of heat exchangers usually starts with process conditions such as stream conditions, temperatures, pressures, and mass flow rates. Using these values and the type of heat exchanger, the overall heat transfer coefficient ($U$) is calculated which is related to the convective heat transfer coefficients, surface areas, and wall thermal resistance. To increase the thermal performance of heat exchanging equipment, one needs to increase the heat exchangers surface area, or the fluid temperature differences, or increase the heat transfer coefficients. Several methods exist with which to increase the convective heat transfer coefficient in a flow passage. These can be divided between active or passive techniques. Active techniques include systems that utilise mechanical means such as the spinning of a surface, surface vibration and fluid oscillation; and require additional external power for operation. Passive techniques on the other hand, do not require additional active power and often rely on a modification of the surface area or geometry which results in increased fluid residence time, or thermal boundary layer disturbance. For instance, extended surfaces using fins can increase the surface area while flow passage geometries that encourage fluid swirling increases the fluid residence time and inhibits the boundary layer development.

Another passive method for influencing the convection heat transfer coefficient (and which is the focus of this study) is the use of turbulation devices which disturb the boundary layer. Such turbulation devices, placed intentionally within the flow field, may result in flow eddies forming. These eddy currents influence the boundary layer, and which can result in an increase of the convective heat transfer coefficient.

Flow turbulators come in many different types; such as helical flow inserts, petal-shaped fins, straight and twisted internal fins, and coil inserts (among others). These can be employed in some form or another in most types of heat exchangers. Unfortunately, the addition of turbulators, in which ever heat exchanger type, also usually result in increased pressure drop.

Among the various types of heat exchangers in existence, tube-in-tube heat exchangers are commonly used in many industries because of their simplicity of design, and their relative ease of construction. For these heat exchangers, the flow and thermal characteristics of the annular passage, constituted by the volume between the inner and outer tube, are important.

Several experimental and numerical investigations have been conducted to measure and predict the annular internal heat transfer coefficients, and the effective adiabatic and diabatic friction factors. A number of heat transfer enhance methods for annular passages have also been investigated. These include coil-wire inserts, internal fin inserts, petal-shaped finned tubes, and twisted tapes. Such efforts have resulted in better understanding of the local heat transfer behaviour and improved heat transfer prediction equations and design procedures. However, there are several other flow turbulation enhancement methods that have not yet been fully explored, including suspended turbulator rings.

By introducing turbulation rings close, but not in direct contact with either the inner or outer walls of an annular space (see Figure 1), an advantageous thermal-hydraulic condition can be created which may result in significantly enhanced heat transfer ability, but at acceptable pressure drop penalties. By varying the radial location, and cross-sectional ring material diameter, as well as the axial distance between consecutive rings, different heat transfer and pressure drop performances can be obtained.

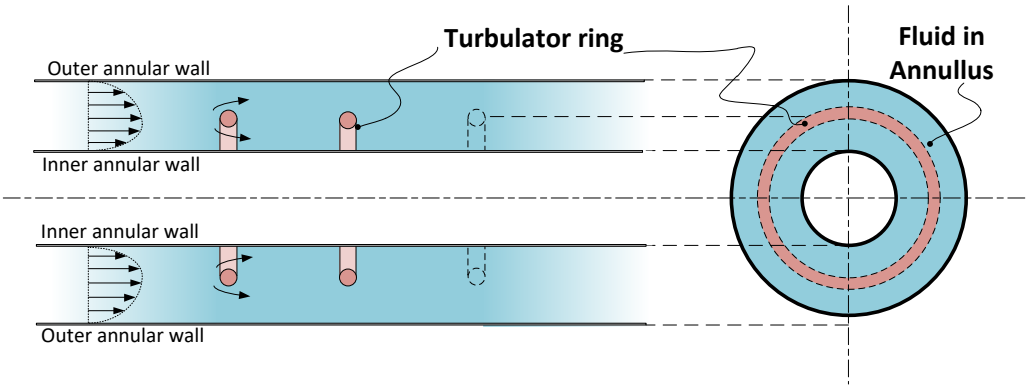


Figure 1: Schematic representation of circular cross sectional turbulator rings in an annular flow passage.

## 1.2. Problem statement

Even though studies on turbulators exist to increase heat transfer coefficients, relatively little research has been done on turbulators within annular spaces, and none has been on cylindrical cross-sectional turbulator rings within an annulus. Therefore, a need exists to perform an investigation into the heat transfer coefficients characterisation in annular passages with turbulator rings.

## 1.3. Objectives

The objectives of this study are to:

1. Design and construct a set of turbulator ring inserts for use within an existing annular flow passage test section.
2. Gather steady state experimental data for cases with and without the turbulator insert with the aim of deriving the local heat transfer coefficients where the flow is in the low turbulent regime.
3. Develop numerical simulation models to characterise the heat transfer enhancement effect of ringed flow turbulators in a horizontal annular flow passage for a range of dimensional sizes and flow conditions.
4. Describe the impact that a change of geometrical parameters will have on the average and local heat transfer coefficients.

## 1.4. Dissertation layout

Chapter 2 presents a review of literature relevant to the study and covers aspect such as heat transfer definitions, background into turbulators and annular flow passages, as well as relevant previous investigations on similar topics. Chapter 3 contains information relating to the experimental facility, test section, and the procedures followed during the experimental investigation. Chapter 4 describes the data reduction method and presents the results from the experimental investigation. Chapter 5 presents a description of the numerical test domain. Chapter 6 contains the results of the numerical investigation, including mesh independence and optimisation trends. Chapter 7 concludes the dissertation and supplies a summary and the overall findings.

# 2. Literature review

## 2.1. Introduction

In this chapter, previous research in the field of heat transfer using turbulation devices is reviewed. An overview is also presented of the work done on annular flow passages. This includes correlations and findings from both fields of research to date. The chapter starts with a short review on the mechanisms of heat transfer in order to familiarise the reader with some of the terms used in the rest of this document.

## 2.2. Heat transfer definitions

A prominent method of heat transfer is through convection. It occurs between a fluid and a surface, and is due to bulk fluid motion of a fluid, without which heat transfer will occur purely via conduction. Compared to conduction heat transfer, convection heat transfer can significantly increase the operating heat transfer rate. This convective heat transfer rate ($\dot{Q}_{conv}$) can be described by means of Newton's law of cooling:

$$\dot{Q}_{conv} = hA_s(T_s - T_\infty) \tag{1}$$

Here $h$ is the convection heat transfer coefficient, $A_s$ is the heat transfer surface area, $T_s$ the surface temperature and $T_\infty$ is the bulk fluid temperature. The convective heat transfer coefficient is not a property of the fluid but is determined experimentally and is dependent on parameters such as the geometry and the relative fluid velocity, thermo-physical fluid properties and the thermal boundary condition, among others.

The convection heat transfer coefficient is often represented non-dimensionally via the Nusselt number ($\mathrm{Nu}$). This number is the ratio of the convective heat transfer to the conductive heat transfer. When substituted, the Nusselt number for a flow passage is obtained as is described in Equation 2. Thus, the Nusselt number represents the enhancement of heat transfer due to convection compared to a case where only conduction heat transfer is present.

$$\mathrm{Nu} = \frac{hD_h}{k} \tag{2}$$

Here $k$ is the fluid thermal conductivity and $D_h$ is the characteristic diameter of the flow passage, referred to as the hydraulic diameter $\left(D_h = \frac{4 \times flow\ area}{wetted\ perimeter}\right)$.

Also, of interest is the Reynolds number ($\mathrm{Re}$) which is defined as the ratio between of the inertia forces over the viscous forces in a fluid. For internal flow it can be written in terms of the fluid density ($\rho$), average cross-sectional velocity ($v$), the hydraulic diameter ($D_h$) and the dynamic viscosity ($\mu$):

$$\mathrm{Re} = \frac{\rho v D_h}{\mu} \tag{3}$$

The Reynolds number can be used to determine the dominant flow regime. The flow can be laminar, turbulent or in transition between laminar and turbulent. Generally the flow in a circular tube is

laminar when Re < 2300 and fully turbulent when Re > 10 000, although turbulence is dependent on other parameters. For other flow passages, the transition between the flow regimes can occur at different Reynolds number ranges, depending on the characteristic diameter definition and the influence of the passage geometry on the velocity flow field.

Another important non-dimensional number is the Rayleigh (Ra) number, associated with buoyancy driven flow. The Rayleigh number has a qualitative relationship describing the buoyancy and viscosity within a fluid. Heat transfer will be dominated by conduction if the Rayleigh number is below a certain critical number and will be primarily in the form of convection if above the critical number. The Rayleigh number is defined in Equation 4.

$$\mathrm{Ra} = \frac{\beta g \Delta T D_h^3}{\nu \alpha} \tag{4}$$

Here $\beta$ is the thermal expansion coefficient, $g$ is the gravitational acceleration, $\nu$ is the kinematic viscosity, and $\alpha$ is the thermal diffusivity.

The Richardson number (Ri), which is another useful dimensionless quantity when considering buoyancy driven flow, is expressed as the ratio of natural convection to forced convection.

$$\mathrm{Ri} = \frac{g\beta(T_s - T_b)D_h}{v^2} \tag{5}$$

Here $T_s$ is the surface temperature, $T_b$ is the bulk fluid temperature and $v$ is the characteristic velocity. Natural convection is typically negligible when $\mathrm{Ri} > 0.1$ and forced convection is negligible when $\mathrm{Ri} > 10$.

Also, of importance is the Prandtl number (Pr) which describes the relative thickness of the velocity and thermal boundary layers. Equation 6 supplies the Prandtl number definition where $c_p$ is the fluid's specific heat capacity.

$$\mathrm{Pr} = \frac{\mu c_p}{k} \tag{6}$$

With liquid water for instance, the Prandtl number is in the order of 10, which indicates that the heat diffuses much quicker than in oils which have Prandtl numbers as high as 40 000. A large Prandtl number is indicative of a thinner thermal boundary layer compared to the velocity boundary layer.

## 2.3. Boundary layer theory

In order to better understand convection heat transfer, boundary layer theory has been developed to describe fluid flow over a surface. The velocity boundary layer consists of an inner and outer layer with an overlapping layer between the two. The inner layer operates with viscous shear that dominates the flow while the outer layer is dominated by turbulent shear. The overlap layer has a profile that smoothly connects the inner and outer layers. The boundary layers are represented with dimensionless parameters that describe the velocity and wall distance ($u^+$ and $y^+$ respectively). $y^+$ is defined in Equation 7 and $u^+$ is defined in Equation 8.

$$y^+ = \frac{yu_t}{v} \tag{7}$$

Here $y$ is the normal distance from the wall, $u_t$ is the shear velocity and $v$ is the local kinematic viscosity.

$$u^+ = \frac{1}{\kappa}\ln(y^+) + C^+ \tag{8}$$

where $\kappa = 0.41$ is the Von Karman experimental constant and $C^+ = 5$ is a constant for smooth walls.

Figure 2 shows the behaviour of the turbulent boundary layer in terms of the dimensionless numbers $u^+$ and $y^+$. The inner layer consists of a viscous sublayer, a buffer region, and the overlap layer. It is important that these layers are modelled correctly in numerical simulations because the boundary layer has a direct impact on heat transfer.

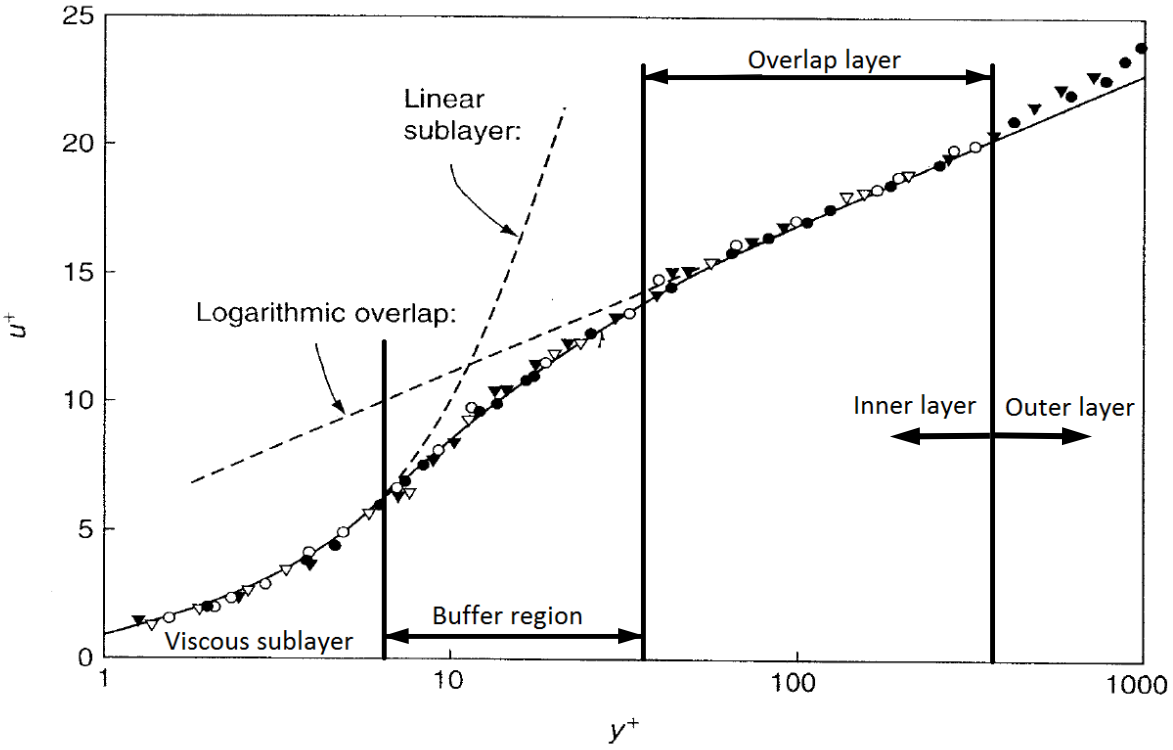


Figure 2: Dimensionless velocity profile of near wall boundary layer (Frank, 2006).

The region between $5 \leq y^+ \leq 30$ is called the buffer region where the velocity profile is neither linear nor logarithmic and is more of a smooth blend between the two. The linear region and logarithmic region is described by two different formulas, while an equation exists that provides a continuous expression for the inner layer, shown in Equation 9 (Spalding, 1960):

$$y^+ = u^+ + e^{-\kappa B}\left(e^{\kappa u^+} - 1 - \kappa u^+ - \frac{(\kappa u^+)^2}{2} - \frac{(\kappa u^+)^3}{6}\right) \tag{9}$$

where $B \approx 5$ as derived from experimental results.

The boundary layer is responsible for the velocity profiles within flow passages. As the boundary layer grows, the flow velocity becomes retarded close to the wall thereby accelerating the flow in the core.

As mentioned earlier, the thickness of a boundary layer is dependent on the wall shear stress, the fluid density and viscosity. A thicker boundary layer in turn has a thicker laminar layer close to the wall. This hinders convective heat transfer because there is little turbulence in the laminar region. As such the thermal conductivity of the fluid will dominate heat transfer. Initially, during its developing stage, the thermal boundary layer is thin which allows for high heat transfer rates. However, as the boundary layer becomes more developed and thicker, the rate of heat transfer decreases.

By computing the mean velocity in turbulent pipe flow and by using boundary layer theory, a direct relationship has also been found to exist between the equations describing the boundary layer and the friction factor calculations in smooth walled pipes. The pressure drop which occurs in turbulent pipe flow is related to the surface roughness because rougher surfaces will interfere with the sublayer, creating more turbulence.

Because fluid and wall interactions can be complicated in engineering problems, correct boundary layer treatment is one of the most important aspects in computational fluid dynamic (CFD) simulations. CFD, which was initially dedicated to the aerospace and aeronautical industry, has found application in many other industries. A number of commercial and open source software packages have become available to solve fluid flow problems. These packages are commonplace for fluid flow research and can provide insight to experimental results.

In engineering applications, solving the continuity, momentum and energy governing equations directly for fluid flow are only useful for a limited number of flow problems and do not hold for complicated flow. Traditionally the most common approach was to use experimental data to obtain some simplified dimensionless parameter of interest. Such experimental efforts can be costly, and CFD is commonly used to complement experimental investigations. Unfortunately, near-wall modelling remains a challenge, and numerical predictions using CFD cannot replace experimental work completely.

Turbulent flow a commonly encountered in many engineering applications and requires special numerical modelling. Turbulence has been described as an energy cascade where turbulence consists of eddies. Large eddies would break up and transfer its energy to smaller sized eddies which would continue until the smallest possible eddy size is reached. The most popular method used to model turbulence is by using Reynolds-averaged Navier-Stokes (RANS) equations. Due to the rapidly varying random fluctuations in turbulent flow, RANS equations are written in terms of time averaged turbulent variables. In RANS modelling the term turbulence kinetic energy ($k$) is characterised by the average kinetic energy per unit mass associated with eddies and is quantified by velocity fluctuations. The rate of dissipation of turbulent kinetic energy per unit mass ($\epsilon$) is described as the rate at which turbulence kinetic energy is converted into internal thermal energy. Because several turbulence models have been created to predict turbulent flow, it is important to know which models perform well for certain problems.

The most popular turbulence models are listed and briefly described below:

- The standard $k-\epsilon$ model is well established, however it is not suited when large and rapid strains are present in the flow.
- Re-Normalisation Group (RNG) $k-\epsilon$ model is a more sophisticated model compared to the standard $k-\epsilon$ model and has been found to give more accurate results when simulating unsteady flow from forced convection to mixed convection (natural and forced convection) (Gao, et al., 2017).
- The $k-\omega$ SST turbulence model has shown great accuracy in external flow over air foils due to its ability to resolve flow down to the viscous part of the boundary layer.
- The Reynolds Stress Model (RSM) has six additional equations to compute the turbulent stresses and has shown good results in flow with large flow strain, but overall success has been moderate.
- Large Eddy Simulation (LES) resolves the large scales of turbulent eddys which is very computationally expensive and is generally used as a research tool instead of an engineering one.

None of the developed turbulence models are applicable to all flow conditions due to the complexity of turbulent flow. A major challenge with modelling turbulence is that there is commonly a lack of knowledge of the proper boundary conditions that need to be applied to flow fluid domain walls. The variations of $k$ and $\epsilon$ are very rapid near the walls, so it is not easy to choose suitable values in the wall region.

As known from the boundary layer, the velocity decreases as it approaches the wall, this includes decreasing the fluctuating components of velocity that is considered turbulence. Turbulence models can make use of either near wall modelling to model the boundary layer, or to use wall functions to model the boundary layer. At high Reynolds numbers, the viscous sublayer becomes very thin and it becomes computationally expensive to use near wall modelling to resolve the boundary layer. This problem can be addressed by using wall functions which model the turbulent boundary layer by superimposing the theoretical boundary layer profiles on the wall.

Problems arise with most wall functions when the fist grid point is not in the logarithmic region (see Figure 2) when $y^+ > 30$. This is due to the high turbulence production at approximately $y^+ = 12$, which is dependent on the Reynolds number, making modelling in this buffer region very difficult and is generally avoided (Moukalled, et al., 2016). Other issues are faced when flow separates, reattaches or within recirculation regions.

Although CFD turbulence models do not always produce exactly the same results as seen in experimental results, it has been noted that optimisation can take place using CFD (Ferziger & Peric, 2002), where relative performance comparisons from simulated data is utilised. As such, numerical simulations (which may or may not require turbulence models) can drastically reduce the number of experimental tests required for optimisation.

## 2.4. Annular flow passages

### 2.4.1. Background

Tube-in-tube heat exchangers are used in many industries as a relatively inexpensive method of exchanging heat. This type of heat exchanger is characterised by two concentric tubes where one fluid flows in the smaller inner tube and another fluid flows in the annular space between the two tubes. Figure 3 shows sectioned diagrams of a counter-flow tube-in-tube heat exchanger with the annular passage inlet and outlet both being perpendicular to the length of the heat exchanger. Important geometric parameters include the inner tube diameter ($D_1$), the outer tube diameter ($D_2$), the inlet diameter ($D_{inlet}$), the annular passage tube's wetted surface length ($L_{ws}$), the annular diameter ratio $\left(a = \frac{D_1}{D_2}\right)$, and the annulus hydraulic diameter ($D_h = D_2 - D_1$).

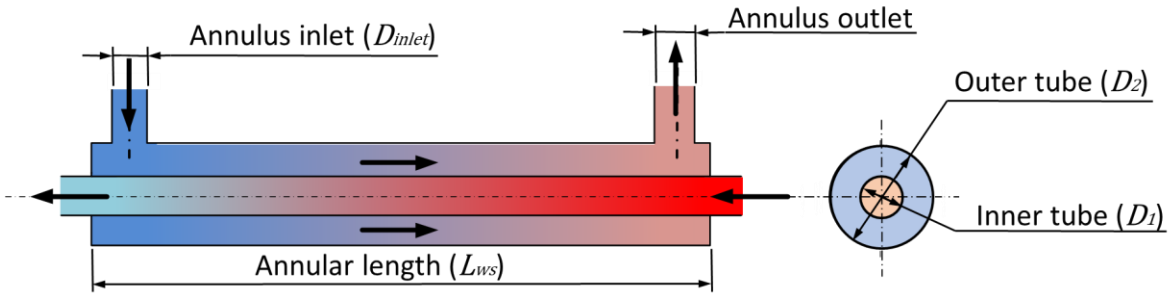


Figure 3: Schematic (sectioned views) of a counter-flow double pipe heat exchanger.

For single phase applications, and due to heat transfer, there is a change in the bulk fluid temperatures along the flow passages (inner tube and annulus). Because these bulk fluid temperature changes are not necessarily linear, it can present a challenge when attempting to determine local heat transfer coefficients along the axial direction of the heat exchanger. To overcome this, it is often preferred to impose a convenient boundary condition on the inner wall of the annulus. Constant heat flux or a constant wall temperature conditions are frequently used. In the case of a uniform heat flux boundary condition, and in the absence of other heat losses or additions, the bulk fluid temperature in the passage assumes a linear relationship.

### 2.4.2. Previous investigations

Annular passages have been studied significantly. In the early years, methods with which to predict heat transfer in double pipe heat exchangers have been developed by using simple mathematical models validated by experimental measurements (Mozley, 1956). Analysis of fully developed laminar flow has been made, which produced good analytical agreement with experimental measurements (Lundberg, et al., 1963). A number of different parameters have been considered, including the effect of the flow regime (laminar vs turbulent), passage orientation, geometric sizes, and fluid properties.

The flow can be forced convection, natural convection or mixed convection depending on the absence or dominance of buoyancy driven flow. Mixed convection in horizontal annuli in the transitional flow

regime region (for instance, $2\,200 < \mathrm{Re} < 5\,000$) have exhibited complicated flow where turbulent flow exists in the upper regions of the flow passage and laminar in the bottom regions, which may lead to different heat transfer coefficients around the annulus (Ciampi, et al., 1987).

Islam *et al.* (2001) performed numerical and experimental investigations of steady state laminar flow with mixed convection for Reynolds numbers between 200 and 1 000, with special attention to the entrance region of a horizontal annulus. Numerical results showed that secondary flow produced a local increase in the Nusselt number near the entrance, which unfortunately could not be studied in detailed experimentally due to limitations of the facility used. It was suggested that the increased heat transfer coefficients were due to a deceleration of flow in the upper part of the annulus and an acceleration in the lower part of the annulus. This phenomenon intensifies with increasing Rayleigh numbers.

Francis *et al.* (2002) assessed the ability of a computational fluid dynamics code to reproduce experimental results of fully developed natural convection within a horizontal annulus. For high Rayleigh numbers, stagnation regions were found to be present near the top of the annulus with turbulent flow moving upward above the inner cylinder. It was also found that the selection of the RNG $k - \epsilon$ turbulence model was appropriate when considering natural convection heat transfer and fluid flow in the annulus.

Yeh (2002) investigated natural convection inside a horizontal annulus with open ends. One of the findings was that the maximum inner cylinder surface temperature occurs at the top of the cylinder. This is important to note as this characteristic for natural convection can be found when natural convection has a dominant role in the convective forces.

Dirker and Meyer (2005) investigated the heat transfer in smooth concentric annuli for a Reynolds number of 2 600 to 35 000 in a counter flow arrangement and found that the relationships and results given by other researchers had large discrepancies when compared to each other. To improve on the existing correlations, new data, with improved levels of accuracy, was gathered to predict the heat transfer for annular diameter ratios between 0.313 and 0.588. A new correlation was proposed which produced predictions within 3% of the experimental results.

Lu and Wang (2008) performed experiments at three different annulus inclinations (horizontal flow, upward flow and downwards flow) for Reynolds numbers between 10 and 30 000. Some results showed that the transition from laminar to turbulent flow occurred much earlier than for flow in circular tubes. The Reynolds number transition range was found to be between 800 to 1 200. It was also found that a narrow annulus achieved higher heat transfer coefficients in the turbulent region.

Swamee (2008) used previous correlations to formulate an optimum design of a double pipe heat exchanger. The objective function of this optimisation process is to maximise the heat transfer while minimising the pressure drop. This method could be employed with the addition of turbulators in future design optimisation problems.

Neto *et al.* (2011) used CFD to simulate turbulent flow in concentric and eccentric annuli with and without inner shaft rotation for a Reynolds number of 26 600 and a hydraulic diameter of 20 mm.

Several RANS turbulence models were used which showed good agreement with experimental data. The Reynolds Stress Model was found to perform well under large fluid shear and gave slightly better predictions due to the large shear from the rotating tube. However, in larger annular spaces the standard $k-\omega$ and $k-\omega$ SST model was more accurate. Overall all of the turbulence models tested were relatively close to each other, although the RSM model performed only slightly better.

Bouras (2013) conducted a numerical study on natural convection in an elliptical annulus and studied a range of Rayleigh numbers from 50 to 20 000 as well as changing Prandtl numbers. It was found that for the low Rayleigh numbers, smaller than 100, the Prandtl number has no significant influence on the average Nusselt number. For a Rayleigh number larger than 100, the Nusselt number increases with the Prandtl number.

Gnielinski (2015) created a correlation for turbulent flow which is used to describe the Nusselt number over a certain length of an annulus for Reynold numbers larger than 4 000. The correlation is based on flow through a smooth tube and as a consequence, the same equation can be used for both smooth tubes and annular passage flow, with the only difference between the two is the correlation used to describe the friction factor. The appropriate hydraulic diameter should be employed and depending on the boundary conditions of the annulus, an additional factor is applied. The equation by Gnielinski uses a wide range of properties of fluids and although a specific medium is not specified, the correlation does allow for the use of liquids and gasses.

Van der Westhuizen *et al.* (2015) implemented the use of liquid crystal thermography to determine wall temperatures in tube-in-tube heat exchangers. This process was also used by Kohlmeyer *et al.* (2017), who studied the local heat transfer coefficients at the inlet region of an annular flow passage was investigated. For the studied Reynolds number range of between 2 000 and 7 500, it was found that the inlet diameter size has little influence on the local inlet Nusselt number. The local Nusselt number was found to decrease from its maximum at the inlet to a lower uniform value once the flow became fully developed. In the developing length, a secondary peak in the Nusselt number was observed which could have been due to jet impingement. Such behaviour can be partially described by a ring vortex striking a surface with a low-pressure zone, producing intermittent acceleration and deceleration in the developing boundary layer (Uddin, et al., 2013).

Bashir *et al.* (2019) conducted an experimental investigation of single-phase heat transfer in the transitional flow regime for Reynolds number between 1000 and 6000. Different inlet types were investigated as well as contraction ratios in some of these inlet geometries. It was found that a 90 degree bend inlet produced the earliest transition compared to all the other geometries tested.

### 2.4.3. Some heat transfer correlations

As mentioned previously, the heat transfer coefficient is not a fluid property and is determined experimentally. Previous heat transfer correlations can be used to compare current results for errors and to investigate any anomalies in experiments. When investigating heat transfer within annular passages, previous investigations must be studied to gain insight into what can be expected from the results. The parameters which were found to have a significant impact on the heat transfer will allow

for special attention to be made to ensure consistency and accuracy. These parameters could have an impact on the turbulator design and shape. Some of the recent correlations for smooth annuli are presented in Table 1 in chronological order .Other correlations also exist, but those included in Table 1 give a broad overview of the parameters used.

To produce good heat transfer correlations for annular flow, a large amount of experimental data is needed. Several correlations exist, but due to the wide range of possible parameters in annular flow, many of the correlations are restricted in terms of thermal boundary condition, fluid properties and dimensional and geometric ranges. In recent years newer correlations have been developed in an attempt to span wider ranges of application.

Initial correlations describe the Nusselt number in an annulus by accounting only for the Reynolds number and Prandtl number. This is based on to the general relationships which have been shown to exist in simpler geometries such as circular tubes, square ducts and vertical plates:

$$\mathrm{Nu} = function(\mathrm{Re}, \mathrm{Pr}) \tag{10}$$

Often these relations are represented by a power law relation:

$$\mathrm{Nu} = C\mathrm{Re}^{m}\mathrm{Pr}^{n} \tag{11}$$

Here coefficient $C$ and exponents $n$ and $m$ may be constants based on experimental data regression (Cengel & Ghajar, 2010). Often correlations adopt $n$=1/3 or relationships of similar value. This is true for some of the correlations listed in Table 1, including those by Dirker and Meyer (2005), Lu and Wang (2008), and Swamee (2008) as are described in Equations 12, 13 and 14 respectively. As more research was done, correlations became more complex and it is evident that heat transfer is not only dependent on the simple relationship between the Reynolds and Prandtl number, but also properties such as viscosity, friction factor and annulus geometry that do not change by the same amount as Reynolds and Prandtl numbers. Gnielinski (2015) took a different approach in developing his correlation (shown in Equation 15) where this correlation is based on the same form used in calculating the heat transfer in smooth tubes. The last correlation listed in the table is that of Kohlmeyer *et al.* (2017) who updated the Gnielinski (2015) correlation based on the local heat transfer coefficient data that was gathered from their experimental study.

Table 1: A selection of annuli heat transfer correlations

| Authors | Correlation | Equation | Diameter ratio range | Reynolds number range | Applicable medium |
|---|---|---|---|---|---|
| Dirker and Meyer (2005) | $\mathrm{Nu}_{D_h} = C_o \mathrm{Re}_{D_h}^{P} \mathrm{Pr}^{\frac{1}{3}} \left(\frac{\mu_b}{\mu_w}\right)^{0.14}$<br>$P = 1.013e^{-0.067a}$<br>$C_o = \frac{0.003a^{1.86}}{0.063a^3 - 0.674a^2 + 2.225a^1 - 1.157}$ | (12) | 0.313-0.588 | 4 000-30 000 | Water |
| Lu and Wang (2008) | $Nu = 0.00222Re^{1.09}Pr^{0.4}$ | (13) | 0.794 | Re>3 000 | Single phase water |
| Swamee *et al.* (2008) | $Nu = \frac{0.027}{\left(1+\frac{1}{a}\right)^{0.2}} Re^{0.8} Pr^{1/3} \left(\frac{\mu}{\mu_w}\right)^{0.14}$ | (14) | Not specified | Not specified | Not specified |
| Gnielinski (2015) | $Nu = \frac{\left(\frac{f}{8}\right)(Re-1000)Pr}{1+12.7\sqrt{\frac{f}{8}}\left(Pr^{\frac{2}{3}}-1\right)} \left(1+\left(\frac{d_h}{L}\right)^{\frac{2}{3}}\right) K\,(0.75\,a^{-0.17})$<br>$K = \left(\frac{Pr_b}{Pr_w}\right)^{0.11}$ | (15) | - | Re>4 000 | Not specified |
| Kohlmeyer *et al.* (2017) | $Nu_{D_h} = \frac{\left(\frac{f}{8}\right) Re_{D_h} \mathrm{Pr_a}}{\varphi + 12.7\sqrt{\left(\frac{f}{8}\right)}\left(Pr_a^{\frac{2}{3}}-1\right)} \left(1+\left(\gamma\frac{D_h}{L}\right)^{2/3}\right) F_{ann} K$<br>$\gamma = \frac{34\,500}{Re}$<br>$\varphi = 1.92 + \frac{17\,440}{Re_{D_h}} - \frac{0.63}{1+10Pr_a}$<br>$K = \left(\frac{Pr_a}{P_{riw}}\right)^{0.11}$<br>$F_{ann} = 0.75a^{-0.17}$<br>$f = (1.8\log_{10} Re^* - 1.5)^{-2}$<br>$Re^* = Re_{D_h} \frac{(1+a^2)\ln(a) + (1-a^2)}{(1-a)^2 \ln a}$ | (16) | 0.648 | 2 000-7 500 | Water |

## 2.5. Turbulators

### 2.5.1. Background

Eddy promoters or flow turbulators are simple devices that are usually included in locations where heat transfer or mixing needs to be enhanced. Turbulators are placed within a flow field to disturb the velocity field. This disturbance can increase the rate of heat transfer through several mechanisms such as:

- The viscous sublayer in the developing boundary layer being disturbed.
- The turbulence intensity being increased which also improves mixing.
- Heat transfer area being increased.
- Inducing secondary flow.

The use of turbulators has the advantage of increasing local convective heat transfer rates with minimal change in heat exchanger size and shape. A possible disadvantage of employing turbulators is that the increase in the flow pressure drop could outweigh the improvement of the heat transfer. For that reason, some effort is required to optimise and to evaluate the influence of the turbulators on the overall objective of the heat exchanger. It has been found that there is a significant increase in the heat transfer coefficient at higher Reynolds numbers when using turbulators, but this is generally also associated with a significant increase in frictional pressure losses which might make turbulators unattractive. Therefore, research on turbulators is continually being conducted to attempt to maximise the performance of turbulators in a wide Reynolds number range.

Turbulators generally induce a combination of heat transfer mechanisms which are different depending on what type of flow turbulation device is used. The geometry of turbulators have a large impact on the performance of the heat exchanger. Flow turbulators have been developed using a variety of different shapes and sizes which can be applied to nearly all types of heat exchangers. Some examples of turbulators and the main mechanisms that increase heat transfer are:

- Small ribs on a surface will disturb the viscous sublayer.
- Delta wing shaped turbulators increases the turbulence intensity.
- Fins placed on a surface increase the heat transfer area.
- Vortex shedding can cause a sweeping motion as a secondary flow.

Another popular option is the use of a swirl flow device because of its low cost and simplicity. Using helical tapes does not directly disturb the boundary layer, but rather hinders its development.

Flow turbulation does not only require the addition of material in a heat exchanger but can also be achieved by the removal of material. The use of a dimpled surface within a channel also increases the heat transfer due to vortex structure shedding from the dimples and the shear boundary layer that forms across the top of the dimples. The pressure drop and friction factor is usually not increased significantly.

Turbulators that create recirculation can, however, cause regions of low heat transfer and increase pressure drop. This negative impact can be reduced by using perforated turbulators or by having a gap between the heat transfer surface and the turbulator itself.

### 2.5.2. Previous investigations

Heat transfer enhancement using passive methods have received significant attention in the last 20 years. For instance, regularly spaced twisted tapes within circular tubes have been found to experimentally perform better than full length twisted tapes (Saha, et al., 1989) and the use of helical coil wires in condenser tubes increased the heat transfer coefficient by as much as 100% above the plain tube values (Agrawal, et al., 1998). Investigations like these are important in the search for more energy efficient systems. A selection of research efforts that have relevance to the current study are briefly discussed in this section.

A numerical study into turbulent natural convection in the presence of radial fins was done by Rahnama and Farhadi (2004). The turbulence model used was the standard $k-\epsilon$ model using a modified wall function. In this study it was found that fin arrangement in the annulus had no significant effect on the average Nusselt number but increasing the number of fins reduces the heat transfer rate.

In a numerical investigation by Wang and Zhao (2015) on a single turbulator in a rectangular channel using a large eddy simulation, the influence of vortex shedding on surface heat transfer in fully turbulent flow was investigated. The impact of the gap size between a single cylindrical turbulator (located in the fully developed turbulent boundary layer) as well as the cylinder's wake on the boundary layer was probed. Figure 4a shows how the gap height ($G$) and turbulator diameter ($d$) is defined. The wake alters the turbulent boundary layer drastically which in turn changes the Nusselt number behind the cylinder. When there was no gap, the Nusselt number decreased and as the gap increased, there was a peak in heat transfer directly under the cylinder, as well as a rise afterwards. A similar curve for the local Nusselt number (seen in Figure 4b) could be expected for other cylindrical turbulators, where $x$ is the downstream location and $H$ is the channel height. It is important to note the small hot-spot that was formed with a turbulator with a small gap. The gap ratio had a significant influence on the wake shape and on the downstream flow characteristics. A cylinder that was closer to the wall had vortex shedding which was suppressed until the ratio of the gap over cylinder diameter ($G/d$) was larger than 4.5, where the vortices produced were closer to that of a cylinder in an isolated free stream. It was found that when $G/d$ = 2, the wake disturbed the boundary to produce the highest overall averaged Nusselt number increase of 18.76%. With small gap sizes the enhanced heat transfer was due to oscillations in a separation zone caused by the cylinders wake where the larger gaps had an increased heat transfer due to more of a sweeping motion of the vortex shedding. Best performance seems to have been in the buffer region where $G/d$ was between 1 and 3.

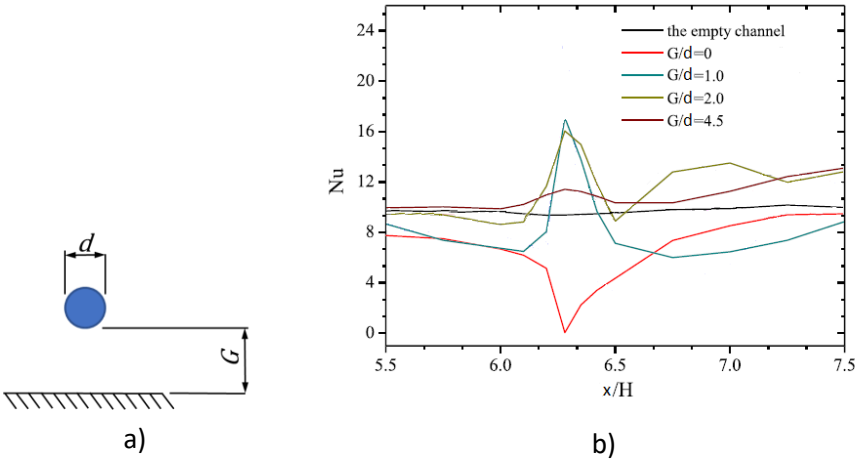


Figure 4: Local Nusselt number on a surface below a cylinder turbulator.

In another numerical investigation, by Ozceyhan *et al.* (2008), the use of circular ring turbulators placed within a smooth tube (see Figure 5) was considered. There was a small gap of 0.3 mm between the rings and the tube wall (constant heat flux boundary). The standard $k$ - $\epsilon$ turbulence model was used and verified by comparing simulation results for a clean tube to conventional tube correlation predictions. As expected, the presence of the rings resulted in an increase in Nusselt number as well as friction factor. The highest Nusselt number was achieved when the pitch between the rings were decreased. When taking friction factor into consideration to calculate an optimum performance between heat transfer and pressure drop, it was found that for pitch-to-tube-diameter ratios less than 2, the overall performance reduced as the pitch was decreased, while it appears to remain constant for pitch-to-tube-diameter ratios greater than 2.

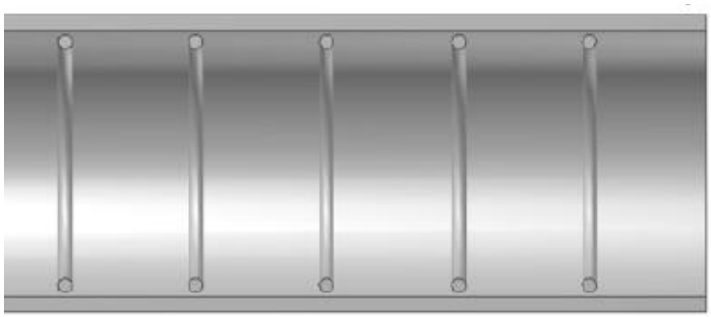

Figure 5: Geometry of circular turbulator rings within a smooth tube (Ozceyhan, et al., 2008).

Zhang (2007) experimentally investigated the heat transfer and pressure drop performance within an annular space of a double pipe heat exchanger with helical flow and petal-shaped fins (see Figure 6) for a Reynolds number between 10 000 and 20 000. It can be seen that the flow was swirled by baffles with petal-shaped fins. The results indicated an improvement of between 235% and 333% in the Nusselt number. The main mechanisms responsible for the increase is the larger surface area provided by the fins and the improved the cross-flow mixing due to the swirling flow patterns. It was, however, not clear which effect is the dominant effect.

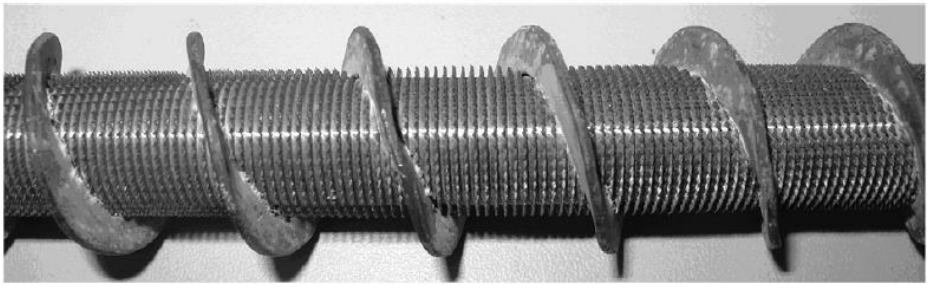

Figure 6: Photograph of the test tube with helical baffles and petal fins (Zhang, et al., 2007).

In a numerical study by Sreenivasulu and Prasad (2009) the use of a helical wire wrapped around the inner cylinder of an annulus (see Figure 7) was investigated for Reynolds numbers between 20 000 and 180 000. Using the $k-\omega\ SST$ turbulence model, it was found that at large Reynolds numbers the heat transfer increases up to 300% for some cases. The two reasons for the increase in heat transfer was the centrifugal force near the inner wall and by turbulent mixing. There was a possibility of hot spots in the cusp region close to the wire wrap. This could be a problem in heat exchanger design and should be kept in consideration when turbulators lie against the heat exchangers surface. In this specific case the insertion of the wire decreased the flow area, thus increasing the flow velocity and Reynolds number. It is not clear whether the Reynolds number reported was this adjusted Reynolds number or the same reference Reynolds number used to compare the results to a clean annulus.

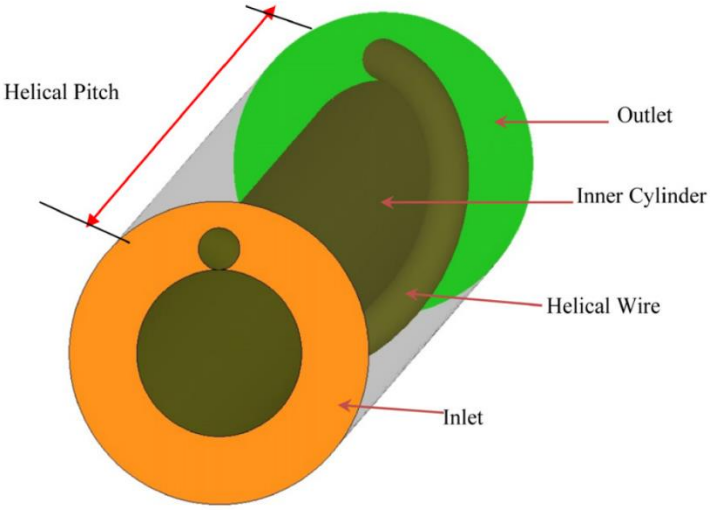


Figure 7: Geometry used in the numerical study (Sreenivasulu & Prasad, 2009).

A number of studies was performed by Sheikholeslami *et al.* (2016) on different turbulator types within annular spaces. In one of these studies, the effect of rectangular cross-sectional ring and perforated ring turbulators were studied experimentally as seen in Figure 8 for a Reynolds number between 6000 and 12 000. The rings without any perforations produced a higher heat transfer than with perforation holes, but the friction factor was higher which leads to a better performing heat exchanger that has the perforations in.

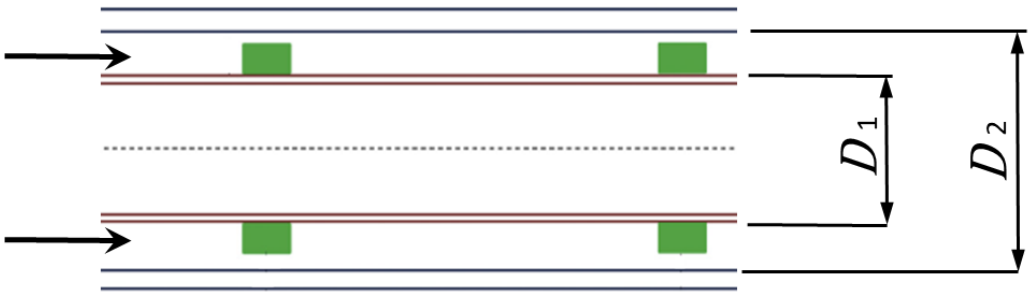


Figure 8: Section of the test section (Sheikholeslami, et al., 2016).

The same was found to be true when using a conical-shaped turbulator, as shown in Figure 9, from another study by Sheikholeslami *et al.* (2016). An experimental investigation and a numerical model was also set up using the RNG $k$ - $\epsilon$ turbulence model with enhanced wall treatment for a Reynolds number between 6 000 and 12 000 where it was found that a larger cone angle produced a smaller pressure drop due to a lower rotating flow intensity.

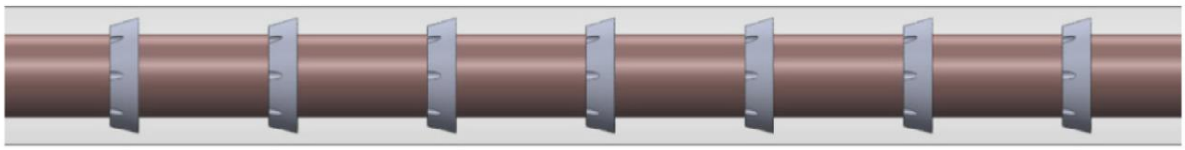

Figure 9: Conical turbulators used in the annular space (Sheikholeslami, et al., 2016).

It was noted that the effect of a turbulator was more pronounced in low Reynolds numbers due to the thicker boundary layer that is disturbed (Sheikholeslami, et al., 2016).

## 2.6. Chapter summary

A background in annular flow has been covered with studies related to the calculation of heat transfer in annuli as well as the basic concepts in numerical heat transfer with boundary layers. Some investigations into mixed convection revealed interesting heat transfer anomalies locally close to the entrance of annular passages. The chapter also gave a brief overview of what turbulators are, where they are employed and the mechanisms behind why they increase the heat transfer. Previous studies on turbulators and turbulators within annular passages was reviewed providing insight on what effects can be expected from this study.

It is clear that there is a lack of investigations into the use of turbulation devices within annuli. There have been some studies but none of these have been done on cylindrical cross-sectional turbulator rings. This study is looking at combining turbulators within annuli and using an accurate method that is not widely used (described in Section 3), which can characterise the local heat transfer coefficient deviations caused by the insertion of turbulation devices. This can assist in the creation of numerical models where an optimisation can take place to characterise the effects of differing turbulator ring geometries.

# 3. Experimental facility and test procedure

## 3.1. Introduction

In this chapter the experimental setup and test method that was used in this investigation is discussed. The relevant information on the design of the experimental test section is presented as well as the test matrix. Information on the method used for acquiring the data is also included.

## 3.2. Experimental facility

An existing experimental facility and setup from a previous study (Kohlmeyer, et al., 2017) was used. In that study local heat transfer coefficients were investigated at the entrance of a smooth horizontal annular test section. In the current investigation, the same flow loop, test section, and test procedure was used, but additional experimental data was produced for conditions with and without ring type flow turbulators. A brief overview of the flow loop is presented first; followed by a detailed description of the test section and of that of the flow turbulators.

### 3.2.1. Flow loop

A schematic representation of the flow loop is given in Figure 10. The test facility was located in the Clean Energy Research Group laboratories of the University of Pretoria and consisted of a closed flow loop in which cold water from a reservoir was circulated through an electrically heated test section. A 1000 litre reservoir tank was maintained at a temperature of between 20°C and 21°C by means of a thermostatic controlled chiller unit. Water was drawn from the reservoir by means of an electrically controlled variable speed SP3 CEMO positive displacement pump with a maximum flow rate of 2000 l/h. Flow fluctuations were dampened by means of a 4-litre blade accumulator before the water passed through a Coriolis mass flow meter with a measuring range of 0.0151 kg/s to 0.606 kg/s and a measurement uncertainty of 0.11%. After the water flowed through the electrically heated test section connected to a power supply, it was returned to the reservoir. Ball valves in the flow loop restricts flow to certain parts of the laboratory (not shown) due to other experimental setups which share the same equipment (such as the pump and reservoir tank). All experiments were performed with exclusive access to the equipment so that there was no external influences present.

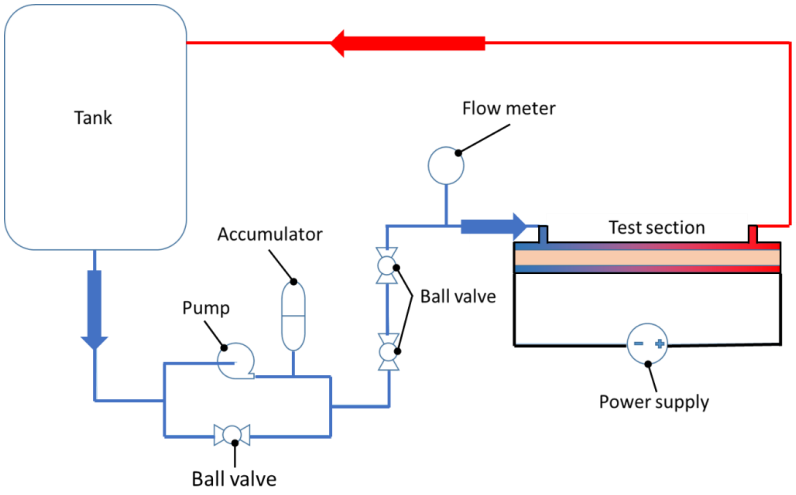


Figure 10: Experimental flow loop.

### 3.2.2. Test section

The test section consisted of a horizontal tube-in-tube annular flow passage as is represented Figure 11. The test section supported the following functions:

- An electrical heater provided a uniform heat flux to the water flowing through the annulus from the inner wall.
- The local wall temperatures on the heated inner wall surface were measured via thermography.
- The inlet and outlet bulk fluid temperatures were measured.
- An approach that allows for the inclusion of internal turbulators to the existing setup was possible.

Due to the test section limitations, there was unfortunately no functionality that allowed the measurement of pressure drop.

The test section was constructed from an inner heating rod and an outer transparent acrylic glass tube which respectively formed the inner and outer walls of the annulus. The heating rod had an outer diameter of $D_1$ = 27.2 mm while the acrylic tube had an inside diameter of $D_2$ = 42 mm a wall thickness of 4 mm. This resulted in an annular diameter ratio ($a = \frac{D_1}{D_2}$) of 0.648 and a hydraulic diameter of $D_h$ = 14.8 mm. The value of the annular diameter ratio is as a result of the standard sizes of the available materials used in construction of the annulus, and not chosen for any specific purpose. The wetted length of the annular passage was $L_{ws} = 1050$ mm, which resulted in length to hydraulic diameter ratio ($\frac{L_{ws}}{D_h}$) of 70.95. The test section had conventional inlet and outlet geometries similar to those found in practice. The inlet and outlet ports were directed radially upward perpendicular to the axial direction of the test section. They had inner diameters of $D_{inlet}$ = 20 mm and were axially separated, centre-to-centre, by a distance of 810 mm.

Although the acrylic glass tube had a low thermal conductivity of 0.19 W/mK, elastomeric thermal insulation with a thermal conductivity of 0.026 W/mK and a thickness of 18 mm was placed over the

external acrylic surface at locations that were not thermally mapped. This minimised the heat loss to the environment, reducing uncertainties in the measurements.

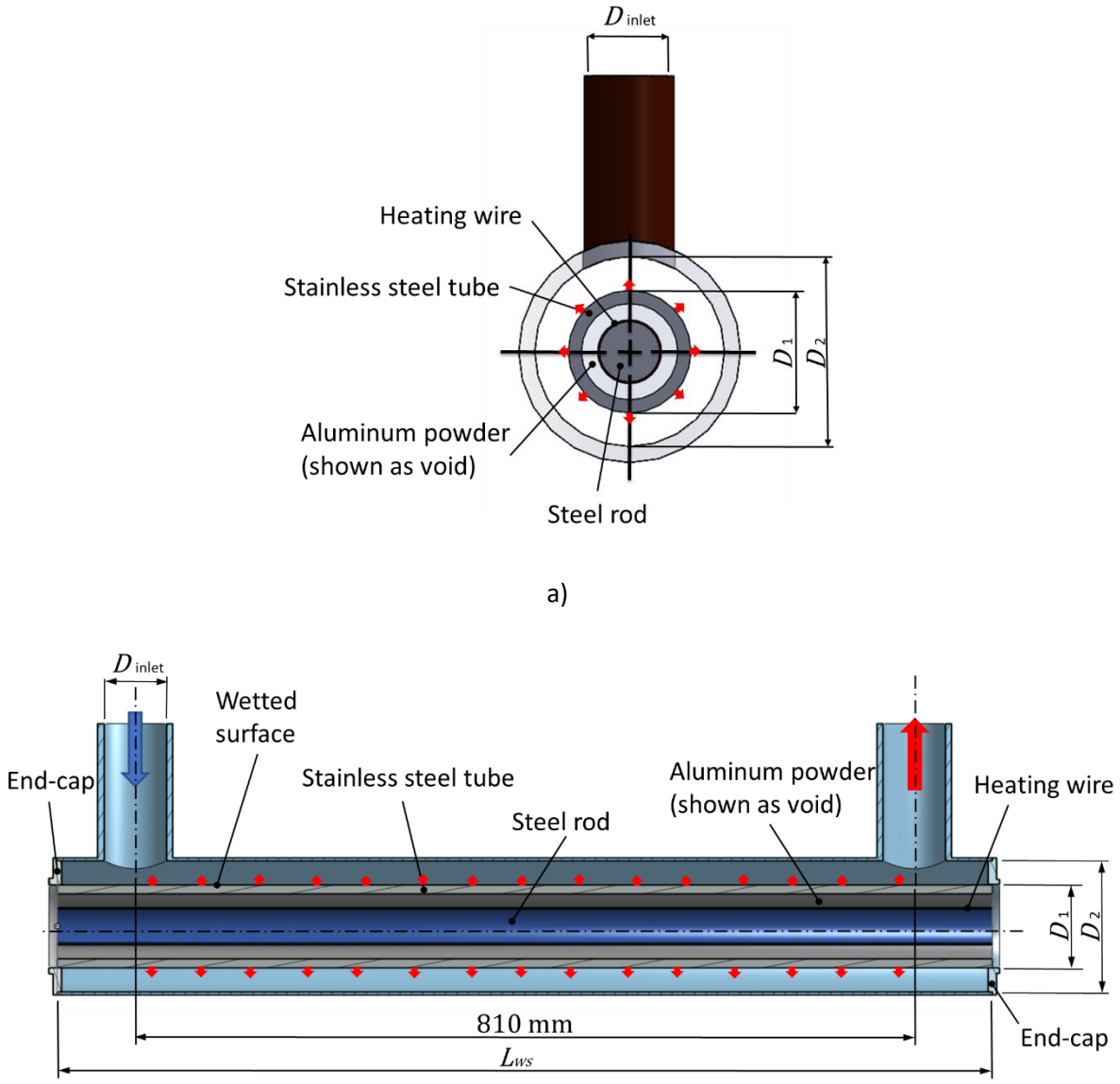


Figure 11: a) Sectioned front view of annular test section and b) sectioned side view of test section.

The heating rod was designed to produce a uniform heat flux and consisted of several internal layers. From the inside outwards these were: a solid bright steel rod with a thermal conductivity of approximately 54 W/mK and an outer diameter of 12 mm, one layer of uniformly wound electrically insulated heating wire, a layer of compacted aluminium powder with a radial thickness of 3.5mm and an effective thermal conductivity of 61.4 W/mK, and an encasing stainless-steel tube with a wall thickness of 2.87 mm and a thermal conductivity of 14.9 W/mK. Due to the small air gap between the wound heating rod and stainless-steel tube, the layer of compacted aluminium powder was used to bridge this gap between the heating wire and the stainless-steel tube. This reduced the thermal

resistance between the heating wire and stainless-steel tube for an even distribution of heat flux on the outer surface of the stainless-steel tube. The internal heating element had an electrical resistance of $R_{elec} = 44.4\,\Omega \pm 0.1\Omega$ and was powered at different heating rates, depending on the test requirements, by means of a direct current Elektro-Automatik (EA 8360-30) power supply unit which had a voltage and current rating of 360 V and 30 A respectively, with an uncertainty of 0.2% of the displayed reading.

The surface of the assembled heating rod was treated with Hallcrest R20C-10-W2 thermal liquid crystal paint which reacted within a temperature band between 20°C and 33°C. This temperature range was specified by the manufacturer and was chosen in this study to operate in the temperature range of interest, although the manufacturer does offer higher and lower temperature paint which could be used in future studies. Due to the paint being soluble in water, a protective layer of self-adhesive PVC film was placed over the painted surface. As will be described in more detail in Section 4.4, the paint colour was used to calculate the local wall temperatures. Only the first half of the heating rod was treated as the fluid is considered fully developed from $x > 10D_h$, so a longer test would be redundant with respect to investigating local heat transfer coefficients.

An automated camera and lighting positioning mechanism controlled by means of an on-board Raspberry-Pi mini-computer was used to rotate and translate a 5-megapixel Raspberry-Pi digital camera around and along the test section to record the colour response of the paint. The camera used was a 5-megapixel Raspberry Pi camera module with a resolution of 2595x1944 pixels. There were three Light Emitting Diodes (LED) placed on each side of the camera module. This provided a constant light source that ensured that there were no shadows in the images as they are taken. The LEDs were LUXEON ES-CW200 that emits light with a colour temperature of 5500 K each at a maximum power of 200 lumen.

Thermocouples were used to measure the bulk fluid temperatures at the inlet and outlet of the test section. The thermocouples used were T-type thermocouples with a bead diameter of 0.8 mm. There were eight thermocouples placed within the annulus inlet, right before the annular passage, and eight at the outlet. The use of eight thermocouples at each location was adopted to reduce the uncertainties in the bulk fluid temperatures measurements. At both the inlet and outlet the thermocouples were soldered to a small length of copper tube at 45° increments to ensure that the average bulk fluid temperature was measured. There was also a rubber insulator placed over the inlet and outlet at the thermocouple's location to minimise any heat conduction to or from the thermocouples. Another thermocouples was placed at the same level as the test section to measure the ambient air temperature used in calculating the heat lost and gained from the environment to the test section.

The test section was designed to be able to be disassembled and reassembled while keeping all components in the test section consistent. The endcaps were machined from nylon and assured that the heated rod was concentric at both ends of the setup. This was important because once base (reference) cases were completed, the setup had to be disassembled and then reassembled with the turbulators in. Thus, the cases with the turbulators were investigated with the confidence that the test section produced results that can be compared consistently.

Looking at a sectioned view of the annulus with turbulators in Figure 12, the dimensions used to describe the annulus containing turbulators are shown. The turbulators were designed to be circular rings with a thickness diameter of $d = 1$ mm with a minimum gap between the wetted surface and turbulator of $G = 1$ mm. These dimensions were chosen because the turbulators would disturb the flow directly in the boundary layer.

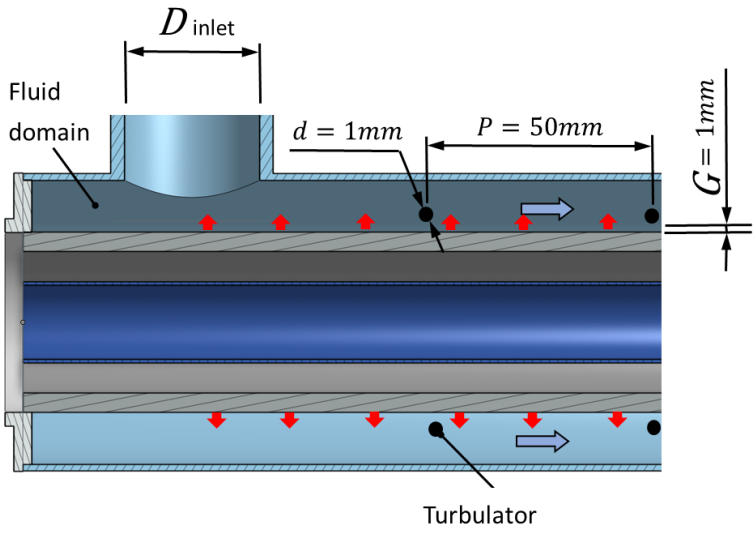


Figure 12: Annuli cross section containing turbulators.

There were 12 turbulator rings manufactured from galvanised wire. The wire was wrapped around a cylinder to get the correct size and circular shape. The rings were cut and soldered into the circular ring. A small jig was built to solder the legs to the rings after which the leg length was measured and clipped in the shape shown in Figure 13. This process was repeated for all the rings.

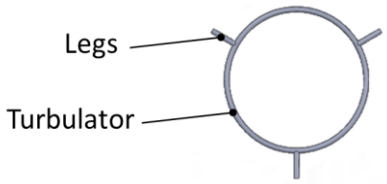


Figure 13: Turbulator with stability legs attached.

The rings had to be connected to a wire which ran axially in the tube. This was done to hold the turbulators at specific axial locations along the annulus. A tempered high-carbon steel (ASTM A228), was chosen for this purpose because it has a higher stiffness than the galvanised wire used for the rings of the turbulators. To achieve the correct geometry between the axial wire and rings, three axial wires were used, as seen in Figure 14a. At each location where a turbulator was, paraffin paper was used to constrain the axial wires at the diameter required to fit into the acrylic tube. The rings were then held down on the paraffin paper and an adhesive was used to connect the axial wires to the turbulators. For this study, the adhesive of choice was cyanoacrylate as it does not bond strongly to the paraffin paper, and a fine sandpaper can remove excess glue with ease. This was left at least 24 hours to ensure complete adhesion.

a) b)

Figure 14: a) Turbulators being built on hung up stand. b) Turbulators fit into outer tube with no movement.

Once the adhesive had bonded the parts together, the structure was strong enough to be handled and was cleaned of any excess glue and solder. Figure 14b shows a portion of the outer tube where the turbulators fit tightly within the tube with no gaps between the axial support wires holding the turbulators and the tube.

The final product is shown in Figure 15 which was strong, light and built to the dimensions required. The first ring was designed to be 35 mm from the inlet and there was a pitch ($P$) of 50 mm between the rings all the way to the end of the test section. The first ring location was chosen as such to attempt to maximise the heat transfer in the annulus and not hinder the high heat transfer at the inlet.

Figure 15: Final turbulators manufactured.

The test section was dismantled and the turbulators were installed as seen in Figure 16. Due to the method of construction used, the turbulators slid into the acrylic tube with ease. The heated rod was also placed back into the test section, with the end-caps installed, the acrylic tube was once again

concentric. Upon inspection of the turbulators it was seen that the rod, turbulators and tube was concentric with each other. To limit the variation of diffraction that could occur from variations in concentricity, multiple calibration curves were created and is covered in detail in Section 3.3.

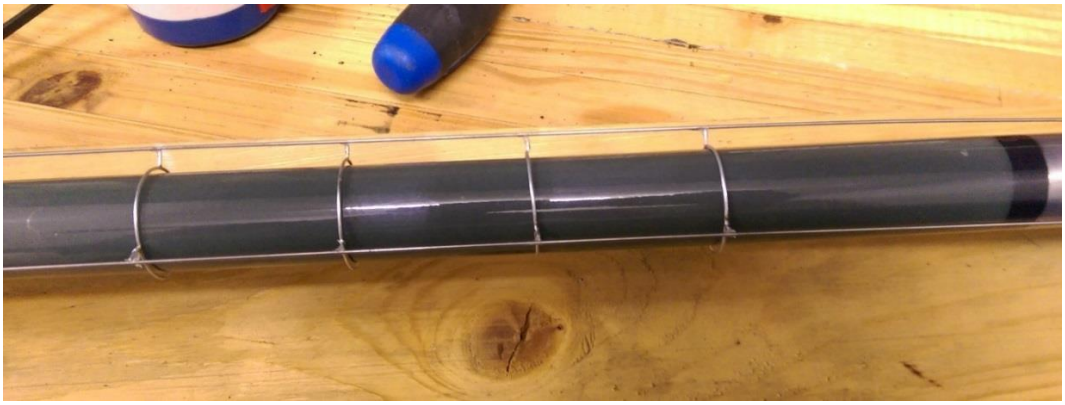

a)

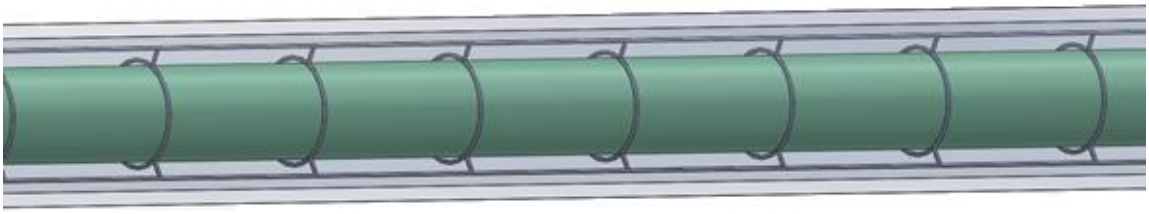

b)

**Figure 16: a) Turbulators fit outside of the heated tube with liquid crystal paint coating and a) drawing of annuli with turbulators installed.**

## 3.3. Calibration

The method used by Kohlmeyer *et al.* (2017) to calibrate the thermocouples as well as creating the liquid crystal paint layer calibration curves is discussed in this section.

### 3.3.1. Thermocouple calibration

As mentioned, in total 17 thermocouples were used to determine the fluid inlet, fluid outlet and ambient temperatures.

Calibration was performed using a Lauda Proline thermal bath containing a PT100 thermocouple calibrated to 0.1°C. Although the thermal bath was calibrated to 0.1°C, the display indicating temperature went to two decimal places which was used to ensure that an isothermal temperature reading was taken up to an accuracy of 0.1°C.

The thermocouples were calibrated for temperatures between 16°C and 26°C at increments of 2°C. At each increment, 600 thermocouple readings were taken over a one-minute period. This was done twice to give a calibration of a heating as well as a cooling cycle. The temperature readings were not logged until the PT100 temperature did not vary by more than 0.1°C and the temperature of the thermal bath did not vary by more than 0.01°C for two minutes.

Using the averaged thermocouple temperatures and the calibrated PT100, a linear line of best fit was created for each thermocouple calibrated against the PT100. This produced an error difference between the thermocouples and PT100 of $\pm 0.01$°C.

### 3.3.2. Liquid crystal surface calibration

Thermochromic liquid crystals are used in a variety of heat transfer problems to measure the surface temperature on an area with little to no intrusion. These crystals can have a narrow-band colour range where the crystals are specially created to operate around a specific temperature with a range of 1°C and wide-band crystals have a range of 5-20°C which allows the surface temperature to be plotted (Kakade & Lock, 2009). Liquid crystals have a specific hue profile which corresponds to a temperature profile response. These profiles are not linear and have to be calibrated.

As mentioned, the liquid crystal paint layer changed colour with temperature, but instead of using the popular red, green, blue (RGB) colour model, Liquid Crystal Thermography studies favour the hue, saturation, intensity (HSI) colour representation due to a monotonic relationship between the hue value and temperature producing high accuracy flow-field temperature distributions (Smith, et al., 2001). This colour representation uses cylindrical co-ordinates to describe the shade and intensity of colour. In these cylindrical co-ordinates the hue value specifies the colour type (such as red, green, blue, etc.) which ranges from 0° to 360°. The saturation varies from 0 to 1 and represents the variation of the colours "lightness". The intensity also varies from 0 to 1 and represents the brightness of the colour.

To get the temperature of the liquid crystal paint, the images taken are converted to the HSI model and the hue values are averaged by taking the mean hue of the image. The hue values are usually measured between 0° to 360° but these values can also be normalised to between 0 and 1. Computer programming platforms with built-in functions can be used to convert RGB colour to the normalised hue values using a conditional algorithm shown in Equation 17. The program used to do the conversion in this study was MATLAB.

$$hue = \begin{cases} \dfrac{G-B}{6(R-\min(R,G,B))} & if\ R = Max \\ \dfrac{2+B-R}{6(G-\min(R,G,B))} & if\ G = Max \\ \dfrac{4+R-G}{6(B-\min(R,G,B))} & if\ B = Max \end{cases} \tag{17}$$

The calibration data to get a temperature-hue curve was created by circulating water, from the same Lauda Proline thermal bath used to calibrate the thermocouples, at a known temperature through the test section. Once the system had reached a steady state (considered when the inlet temperature and outlet temperature did not vary by more than 0.1°C for five minutes) photos of the liquid crystal treated surface (inner wall of the annulus) were taken. The photos were processed, and the normalised hue values were calculated. A calibration curve for the liquid crystal paint layer on the inner wall of the annulus was created using 52 independent temperature readings to give a good

calibration resolution. An example of a calibration curve is shown in Figure 17. The curve has a sharp increase in temperature from a hue of approximately 0.42. To produce polynomials that fit the data well, the curve has two polynomials sections to describe the data, one for hue values up to 0.42 and another for hue values above 0.42. The polynomials were of the sixth and fifth orders respectively. The upper curve contained the larges absolute error of 0.236°C and the average error over both curves was 0.036°C. Also indicated in Figure 17 is the temperature uncertainty of the thermal bath.

There were some localised variations in hue values around the circumference which could be attributed by diffraction through the Perspex tube and a variation of distance between the surface and camera from a slight sag in the heated rod. To mitigate this and to improve the accuracy, each radial position (circumferential position around the inner surface of the annulus), which were relevant to this study, had its own calibration curve. The area region close to the inlet was calibrated at a higher axial resolution and were represented by a separate set of calibration curves, while for regions further downstream a lower axial location resolution was used. This resulted in 16 calibration curves for the test setup (8 radial positions each at in the region close to the inlet, and further downstream).

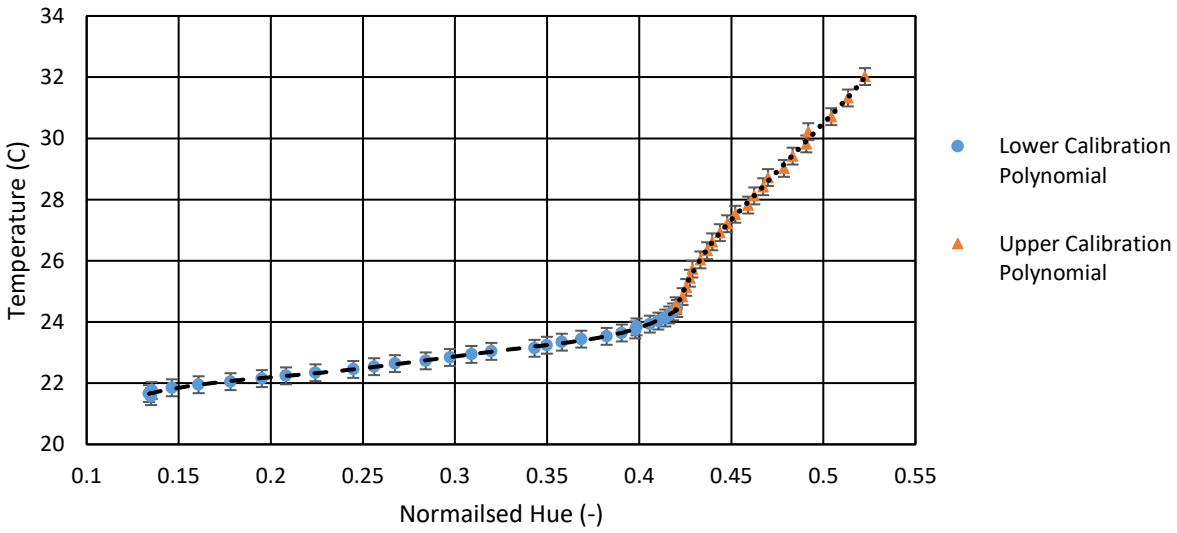


**Figure 17: Temperature-Hue calibration curve for the liquid crystal paint layer.**

## 3.4. Data acquisition and test procedure

A data acquisition system was used to monitor and capture the temperatures from the thermocouples, the flow rate from the Coriolis flow meter, and the power dissipation in the heating rod. The hardware used to record this data consisted of a National Instruments SCXI-1303 data card, SCXI-1102 Thermocouple Input Module (accuracy of maximum 0.02% of reading) and SCXI-1001 Chassis. The data was recorded from the hardware using LabVIEW software on a personal computer in the laboratory.

Images were taken of the liquid crystal paint layer in the test section to be able to calculate the surface temperature. To keep consistency in the location, size and lighting of the images taken, an automated system was used which consisted of a rotating mechanism that rotated around the test section. On

this section was a Raspberry-Pi B model 2 which controlled stepper motors for positioning and had the 5-megapixel camera attached to it. Stepper motors ensured that the images were consistently taken at the same positions in all of the tests. Due to the Raspberry-Pi camera being a separate module that connects to the Raspberry-Pi, all the automatic features of the camera were fixed to ensure consistency in the imaging.

The tests were done at night for two reasons: this was to ensure the UV light from the sun did not degrade the liquid crystal pain layer and changing light conditions would also have had an influence on the colour of the images recorded by the camera. Due to the sensitivity of changing the lighting angles and lighting used on the crystals, the lights in the laboratory were also switched off during experimental runs and only the LED lights on the setup were used.

For any given test case, the water that was circulated through the test section had a starting temperature of approximately 20.5°C. This was reached by circulating the water through the chiller and the 1000 litre water tank to ensure the flow loop has the same water temperature. While the water was pumped through the test setup, the temperature was constantly measured at the inlet and outlet.

To perform the tests, the flow rate was adjusted to the Reynolds number required and the power supply was set to deliver 312 W for all the tests performed. This power was chosen such that the surface temperature was within the liquid crystal's calibrated temperature range (this is covered in more detail in Section 3.3) and produced a heat flux on the wetted surface of 3942 W/m$^2$. The setup was monitored until a steady state was reached. The criteria used for a steady state was when the temperature variations at the inlet and outlet did not fluctuate by more than 0.1°C over a period of 5 minutes.

With steady state conditions achieved, the process for capturing the images were commenced. The LED's were switched on and the data logger and Raspberry-Pi was synchronised. Once ready, the Raspberry Pi controlled the stepper motors and started imaging the inner annular surface. Eight images were taken around the circumference at 45$^o$ increments, after which the Raspberry-Pi moved along the axis. The number of circumferential images was based on the findings of Kohlmeyer *el al.* (2017), who found that there was no noticeable impact on the average local heat transfer coefficient compared to when more circumferential images were used. The procedure was done at 33 axial positions along the flow direction of the test to produce a total of 264 images. On average, each image location took 4.5 seconds to complete. This was done to ensure the camera system has stabilised and came to a complete stop before the image was taken.

Higher axial densities of images were adopted at the entrance region of the annulus to capture a higher resolution temperature field in the area where the boundary layer was developing. The images taken on the surface of the annulus had a size of 10.6 mm x 10 mm, which were taken in the first 110 mm of the annulus, after which the size increased to 10.6 mm x 20 mm. Figure 18 describes where the images were taken on the annulus. The colour represents what would actually be seen in the setup, with the paint being a green colour at lower temperatures and changes to a blue colour with higher temperatures. These sizes represent the actual imaged area on the heated inner tube. Due to

a step size error during the transition between high and low resolution images, there was a 2.5 mm gap between the images, this had no noticeable influence on the results and only shifts the temperature field by 2.5 mm. The number of digital pixels used in the cropped images were approximately 113 400 pixels. Cropping was necessary to analyse only specific sized sections on the tube to produce the local temperatures.

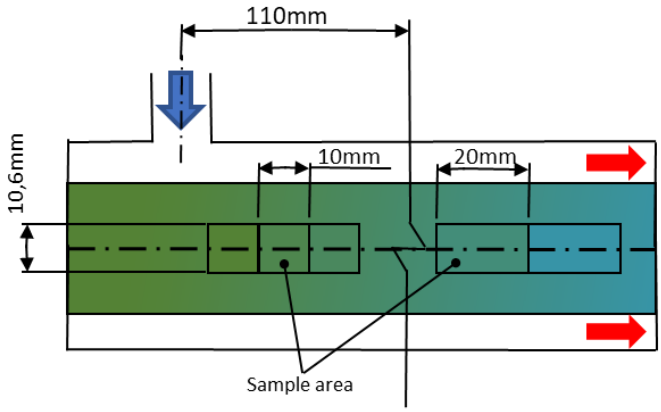


Figure 18: Sample pictures that are taken of the heated pipe.

As mentioned, to limit heat loss to the ambient air, insulation was placed over the outer tube of the test setup. This insulation was divided into sections such that there was an open area at the location that the camera has stopped at to be able to view the internal tube. When the camera moved to the new axial position, the insulation was also moved to allow for viewing at the new position.

Figure 19a gives an example of an image taken of the inner wall treated with thermochromic liquid crystals during a test run in the annulus without turbulators and Figure 19b shows the image taken with the turbulator insert visible. It can be seen that in this instance, the surface had a greenish colour which indicates that the thermochromic crystals was within the temperature sensitive bandwidth. Because the view angle of the surface has an impact on the observed colour, only a small region of each image was used. For this reason, each image was cropped and only the rectangular block as shown was used during the data analysis. It is also noted that the insulation is not visible in these images because the insulation was moved as the camera moves, mentioned previously.

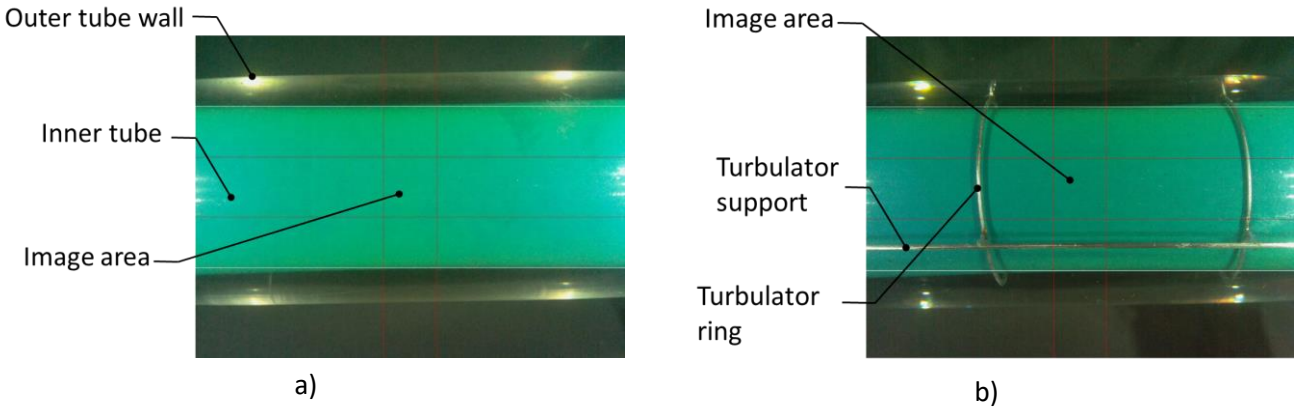


Figure 19: Image taken of the test section that was used to determine the surface temperature for a) the reference annulus and b) turbulator inserts.

This process was repeated for a range of Reynolds numbers at the same heat flux. With all the images available, the data could be processed into a surface temperature profile. This process of transforming the images into a temperature profile is covered in Section 4.4.

## 3.5. Experimental test matrix

To do a comparison between the reference annulus (without turbulator rings) and an annulus with turbulator rings, the same Reynolds number set was used. The target Reynolds numbers were approximately 2000, 4000, 6000 and 7500. This corresponded to mass flow rates of approximately 0.109 kg/s, 0.217 kg/s, 0.325 kg/s and 0.405 kg/s respectively. These numbers were chosen because they are in the turbulent flow regime which was able to give a good overall trend of the heat transfer coefficient with Reynolds number and another motivation is that the results can be compared to previous studies done on this test setup.

The exact Reynolds numbers achieved where calculated with the previous Equation 3, but the hydraulic diameter was adjusted for the turbulator case. As discussed, the hydraulic diameter is dependent on the surface area and wetted perimeter. This is a trivial calculation for the reference annulus but not for the turbulator case. Reynolds number for the turbulator case was calculated by taking into account the longitudinal support wires only and not the actual turbulators. This is because the turbulators only form a small part of the flow section while the majority of the flow is only subjected to the support wires.

With the average velocity calculated from the measured mass flow rate and calculated hydraulic diameter the Reynolds numbers were calculated. The target and actual Reynolds numbers are shown in Table 2, for the reference annulus the difference in target and actual Reynolds numbers have a range between 1.93% and 2.33%, the turbulator case has a range between 2.44% and 2.69%. The maximum difference in Reynolds numbers between the reference cases and turbulator cases was considered to be close enough to make a comparison between the cases.

**Table 2: Target vs. actual Reynolds number achieved in experiments.**

| | **Reynolds number achieved** | | | |
|---|---|---|---|---|
| **Target Reynolds number** | **Reference annulus** | **Difference from target** | **Turbulators** | **Difference from target** |
| 2000 | 2043 | 2.15% | 1946 | 2.69% |
| 4000 | 4077 | 1.93% | 3902 | 2.44% |
| 6000 | 6135 | 2.25% | 5848 | 2.53% |
| 7500 | 7675 | 2.33% | 7310 | 2.53% |

## 3.6. Chapter summary

This chapter presented the experimental facility and test section setup which will be used in the calculation of the local heat transfer coefficients. The methods and hardware used in the data acquisition system was setup to record the flow rate, inlet and outlet temperatures of the test section. The inner tube was built to produce a uniform heat flow and a coat of temperature sensitive liquid

crystals was painted on the smooth surface. A set of turbulator rings were constructed to be fitted to the test section. The surface was automatically imaged using stepper motors and a control system. Calibration curves were obtained for the liquid crystal paint and the thermocouples were also calibrated. A test matrix was setup for four different Reynolds numbers tested for a reference annulus and an annulus with ring turbulators.

# 4. Experimental data analysis and results

## 4.1. Introduction

This chapter contains the data reduction methods used to calculate the local and average experimental heat transfer coefficients in the annulus as well as the associated uncertainty values. The chapter also presents the data validation and the processed results.

## 4.2. Energy balance

As with any investigation into heat transfer, aspects such as energy loss, equipment uncertainty, and environmental effects must be minimised, or accounted for accurately. The steady state energy balance error ($EB$) was calculated by comparing the measured and estimated total inputs to the total energy output rates, and the difference was represented as a percentage as described in Equation 18. This equation calculates the percentage of energy that has not been accounted for, with the electric heater supplying energy ($\dot{Q}_{elec}$) and the water gaining the energy ($\dot{Q}_a$).

$$EB = \frac{\dot{Q}_{elec} - \dot{Q}_a}{(\dot{Q}_{elec} + \dot{Q}_a)/2} \times 100 \tag{18}$$

A refined energy balance error is shown in Equation 19, this energy balance error takes the estimated energy loss to the environment ($\dot{Q}_{loss}$) into account.

$$EB_{ref} = \frac{\dot{Q}_{elec} - (\dot{Q}_a + \dot{Q}_{loss})}{(\dot{Q}_{elec} + \dot{Q}_a)/2} \times 100 \tag{19}$$

$\dot{Q}_{loss}$ is assumed to be constant along the annulus because there was negligible change of $\dot{Q}_{loss}$ due to the following reasons:

- There is a small temperature difference of bulk fluid temperature along the length of the annulus.
- The thermal resistance of the annulus to the ambient environment Is high.
- As mentioned previously, the insulation is moved to provide space for images to be taken, creating a dynamic problem.

The heat gained by the water ($\dot{Q}_a$) was first calculated using Equation 20. The mass flow rate ($\dot{m}$) through the annulus was obtained from the Coriolis flow rate meter. The bulk fluid inlet temperature ($T_{b,in}$) and outlet temperature ($T_{b,out}$) were obtained by taking the arithmetic average of the eight inlet and eight outlet thermocouples respectively. The specific heat capacity ($c_p$) of water was calculated by the equations Popiel & Wojtkowiak (1998) at the average bulk fluid temperature, taken as the arithmetic average of the inlet and outlet bulk fluid temperature before and directly after the test section.

$$\dot{Q}_a = \dot{m} C_p (T_{b,out} - T_{b,in}) \tag{20}$$

The electric power supply supplied direct current to the heating wire in the heated rod. The rate of energy transfer $(\dot{Q}_{elec})$ to the heated rod, which was fully converted to heat, was calculated using Equation 21, where $V$ and $I$ represent the voltage and current respectively that was displayed on the power supply connected to the heating wire. To ensure the reliability of the power input to the heating rod, the voltage and current input to the setup was manually set on the power supply display to an accuracy of two decimal places. The power supply produces an output uncertainty of 0.2% which is taken into account in the uncertainty analysis in a later section. An active power correction circuit is built in internally to the power supply which also increases confidence in the power output.

$$\dot{Q}_{elec} = VI \tag{21}$$

Although steps were taken during the experimental procedure to minimise heat loss to the environment, it cannot altogether be eliminated. To take this into consideration, energy balance checks were performed to quantify the relative energy loss rate to the environment. The relative degree of energy loss can significantly influence the local bulk fluid temperature, which could have a significant impact on the calculated heat transfer coefficients.

Energy loss from the test section could have occurred in multiple ways, such as:

- Heat loss through the plexiglass tube and the insulation around it in portions where liquid crystal thermography was temporarily not performed.
- Local heat loss through the plexiglass tube without external insulation in portions where liquid crystal thermography was temporarily performed.
- Heat loss through the endcap supports.

These losses were driven by the temperature differences between the inner bulk fluid temperature and the ambient air in the laboratory. These temperature differences were generally small due to the water reservoir being at the same temperature as the laboratory. This was true during the experimental runs and could be checked by comparing the measured water and laboratory air temperatures. The temperature difference between the water inlet temperature and air temperature was approximately 0.3°C, whereas the temperature difference between the outlet temperature and the ambient air temperature was approximately 1°C, depending on the applied heat flux rate and the relevant mass flow rate. Nonetheless, a first-order approximation of a thermal resistance network was developed to account for heat loss rate ($\dot{Q}_{loss}$) from the test section.

The total energy loss was calculated using Equation 22 where $\dot{Q}_{w/insu}$ represents the heat loss at the area with insulation, $\dot{Q}_{wo/insu}$ represents the heat lost at the area without insulation and $\dot{Q}_{caps}$ represents the heat loss at the end caps.

$$\dot{Q}_{loss} = \dot{Q}_{w/insu} + \dot{Q}_{wo/insu} + \dot{Q}_{caps} \tag{22}$$

The heat loss through the area without insulation was calculated with Equation 23.

$$\dot{Q}_{wo/insu} = \frac{T_b - T_{amb}}{R_{wo/insu}} \tag{23}$$

With

$$R_{wo/insu} = \frac{\ln\left(\frac{r_2}{r_1}\right)}{2\pi Lk} \quad (24)$$

In this case $r_1$ and $r_2$ refer to the inner and outer radii of the outer tube, $L$ is the tube length and $k$ the thermal conductivity of the plexiglass. The same method was employed to calculate the heat loss through the areas with insulation ($\dot{Q}_{w/insu}$) with the added thermal resistance of the insulation.

The thermal resistance of the end caps support was calculated using Equation 25 with $L$ being the cap thickness and $A_c$ the cross-sectional area.

$$R_{caps} = \frac{L}{kA_c} \quad (25)$$

For the base case results of the reference annulus, the maximum and minimum heat loss rates were 1.024 W (0.33%) and 0.5029 W (0.16%) respectively. For the cases with turbulator rings, higher maximum and minimum loss rate of 1.673 W (0.52%) and 1.1515 W (0.36%) respectively were applicable.

Table 3 summarises the energy balance errors of all the experiments performed. There are two important observation that must be clarified from the energy balance results. The first is that the reference annulus lost heat to the ambient and the turbulator annulus gained heat from the ambient. This was the cause of the negative energy balance error seen in Table 3 for the turbulator case. Figure 20 shows the inlet, outlet and ambient temperature for reference annulus and the turbulator annulus. The cause of the negative energy balance error was due to the ambient temperature being higher than the annulus for the turbulator case, while the reference annulus had an ambient temperature lower than the annulus. This was due to the turbulator experiments being done closer to summer which created a higher temperature in the laboratory. The second observation is that the energy balance error for the turbulator annulus had a higher overall energy balance error. Again, the reason is seen in Figure 20, the difference in temperature between annulus and ambient was larger for the annulus containing the turbulator than that of the reference annulus.

**Table 3: Summary of the energy balance errors for all experiments run.**

| Reference annulus<br>Reynolds number | Basic energy balance (Eq 18) (%) | Refined energy balance (Eq 19) (%) | Difference from basic energy balance (%) |
|---|---|---|---|
| 2043 | 3,16 | 3,00 | 0,17 |
| 4077 | 3,69 | 3,47 | 0,22 |
| 6135 | 3,41 | 3,14 | 0,28 |
| 7675 | 1,40 | 1,06 | 0,33 |

| Turbulator annulus<br>Reynolds number | Basic energy balance (Eq 18) (%) | Refined energy balance (Eq 19) (%) | Difference from basic energy balance (%) |
|---|---|---|---|
| 1946 | -1,18 | -0,67 | -0,52 |
| 3902 | -3,97 | -3,51 | -0,46 |
| 5848 | -7,48 | -7,09 | -0,39 |
| 7310 | -8,95 | -8,62 | -0,33 |

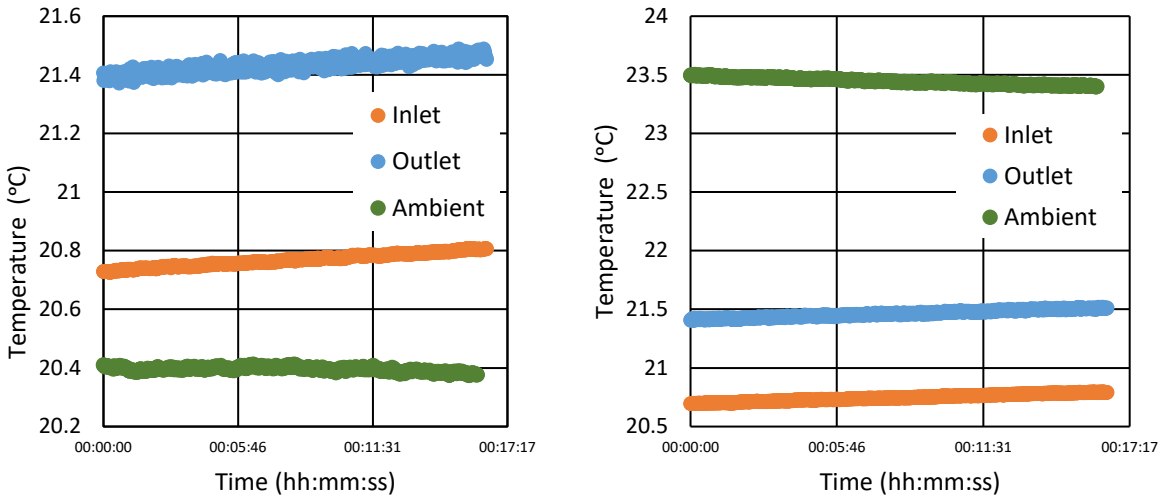


a) b)

**Figure 20: The temperature measured during an experiment showing the difference in temperature from of the ambient compared to the annulus for a) reference annulus and b) turbulator annulus.**

## 4.3. Water inlet temperature drift

Even with the use of a water reservoir, a small temperature drift was present in the bulk fluid measurements. This temperature drift effect can be seen in Figure 21a, where the temperature change with time is shown during a typical experiment. The temperature difference between the inlet and outlet in the graph at a specific time is proportional to the energy gained by the water. The temperature rise from the inlet and outlet, shown in Figure 21b, remained however constant, indicating that the net heat rate into the test section was constant. This was true for all cases for which data was collected.

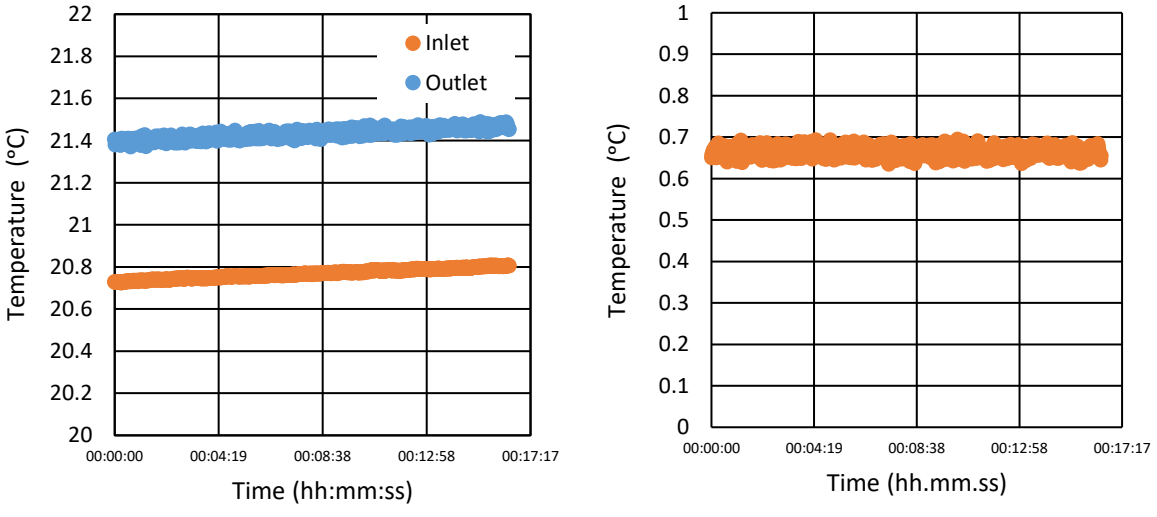


a) b)

**Figure 21: a) Bulk fluid temperature change at the inlet and outlet of the test section and b) difference in temperature at a specific time.**

The temperature drift was taken into account when calculating the heat transfer coefficient as the bulk fluid temperature along the annulus slowly changed over time.

To overcome the temperature drift, the bulk fluid temperature was updated to the relevant temporal temperature during the experiment. This was possible because before the experiment started the imaging controller and data capture system was synchronised. This synchronisation allows the instantaneous bulk fluid temperature to be captured at the same time that any given images was recorded. The bulk fluid temperature was adjusted for that specific image and used during the heat transfer coefficient calculations.

## 4.4. Local heat transfer coefficient data reduction

When calculating the local heat transfer coefficients, the bulk fluid temperature which is dependent on the time of the measurement ($t$) and the axial location ($x(i)$), ($T_b(x(i),t)$) is required and was calculated using Equation 26. Figure 22 shows how the annulus was modelled to give the local surface and bulk fluid temperature where $i$ is the local position in the annulus. The bulk fluid temperature increased linearly along the tube length because the test section was modelled as a constant volume system with a constant heat flux and is also a function of time due to the temperature drift discussed previously.

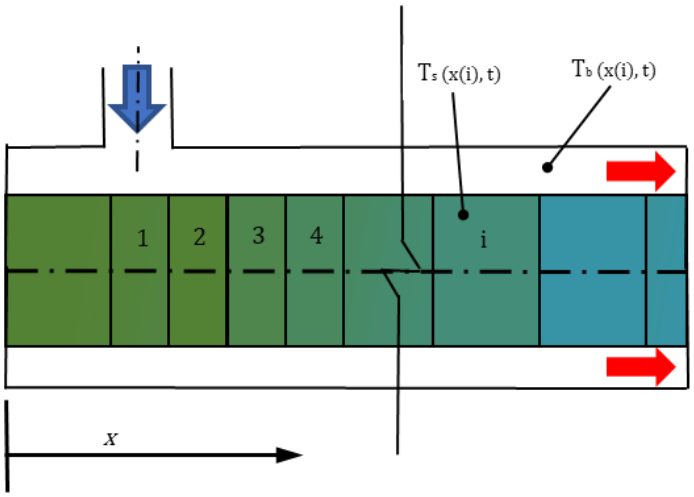


Figure 22: Local heat transfer coefficient and bulk fluid temperature location definition.

The energy loss terms are taken into account when calculating the bulk fluid temperature also seen in Equation 26.

$$T_b(x(i),t) = T_{bin}(t) + \frac{x(i)}{L_{ws}} \frac{(\dot{Q}_{elec} - \dot{Q}_{loss})}{\dot{m}\, Cp} \qquad (26)$$

The sum of the convection heat transfer rates ($\Sigma\dot{Q}_{conv}$) was calculated with Equation 27. In this equation the unknown local heat transfer coefficient ($h(x(i),t)$) is of interest. The surface area also used in these calculations ($A_s(x(i))$) was the local surface area on the tube. As mentioned previously, the images taken on the surface of the annulus had a size of 10.6 mm x 10 mm, which were taken in the first 110 mm from the inlet, after which the size increases to 10.6 mm x 20 mm.

$$\Sigma \dot{Q}_{conv} = h(x(i),t)\, A_s(T_{ws}(x(i),t) - T_b(x(i),t)) = \dot{Q}_{elec}(x(i)) \quad (27)$$

As mentioned previously, there was a transparent layer of self-adhesive PVC film protecting the paint from the water. The temperature of the liquid crystal paint layer is not the surface temperature that was in contact with the fluid. The actual surface temperature was calculated using the resistance of the PVC film which was calculated to be 0.004996 ˚C/W for a single layer. This resistance was previously determined experimentally and compared to the manufacturer's specification sheet, producing a difference between the two of 1.051% (Kohlmeyer, et al., 2017). To calculate this value experimentally, temperature readings were taken with two layers of PVC and then again with three layers, all readings were done at five different Reynolds numbers at the same heat flux. Using the temperature differences and heat flux, it was possible to calculate the resistance of the PVC film used.

There were a number of terms that had to be determined to be able to calculate the wetted surface temperature ($T_{ws}$). Using a thermal resistance network of the PVC film resistance ($R_{PVC}$), the local liquid crystal paint layer temperature ($T_{TLC}$), and the local electric heat flux ($\dot{Q}_{elec}(x(i))$), the wetted surface temperature ($T_{ws}(x(i),t)$) was calculated using Equation 28. This study used 3 layers of PVC film creating a relatively high thermal resistance of the PVC film which gives a temperature difference between the wetted surface and liquid crystal paint of 4.69°C.

$$T_{ws}(x(i),t) = T_{TLC}(x(i),t) - (\dot{Q}_{elec}(x(i))R_{PVC}) \quad (28)$$

With the calibration data of the liquid crystal paint and images available, the temperature of the liquid crystal paint layer ($T_{TLC}$) was calculated. For each image taken in the test section images were cropped to size and the colour for each pixel was converted to hue values as was described in Section 3.3. The number of digital pixels used in the cropped images are approximately 113 400 pixels. The arithmetic mean of the hue value was calculated from all the pixels in the images. The hue values were processed into temperature values using the calibration curves and the temperature map was plotted, with the locations to scale, as is shown in Figure 23. The angular position of the temperature is indicated by the values in the first column, where 0° represent the upper surface of the inner cylinder and -180° and +180° represent the lower surface. At the location of the annulus inlet, interference with the water supply line prevented the recording of the surface colour, and is thus indicated by black in the figure.

Figures like these represent the temperature field of the liquid crystal temperature on the surface of the inner tube. As seen, there is a higher resolution at entrance region of the tube and the temperature field was available around the whole tube.

Temperature field - TLC

| x(mm) | 5 | 15 | 25 | 35 | 45 | 55 | 65 | 75 | 85 | 95 | 105 | 115 | 132,5 | 152,5 | 172,5 | 192,5 | 212,5 | 232,5 | 252,5 | 272,5 | 292,5 | 312,5 | 332,5 | 352,5 | 372,5 | 392,5 | 412,5 | 432,5 | 452,5 | 472,5 | 492,5 | 512,5 | 532,5 |
|---|---|---|---|---|---|---|---|---|---|---|---|---|---|---|---|---|---|---|---|---|---|---|---|---|---|---|---|---|---|---|---|---|---|
| -180 | 26 | 27 | 27 | 27 | 27 | 28 | 28 | 28 | 28 | 28 | 28 | 28 | 28,5 | 28,58 | 28,68 | 28,92 | 29,1 | 29,32 | 29,47 | 29,58 | 29,77 | 29,78 | 30,02 | 30,13 | 30,44 | 30,6 | 30,62 | 30,49 | 30,49 | 30,74 | 30,84 | 30,89 | 30,88 |
| -135 | 27 | 27 | 27 | 27 | 27 | 28 | 28 | 28 | 28 | 28 | 28 | 29 | 28,75 | 28,71 | 28,91 | 29,01 | 29,15 | 29,43 | 29,64 | 29,57 | 29,74 | 29,86 | 29,88 | 30,12 | 30,21 | 30,4 | 30,47 | 30,26 | 30,35 | 30,63 | 30,7 | 30,71 | 30,77 |
| -90 | 26 | 27 | 27 | 27 | 27 | 28 | 28 | 28 | 29 | 29 | 29 | 29 | 28,85 | 28,82 | 29,2 | 29,24 | 29,21 | 29,42 | 29,69 | 29,55 | 29,69 | 29,83 | 29,88 | 30,01 | 30,22 | 30,43 | 30,37 | 30,25 | 30,31 | 30,54 | 30,64 | 30,79 | 30,91 |
| -45 | | 27 | 27 | 28 | 28 | 29 | 29 | 29 | 29 | 29 | 29 | 29 | 29,01 | 29,05 | 29,37 | 29,27 | 29,52 | 29,58 | 29,74 | 29,6 | 29,72 | 29,87 | 29,9 | 29,99 | 30,13 | 30,43 | 30,39 | 30,31 | 30,31 | 30,53 | 30,72 | 30,91 | 30,93 |
| 0 | | | | | | 29 | 29 | 30 | 30 | 29 | 29 | 29,04 | 28,9 | 29,11 | 29,33 | 29,38 | 29,6 | 29,72 | 29,46 | 29,71 | 29,86 | 30,07 | 30,05 | 30,17 | 30,4 | 30,44 | 30,45 | 30,56 | 30,64 | 30,62 | 31 | 31,21 | |
| 45 | | 27 | 28 | 28 | 28 | 28 | 29 | 29 | 29 | 29 | 29 | 28,87 | 28,72 | 29,03 | 29,14 | 29,31 | 29,55 | 29,72 | 29,64 | 29,77 | 29,9 | 29,93 | 29,99 | 30,17 | 30,42 | 30,61 | 30,67 | 30,75 | 30,95 | 31,03 | 31,31 | 31,43 | |
| 90 | 26 | 26 | 27 | 27 | 27 | 27 | 28 | 28 | 28 | 28 | 28 | 28 | 28,5 | 28,32 | 28,55 | 28,7 | 29,03 | 29,29 | 29,54 | 29,52 | 29,8 | 29,87 | 30,16 | 30,17 | 30,19 | 30,5 | 30,7 | 30,74 | 30,94 | 31,14 | 31,14 | 31,35 | 31,38 |
| 135 | 26 | 27 | 27 | 27 | 27 | 27 | 28 | 28 | 28 | 28 | 28 | 28 | 28,41 | 28,39 | 28,41 | 28,62 | 28,93 | 29,26 | 29,51 | 29,63 | 29,88 | 30,01 | 30,18 | 30,34 | 30,45 | 30,72 | 30,83 | 30,69 | 30,7 | 30,85 | 31 | 31,1 | 31,02 |
| 180 | 26 | 27 | 27 | 27 | 27 | 28 | 28 | 28 | 28 | 28 | 28 | 28 | 28,5 | 28,58 | 28,68 | 28,92 | 29,1 | 29,32 | 29,47 | 29,58 | 29,77 | 29,78 | 30,02 | 30,13 | 30,44 | 30,6 | 30,62 | 30,49 | 30,49 | 30,74 | 30,84 | 30,89 | 30,88 |

**Figure 23: Temperature field (°C) of the heated inner cylinder.**

Combining Equation 26 and Equation 28 with some rearrangement, the local heat transfer coefficient was calculated using Equation 29. The surface area ($A$) was calculated from the heating rod's diameter in contact with the fluid and the heated length.

$$h_x(x(i),t) = \frac{\dot{Q}_{elec}}{A(T_{ws}(x(i),t) - \dot{Q}_{elec}\, R_{PVC} - T_b(x(i),t))} \tag{29}$$

With the local heat transfer coefficients available, the local heat transfer coefficient was non-dimensionalised by calculating the local Nusselt number ($Nu_x = \frac{h_x\, D_h}{k}$) along the tube. The average Nusselt number ($Nu_{avg}$) in the tube is the area-weighted average of the local Nusselt numbers.

To investigate the change in Nusselt number due to the addition of turbulators in the annulus, a heat transfer enhancement factor ($\in$) is defined in Equation 30. Where $h_{avg,turb}$ is the average heat transfer coefficient in the developed region of the annulus containing turbulators and $Nu_{avg,ref}$ is the average heat transfer coefficient in the developed region of the reference annulus.

$$\in = Nu_{avg,turb}/Nu_{avg,ref} \tag{30}$$

With all the data from the images and test section reduced to a localised Nusselt number, the accuracy can be calculated with an analysis of the uncertainty of the setup.

## 4.5. High Resolution local heat transfer coefficient data reduction

The temperature field was suitable for the reference annulus, but when the turbulators were present there were data points missing. This was because every image that had a turbulator present in the field of view (as shown previously in Figure 19b) had to be discarded or treated differently. This is because the turbulator rings were not treated with liquid crystal paint, and even if they were, their geometric location away from the wall could not be used determine the wetted wall temperature. Figure 24a shows the low-resolution temperature field of the liquid crystals. As can be seen there are many gaps in the data at the turbulator locations and also along the length where the three supporting wires were. These are represented as white areas. This produced limited data that could be used to identify trends in the heat transfer along the tube length.

A special approach was taken to double the temperature field resolution without the need to take more images. Each image taken during the isothermal calibration was symmetric, for this example in the axial direction, so that the average hue of an image was the same as the average hue on either side of the symmetry plane. This means that for the experimental cases, each image can be divided in two halves as demonstrated in Figure 25, and the calibration curve will still be valid when averaging the hue values. The only effect this splitting procedure had was to half the number of pixels, which increases the uncertainty, but as demonstrated in the uncertainty analysis this effect was negligible.

The temperature field of the turbulator case, using this method to increase the resolution, is shown in Figure 24b with the turbulator interference shown as the white area. There are now more data points in the axial direction, and more importantly, there are more points between the turbulator locations. This method was employed successfully without added experimental time and produces more insight to the temperature fields between turbulators.

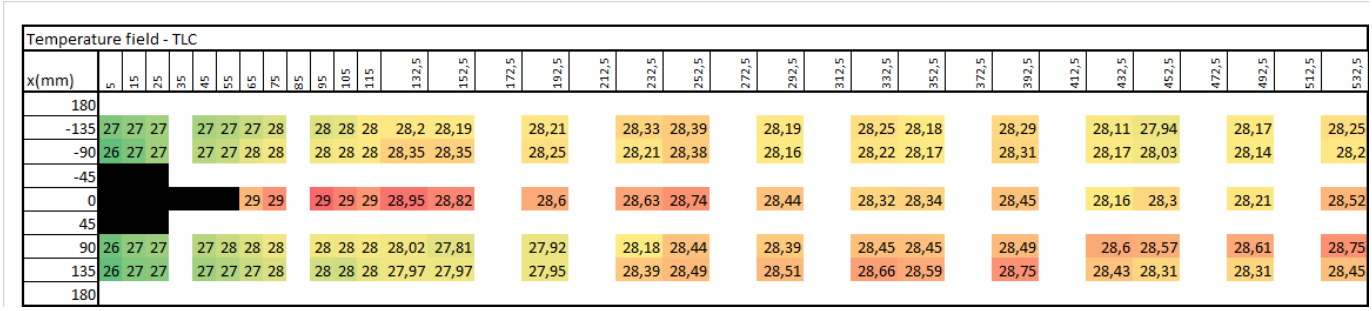


a)

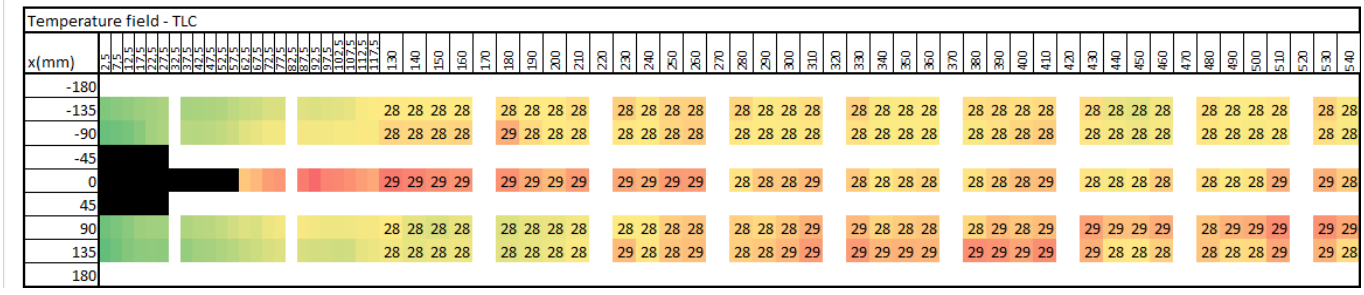


b)

Figure 24: Turbulator case temperature fields (°C) of the liquid crystals at a) low resolution and b) high resolution.

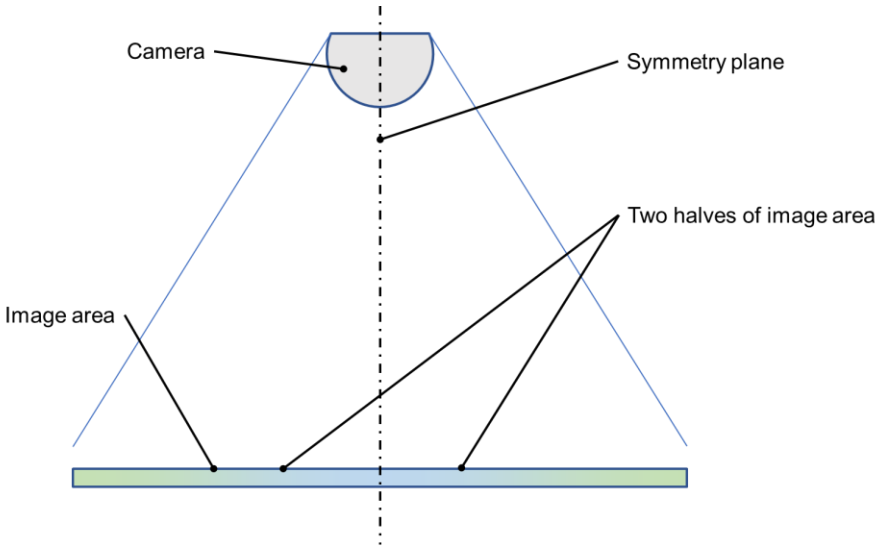


Figure 25: A single image area is divided into two halves to increase temperature field resolution.

The average surface temperature along the axial direction was calculated by averaging the 8 samples around a specific axial location. This will show the temperature increase along the length of the heated rod and was used in the calculation of the heat transfer coefficient.

## 4.6. Uncertainty propagation analysis

According to Moffat (1988), an uncertainty propagation analysis is the process of estimating the effect that individual measurements have on the calculated results. The uncertainty analysis serves as a way to allow future work to be assessed for any significant differences from another study. Because this study used the same setup and techniques used by Kohlmeyer *et al*. (2017), the results of this reference annulus can be compared directly to the previous results to ensure that the liquid crystals have not degraded and will also prove that the methods used are repeatable. The uncertainties calculated are applicable to the reference annulus as well as the annulus with turbulators in as there was no change in equipment used between the two experiments performed.

The equipment measuring accuracies were taken into account. Table 4 lists the measuring range and accuracy for the different components in the test facility. The thermophysical properties used in the processing calculations are listed with their accuracy in Table 5. These property values are prescribed by Popiel and Wojtkowiak (1998). The values listed in Table 4 and Table 5 were used to calculate the overall uncertainties.

Table 4: Equipment used during study with the equipment accuracy.

| **Equipment** | **Range** | **Accuracy** |
|---|---|---|
| Coriolis flow meter | 0.015 kg/s to 0.603 kg/s | 0.11% of reading |
| Measuring tape | 0 mm to 5 000 mm | 1 mm |
| Power supply | 0 V to 360 V<br>0 A to 30 A | 0.2% of reading<br>0.2% of reading |
| PT100 | 0˚C to 100˚C | 0.1°C |
| Single thermocouple | -200˚C to 350˚C | ±0.11˚C |

| | | |
|---|---|---|
| Liquid crystal paint layer pixel | 20˚C to 41˚C | 0.5˚C |

Table 5: Thermophysical properties used and respective uncertainties.

| Property | Range | Accuracy |
|---|---|---|
| $Cp$ | 0°C to 150°C | 0.06% |
| $k$ | 0°C to 150°C | 2.00% |
| $\rho$ | 0°C to 150°C | 0.04% |
| $\mu$ | 0°C to 150°C | 1.00% |

The uncertainty propagation analysis was done according to the method of Moffat (1988). The overall uncertainties of the results were calculated as $\delta R$ in Equation 31. This represents the uncertainty of single measurements of several independent variables. Each variable had its own uncertainty $\delta X_i$ and contributed to the overall uncertainty.

$$\delta R = \left( \sum_{i=1}^{N} \left( \frac{\partial R}{\partial X_i} \delta X_i \right)^2 \right)^{1/2} \quad (31)$$

A consequence of using this method, which has a root-sum-squared term, is that small errors have a small effect compared to large errors. Usually if the smaller terms are smaller by a factor of 3 or more compared to the largest term, the smaller terms can be ignored (Moffat, 1988).

The propagated uncertainties for some variables are listed in Table 6 with the percentage average uncertainty of the average Nusselt number ($\delta Nu_{avg}$) along the tube for the reference case shown. The bulk fluid temperature uncertainties, measured with thermocouples, were reduced drastically by using 8 thermocouples at the measurement location. The same was true with the uncertainties of the images of the liquid crystal paint layer as the high number of pixels, defined in Section 3.4, reduces the liquid crystal paint layer temperature uncertainty.

Table 6: Uncertainty values of some independent variables.

| Reynolds number | $\delta D_h$ (%) | $\delta \dot{Q}$ (%) | $\delta T_b$ (°C) | $\delta T_{ws}$ (°C) | $\delta R_{adh}$ % | $\delta Nu_{avg}$ (%) |
|---|---|---|---|---|---|---|
| 2 043 | 1.91 | 0.28 | 0.107 | 0.27313 | 8.81 | 8.43 |
| 4 077 | | | | | | 12.44 |
| 6 135 | | | | | | 15.25 |
| 7 675 | | | | | | 16.73 |

By far the largest contributor to the overall uncertainties was the thermal resistance of the protective layer of PVC film used to protect the liquid crystals. This had a knock-on effect where the wetted surface temperature has a large uncertainty of 0.273°C. This thermal resistance was previously calculated experimentally by investigating the difference in results between 2 and 3 layers of film used (Kohlmeyer, et al., 2017). It should be noted that for all the experiments performed, the protective PCV layer was never changed and thus the results share the same common uncertainty contributor.

The final uncertainty percentage of the Nusselt number for the reference annulus and turbulator case is plotted in Figure 26a and in Figure 26b respectively, where the change in the uncertainties is seen along the length of the test section. The higher the Reynolds number, the larger the uncertainties become. A larger uncertainty was also seen at the entrance region of the test section where it then decreases. This effect was mainly due to the large uncertainty of the thermal resistance of the PVC layer, when there is a small temperature difference between the PVC layer, the PVC layer uncertainty carries a larger weight. This was evident in the turbulator case where the temperature difference between the wetted surface and liquid crystal paint layer was small, due to an enhancement of the heat transfer coefficients, producing larger uncertainties.

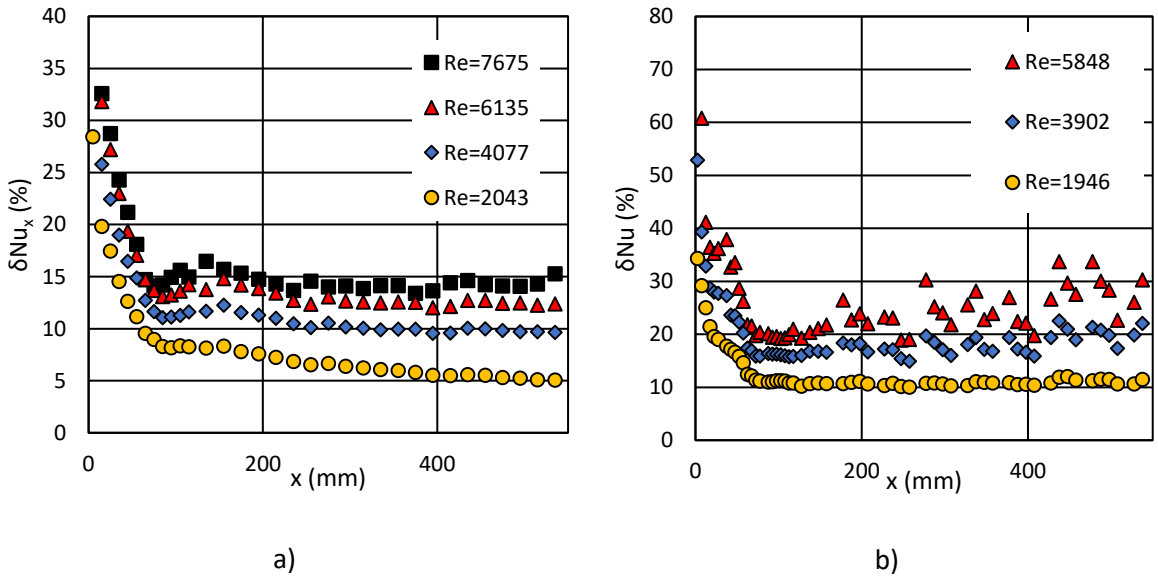


a) b)

**Figure 26: Overall uncertainty of the local Nusselt numbers along the test section length for a) reference annulus and b) annulus containing turbulators.**

## 4.7. Experimental results

### 4.7.1. Reference annulus results

To ensure that the thermochromic liquid crystals have not degraded since the previous experimental runs, the reference case for the current study, which does not have any turbulators, was compared to the previous study. The previous results used in this comparison were obtained from the same experimental setup. To make a direct comparison between the new results and the previous results, proving repeatability, the Reynolds numbers of 2 043, 4 077, 6 135 and 7 675 were compared. Figure 27 shows the local Nusselt number, plotted with the uncertainties of the current results. The results for the reference annulus were also compared to the correlation by Gnielinski (Gnielinski, 2015), shown in Equation 15. Because the Gnielinski correlation was not necessarily developed for a Reynolds number of 2 000, it is not shown at this Reynolds number. It can be seen in both cases that the previous

study results are within the uncertainty bars of the current study. Looking at the overall trend, the Nusselt numbers have the same characteristics of a sharp decrease from the entrance with some local peaks and troughs at the same locations.

The large Nusselt number at the entrance was due to the under-developed boundary layer. Once the boundary layer had developed, from approximately $x > 10D_h$, the Nusselt number stabilises. The same local peaks (mentioned earlier) were also present at $x = 150$ mm, which seem to have small oscillating variations downstream. It is also important to note that the Nusselt number downstream of the entrance, appears to be decreasing along the length of the tube. This is important when the oscillating variations are investigated further in this chapter as there is a large focus on the Nusselt number downstream and not as much in the entrance region.

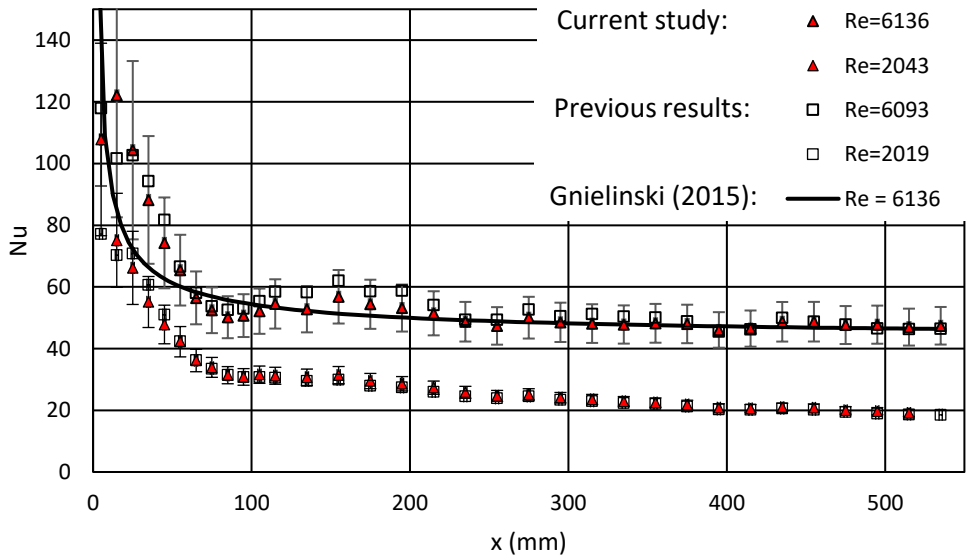


Figure 27: Comparison of local Nusselt number along the length of the reference annulus at two different flow rates.

It can be postulated that the local minimum at $x = 100$ mm and local maximum at $x = 150$ mm could be due to secondary flow induced by buoyancy effects. At the lowest Reynolds number of 2043, the Richardson number was calculated using Equation 5 to be $\mathrm{Ri} = 0.00589 \ll 0.1$. As mentioned previously, natural convection is typically negligible when $\mathrm{Ri} < 0.1$ which indicates that the buoyancy effects are negligible in the ranges of flow rates in this study. As seen in the literature, there are some researchers that found similar anomalies at the entrance region of annuli (Islam, et al., 2001) which would indicate that this effect is also due to natural convection, but in this specific study the magnitude of the local maximum is more pronounced at a higher Reynolds number. This is counterintuitive as the effects of natural convection should decrease with an increase in Reynolds number, indicating that the buoyancy effects are not responsible for the local minimum and maximums.

Looking at the two temperature fields in Figure 28 of the wetted surface for a Reynolds number of 2043 and 7675 respectively, it is clear that the temperature fields around the circumference is not uniform. Both Reynolds numbers show a characteristic hot spot on the top of the tube at approximately 80 mm from the inlet. The test with the higher Reynolds number, however, produces

a larger hot spot than at the lower Reynolds number. There also seems to be a small swirling effect downstream at a higher Reynolds number, although this swirling temperature difference is relatively little at around 0.2°C, while a lower Reynolds number has a more evenly distributed temperature field.

In mixed convection studies, it has been seen that at low Reynolds numbers the temperature is higher on the top of the inner tube while at slightly higher Reynolds numbers the temperature is higher on the bottom of the inner tube. However this was not investigated directly in the entry region of the annulus (Ciampi, et al., 1987), but this effect can still be seen in this study at the higher Reynolds number of 7675.

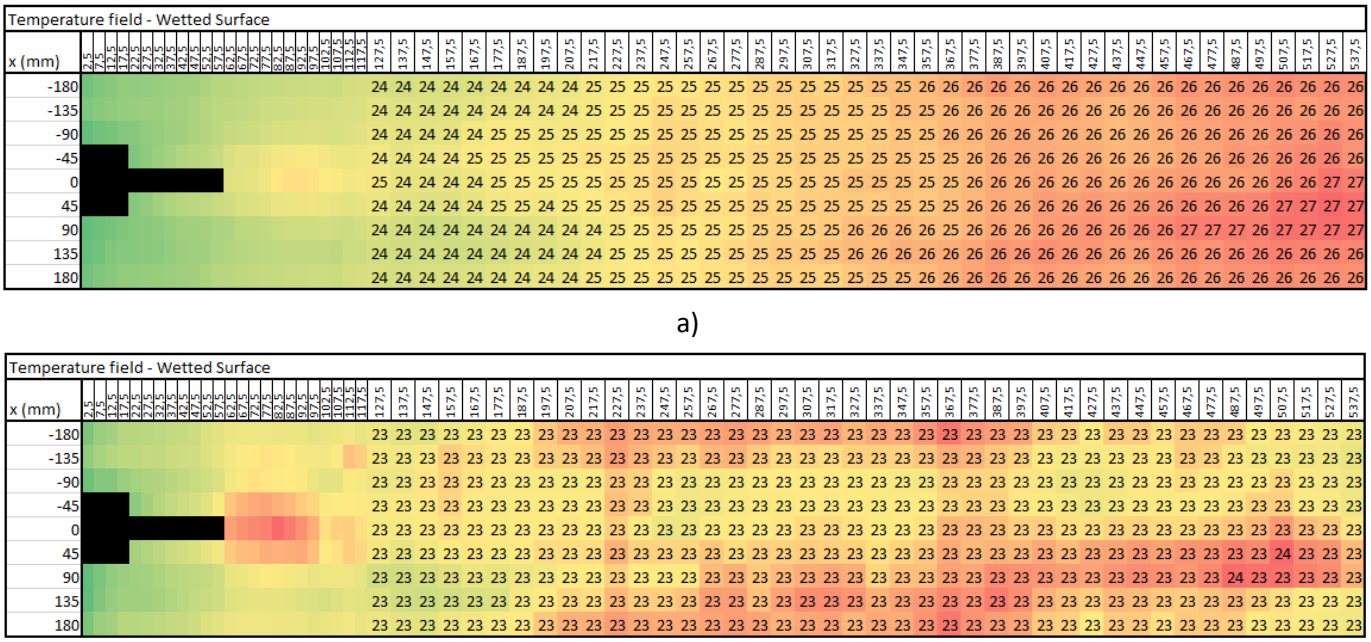


a)




b)

Figure 28: Temperature field (°C) of the wetted surface for a Reynolds number of a) 2043 and b) 7675.

By considering Figure 29, which shows the inlet region of the reference annulus, specifically between $x = 0$ mm and $x = 70$ mm, at a Reynolds number of 2 000, it can be seen that there was a slight disturbance in the Nusselt number trend around $x = 25$ mm, this was seen in both the current study and the previous study. Both studies had an inlet perpendicular to the annulus where the flow impinges on the surface of the inner tube. In impinging studies there is generally a peak in heat transfer between $1.4 < \frac{x}{D_{inlet}} < 2.8$ (Uddin, et al., 2013). This study had an inlet diameter $D_{inlet} = 20$ mm and using this relation a secondary peak could be expected at $28\,mm < x < 56\,mm$. The disturbance at $x = 25$ was probably due to the impingement although it is not in the exact range because the inner tube is not a flat plate as is used in impingement studies.

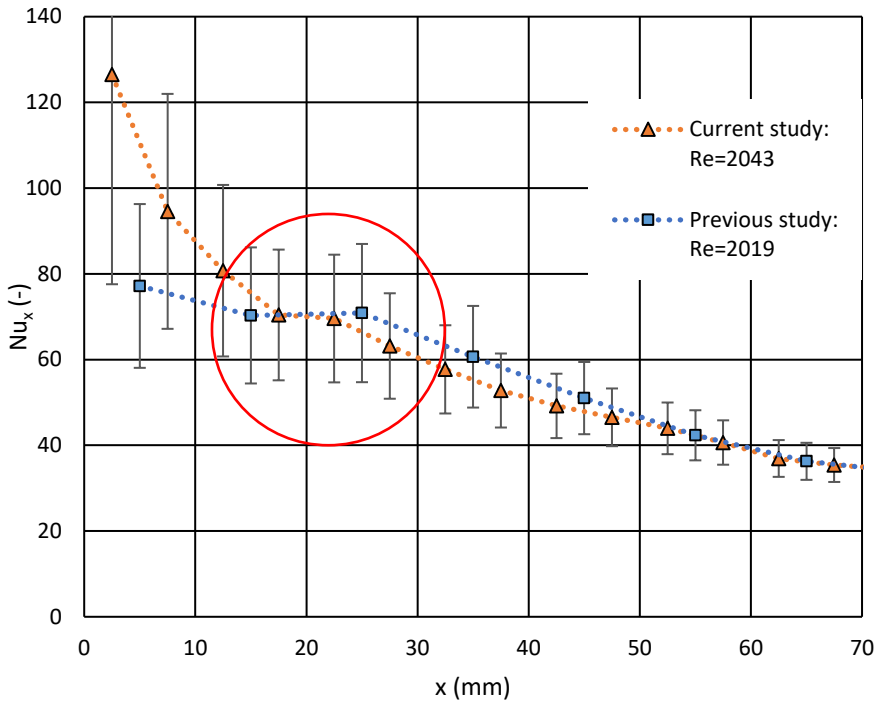


Figure 29: Inlet region of reference annulus at a Reynolds number of 2000.

A comparison was made of the average Nusselt numbers obtained from the current study and the previous study. The Nusselt number was averaged from where the flow is at least 10 hydraulic diameters from the entrance until the end of the test section. The average Nusselt numbers are presented in Figure 30, which includes the average uncertainty in this region. It can be seen that the uncertainties increased as the Nusselt number increased. This was expected because the temperature difference between the wetted surface and the liquid crystal paint layer was small, producing the larger uncertainties. Based on this, it can be concluded that there appears to have been little significant modification of the thermal response of the liquid crystals.

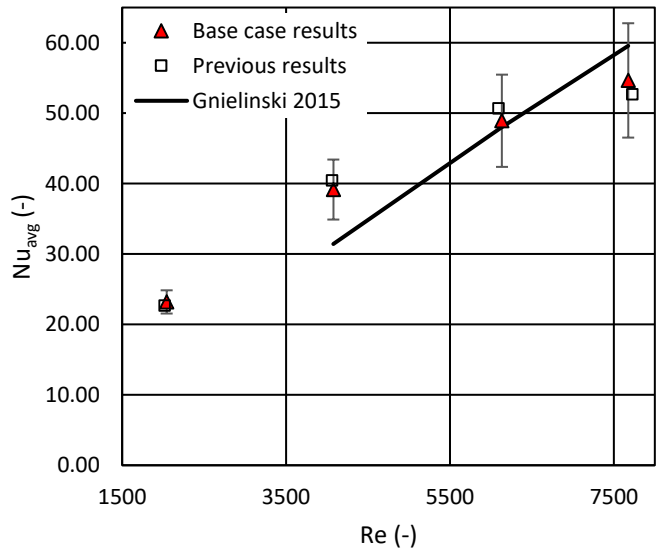


Figure 30: Averaged Nusselt number comparison of the new work and previous work for developed flow.

### 4.7.2. Turbulator test results

The reader is reminded that the inclusion of turbulators is the main purpose of this investigation. For that reason, the relative influence of the turbulator presence on the local wall temperature and the resultant heat transfer coefficients are of importance. Consider Figure 31 which gives a direct comparison of the local Nusselt numbers at a Reynolds number of approximately 1 946 for a case with and without turbulators. For convenience, the turbulator locations are indicated with dash lines. The first turbulator is located at 35 mm from the inlet (there were 11 turbulators present with a pitch of 50 mm separating them).

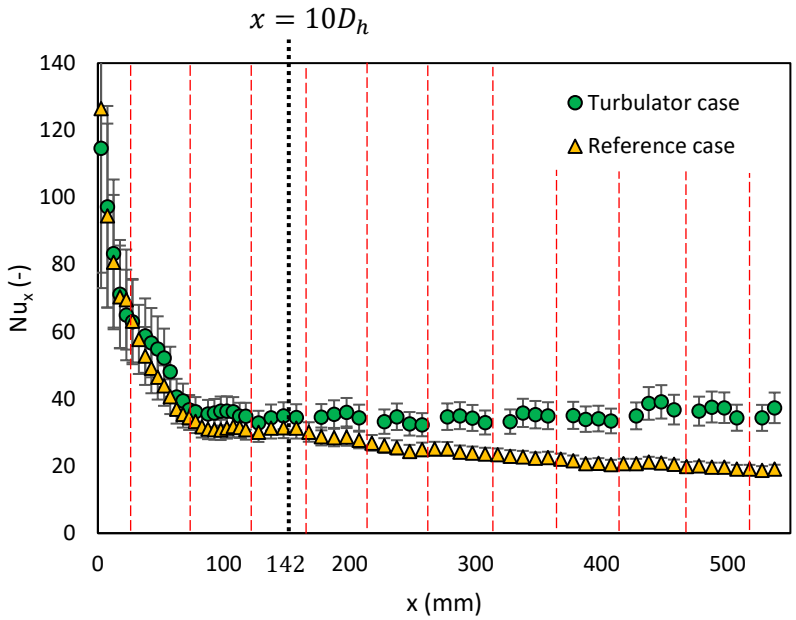


Figure 31: Local Nusselt number at Re=1946 for annuli containing turbulators.

The overall trend of the turbulator case follows the same trend as the reference case. At the inlet there relatively high Nusselt number were present which decreased along the length of the flow passage. Downstream from where the flow would be considered fully developed $x > 142$ mm, the Nusselt number remains relatively constant throughout the test section, with the exception of the small local peaks between turbulators.

As can be seen, there was a significant increase in heat transfer coefficient in the annulus with turbulator rings compared to the reference annulus. For Re = 1 946 the largest improvement occurred at $x$ = 535 mm where the local Nusselt number was approximately twice the Nusselt number without turbulators. At $x = 45$ mm the trend deviated from the reference annulus case; this was because the first ring was located at $x = 35$ mm from the entrance. This indicates that the first ring is the cause of that variation. The Nusselt number of the turbulator cases remains steady without a significant decrease as seen in the reference cases, this indicates that the flow was constantly being disturbed and the boundary layer was not able to developing fully.

Similar comparisons can be made at other Reynolds numbers. For instance, as is shown in Figure 32, a higher Reynolds number of 5 848 is shown. The trend of the Nusselt number along the axial length

was the same as the reference annulus with initially a large decrease in Nusselt number. The effects of the turbulators were, however, much more pronounced at the higher Reynolds number showing that at some locations the maximum enhancement factor was almost 1.5, which is a large improvement over the reference case. Although it was not possible to have derived the Nusselt number directly under the turbulators (due to visual interference), the highest improvement was generally seen directly after a turbulator. The annuli with turbulators had a higher heat transfer performance at every point along the annuli compared to the reference case with the largest performance increase occurring downstream from the inlet.

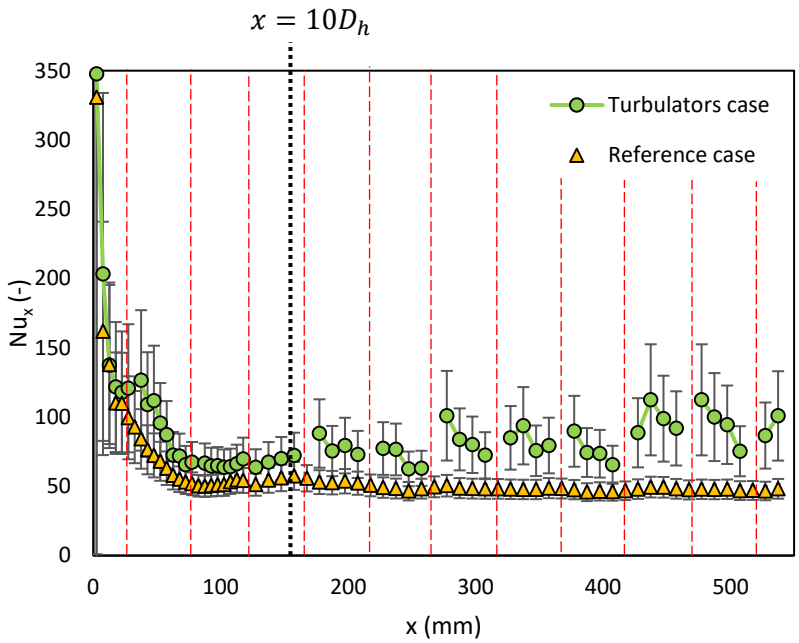


Figure 32: Local Nusselt number at Re=5848 of annuli containing turbulators.

It is thus evident that the mass flow rate played an important role on relative performance of the turbulators. This is also shown in Figure 33 where the local Nusselt numbers for the turbulator cases only, are plotted against each other for Reynolds numbers of 1 949, 3 902, 5 848 and 7 310. It shows that the Nusselt numbers due to the turbulators had larger local maximum amplitudes as the Reynolds numbers increases. There was also a much larger variation in the Nusselt number as the Reynolds number increased, where the local Nusselt number's characteristic trend between turbulators becomes sporadic and is not regular.

The first turbulator was located at approximately $x = 35$ mm which was within the area of developing flow seen by the decrease in local Nusselt number in the entry region. The Nusselt number is already relatively large in this region but it can be seen that the turbulator produces a local disturbance which increases the local Nusselt number directly after it. After the local disturbance, the Nusselt number continues to decrease as the flow develops.

The second turbulator was located at approximately $x = 85$ mm which is where the local minimum was present in the reference annulus. For the Reynolds numbers tested the turbulators increased the Nusselt number at these locations such that the local minimums where not as pronounced.

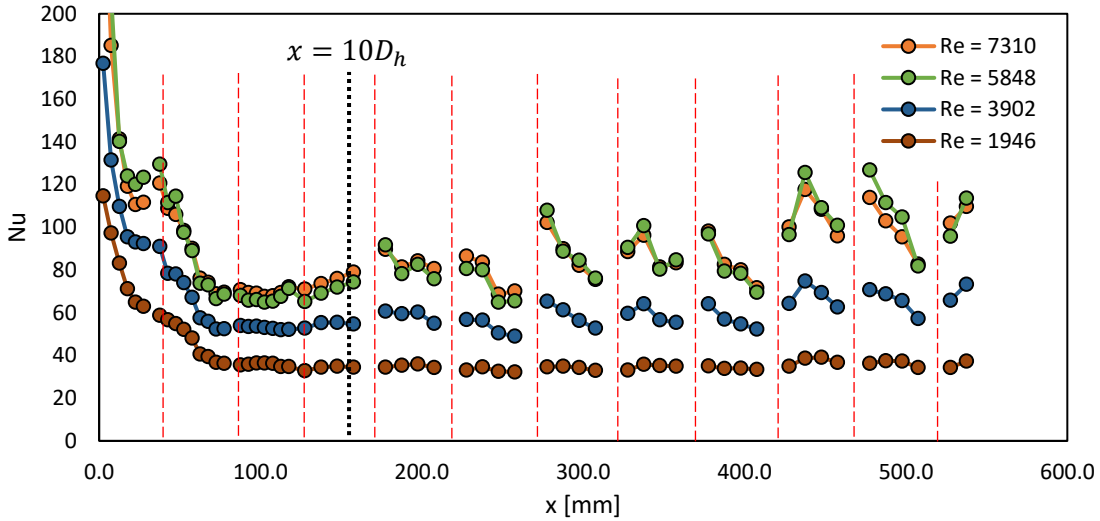


Figure 33: Local Nusselt numbers for the annulus with turbulators at Reynolds numbers of 1946, 3902, 5848 and 7310.

Similarly, a comparison can be made of the average Nusselt numbers as are shown in Figure 34 and listed in Table 7. It is clear that the addition of turbulators increases the average Nusselt number in all cases. The average Nusselt numbers of the reference case and the turbulator case diverged as the Reynolds number increased and the large gains are expected to decrease when the Reynolds number increases. For the two highest Reynolds numbers tested, namely at 5848 and 7310, there is very little change in local heat transfer coefficients where the flow is developed, but there is higher heat transfer before $x = 10D_h$. This could be due the turbulators having less effect on the flow because of the higher turbulence as the Reynolds number increases, but more data is needed to make any conclusion on this. In the experiments performed, the turbulator cases produced high increases enhancement of $\epsilon = 1.85$ at a Reynolds number of 5 848, and the lowest enhancement factor of $1.51$ at a Reynolds number of 1 946. This provides a substantial increase in heat transfer with the addition of a simple flow turbulation device.

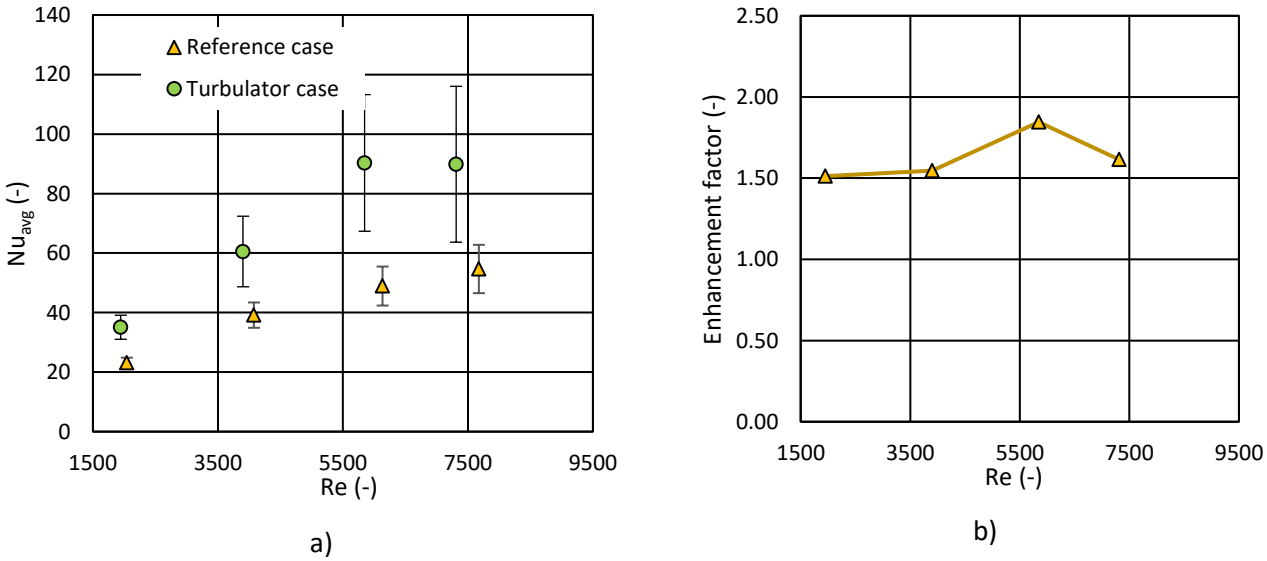


Figure 34: Average experimental a) Nusselt numbers for the reference and turbulator annuli and b) enhancement factor.

Table 7: Average Nusselt numbers of the reference annulus and turbulator cases showing the heat transfer enhancement factor.

| Target Reynolds number | Reference annulus ($Nu_{avg}$) | Turbulators ($Nu_{avg}$) | Heat transfer enhancement factor |
|---|---|---|---|
| 7 500 | 55.64 | 89.85 | 1.61 |
| 6 000 | 48.92 | 90.29 | 1.85 |
| 4 000 | 39.15 | 60.53 | 1.55 |
| 2 000 | 23.20 | 35.08 | 1.51 |

## 4.8. Chapter summary

In this chapter, the methods used to convert the measured data, including liquid crystal thermography images into local heat transfer coefficients was covered. In the reference annulus, local maximum and minimum heat transfer coefficients were present, but could not be attributed to natural convection. Results showed that the experimental setup can reliably reproduce previous experiments, giving confidence in the results. From the experiments, it is clear that the use of eddy promotors in annuli can significantly increase of heat transfer coefficient. The general trend of the turbulators showed that the highest heat transfer coefficient was achieved directly behind the turbulators. The results showed that the local heat transfer coefficient was almost doubled with the addition of turbulators where the average Nusselt number had a maximum improvement of 45.8% compared to the reference annulus without turbulators.

# 5. Numerical models

## 5.1. Introduction

As mentioned, this study consisted of both experimental and numerical work with the main aim to produce sufficient data to suitably characterise and possibly optimise the impact of the turbulator geometry and lay-out. Because it was relatively difficult and expensive to perform vast numbers of experimental test investigations, numerical simulation results were used to extend and compliment the limited experimental data. For this purpose, numerical models were produced to firstly validate this simulation approach by reconsidering the same Reynolds numbers as was used in the experimental investigation for both the reference and turbulator annular passage. Once qualitatively verified, additional models were used to investigate additional turbulator geometric cases.

## 5.2. Computational domain

The computational domain used in the numerical section is different from the experimental section. This was done as there are computational limitations to cell count and the numerical complexity of using the full geometry. Recalling from the experimental investigation, the inlet was 90° to the annulus flow direction, numerically this proves to be a complex problem with impingement on the inner tube which then transitions into the annular flow, among other effects. As will be discussed later, different turbulence models have their own flow characteristics and to choose one that would have provided suitable results for the complex problems with this geometry was not possible.

The domain was three-dimensional as is represented in Figure 35. As can be seen, there were two separate sub-domains: the fluid domain and a solid domain. The solid domain consisted of a stainless-steel inner tube which was included to take the axial heat conduction of the tube into account. The inlet was in the axial direction to produce a pure annular flow without the impingement and recirculation as would have been seen in the experimental test section. The stainless-steel rod dimensions were matched to the experimental test section dimensions and had an outer diameter of $D_1$ = 27.2 mm, while the outer diameter of the annular passage was $D_2$ = 42 mm. The inner diameter of the stainless-steel tube was $D_{HS} = 20.93$ mm and the total length of the numerical geometry was $L_N = 550$ mm.

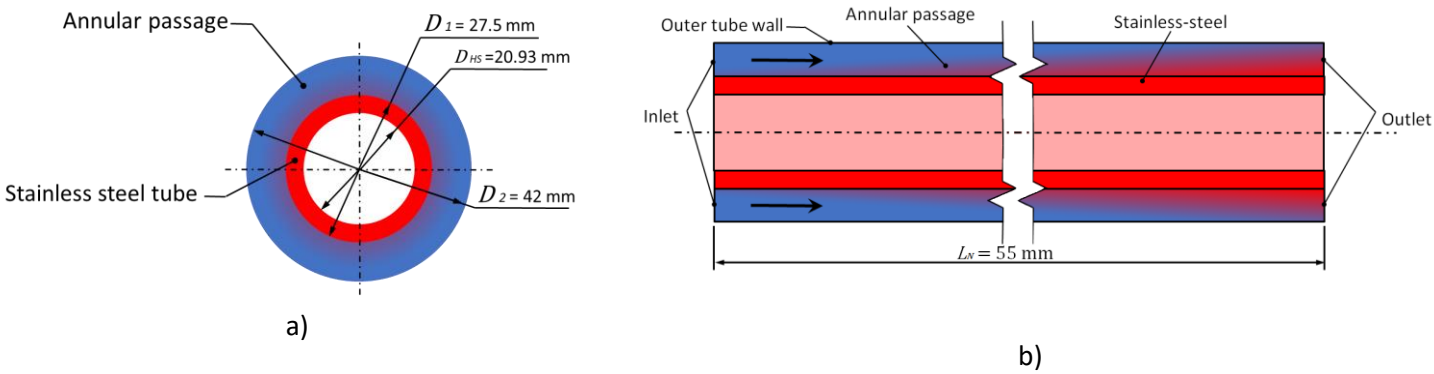


Figure 35: Numerical geometry of reference annulus from a) front and b) side view.

Figure 36 shows a cross section of the numerical case with turbulator inserts. It should be noted that the numerical geometry used for both the reference annulus tests and turbulator case were the same except for the addition of the internal turbulators. This meant the geometry for the turbulator cases was also three-dimensional. The gap ($G$) is the minimum distance between the stainless-steel tube wall and the turbulators and the turbulator diameter ($d$) is shown. The turbulator supporting wires were not added into the numerical model as the added number of cells would have been unfeasible. The results will show the direct influence of the turbulators only and not the support material, although the Reynolds number will change due to this, the effect is negligible and a comparison can still be made with little influence on the results.

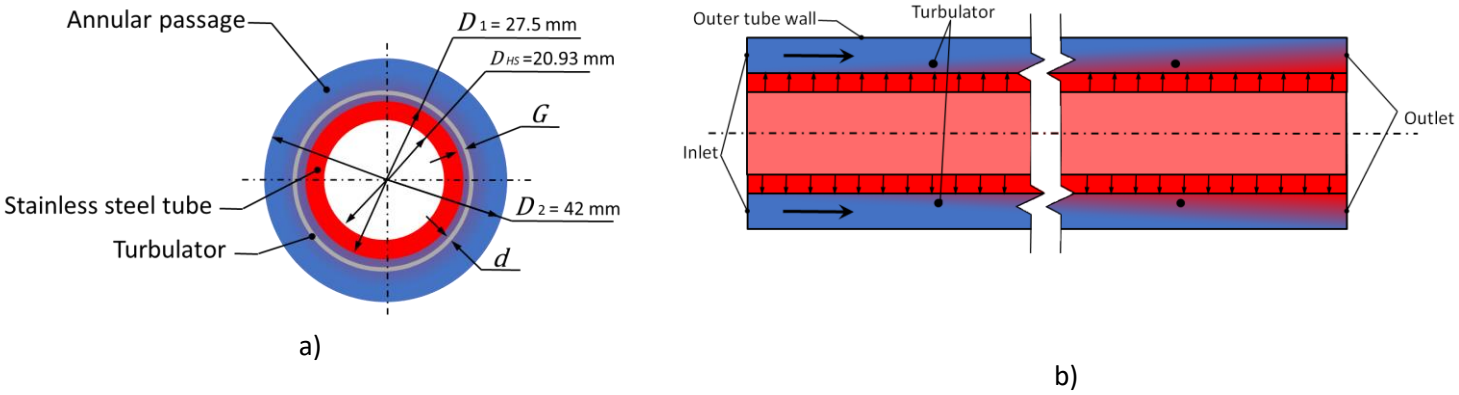


Figure 36: a) Front and b) side cross sectional view of the numerical domain with turbulator inserts.

The density and viscosity of the fluid were dependent on temperature and were considered in the solution. To add temperature dependent properties to the solver, 4$^{th}$ order polynomials were used to represent the property values with respect to temperature in Kelvin. These polynomials were fit to experimental data on water properties (Popiel & Wojtkowiak, 1998). These are shown in Table 8. All the thermo-physical properties of the steel were kept constant.

Table 8: Thermophysical properties of water and steel.

| **Water Properties** | **Equation/Value** |
|---|---|
| $\rho$ (kg/m$^3$) | $78418.32 - 1025.71T + 5.09067T^2 - 0.0112146T^3 + 9.25 \times 10^{-6}T^4$ |
| $c_p$ (j/kg · K) | 4 180 |
| $\mu$ (Pa · s) | $0.455 - 5.267 \times 10^{-3}T + 2.293 \times 10^{-5}T^2 - 4.451 \times 10^{-8}T^3 + 3.245 \times 10^{-11}T^4$ |
| $k$ (W/m · K) | 0.603 |
| **Steel properties** | **Value** |
| $\rho$ (kg/m$^3$) | 8030 |
| $k$ (W/m · K) | 16.27 |
| $c_p$ (J/kg · K ) | 502.48 |

## 5.3. Boundary conditions

The boundary conditions are selected, as far as possible, to represent the same conditions that was in the experimental section. The outer most tube wall was modelled as an adiabatic, insulated wall with

no heat transfer to or around the wall. Although the experimental work had a small amount of heat loss, it was neglected in the numerical sections. This will have a negligible impact when comparing the results between the numerical and experimental sections because the heat loss was small in comparison the heat added.

The turbulator rings were modelled as voids in the annular space, seen in Figure 36b. The boundaries of the turbulators will thus also not have heat transfer to or across them. The addition of solid turbulators increased the cell count by a considerable amount with no additional benefit for the most part. There will be an influence on the results if there was no gap between the wetted surface and turbulators because the turbulators will act as fins on the wetted surface having a higher surface area. In these cases, using a void was still used to produce results that represent the pure convective effects of the turbulators and the effects of increasing the surface area was not considered.

As with the experimental section, a constant heat flux was applied to the inner tube. As can be recalled, the heated rod from the experimental section was built from different material layers, however, the numerical model was setup to only have a stainless-steel tube. The stainless-steel tube was inserted to take heat conduction in the heated rod into account, this will however, not have any significant effect as was shown in the experimental section. To compare directly with the experimental work all the boundary conditions used in the experimental tests were applied to the numerical model as far as possible. The heat flux was adjusted to produce 4994 $W/m^2$ on the inner tube for the turbulator case and 8711 $W/m^2$ for the reference case, which was the same rate of heat transfer that the experimental tests had. The interface between the stainless-steel tube and the fluid are connected with matching meshes.

The inlet boundary condition was modelled as a uniform inlet velocity with a flat velocity profile. This velocity profile was chosen so that the boundary layer development will be visible in the results. In the experimental section, the boundary layer development was clearly visible and using a different velocity profile will not give a complete comparison between the two. From where the fluid enters the numerical domain is where the inlet is matched between the experimental and numerical results. The temperature was adjusted at the different Reynolds numbers such that the same temperature and velocity, that was measured in the experimental investigation, was used in all the numerical simulations. This was done to produce a set of results that can be directly compared with each other and is discussed further in Section 5.6. A pressure-outlet boundary condition was used at the outlet. The flow was not fully developed at the outlet when the turbulators are present and as such this condition was used instead of a regular outflow condition where the condition was more appropriate when the exit flow is close to developed conditions. The walls have a no-slip condition where wall functions are used near the wall and is covered in the next section.

## 5.4. Governing equations

The fluid flow simulation was performed using the ANSYS Fluent 18 solver. The numerical model was created for a steady state condition with a pressure-based solver and water as the working fluid. The differential governing equations for continuity, momentum and energy are listed. These are the conservation equations used under steady and incompressible flow in the numerical model.

Conservation of mass equation:

$$\nabla \cdot (\rho \vec{v}) = 0 \tag{32}$$

Conservation of momentum equation:

$$\nabla \cdot (\rho \vec{v}\vec{v}) = -\nabla \mathrm{P} + \nabla \cdot \bar{\bar{t}} + \rho \vec{g} \tag{33}$$

With the stress tensor being:

$$\bar{\bar{t}} = \mu \left[ (\nabla \vec{v} + \nabla \vec{v}^{T}) - \frac{2}{3} \nabla \cdot \vec{v} I \right] \tag{34}$$

Here $\mu$ is the molecular viscosity and $I$ is a unit tensor.

Conservation of energy equation:

$$\nabla \cdot \left( \vec{v}(\rho E + P) \right) = \nabla \cdot (\mathrm{k_{eff}} \nabla \mathrm{T} - \sum_{j} h_j \vec{J}_j + (\bar{\bar{\tau}}_{eff} \cdot \vec{v}) \tag{35}$$

Here $k_{eff}$ is the effective conductivity defined as $k_{eff} = k + k_t$ with $k_t$ being the turbulent thermal conductivity, and $\vec{J}_j$ is the diffusion flux.

The turbulence in the fluid flow was modelled using a Reynolds-Averaged Navier-Stokes (RANS) formulation. RANS equations compute the flow where the turbulence eddies are modelled rather than resolved like Large Eddy Simulations. This leads to computations that are cheaper to perform compared to direct numerical simulations of the Navier-Stokes equations. The RANS turbulence model chosen in this study was the RNG $k$ - $\varepsilon$ turbulence model as it offers good convergence (Gao, et al., 2017) and is a model with the largest number of applications. The choice of turbulence model also stems from several simulations to see which model fits the experimental data the best. Figure 37 shows the results of 5 turbulence models tested. These are not the only models tested but are the ones shown as there were also different wall functions applied and compared. As seen the RNG $k$ - $\varepsilon$ turbulence model has a good fit to the experimental results.

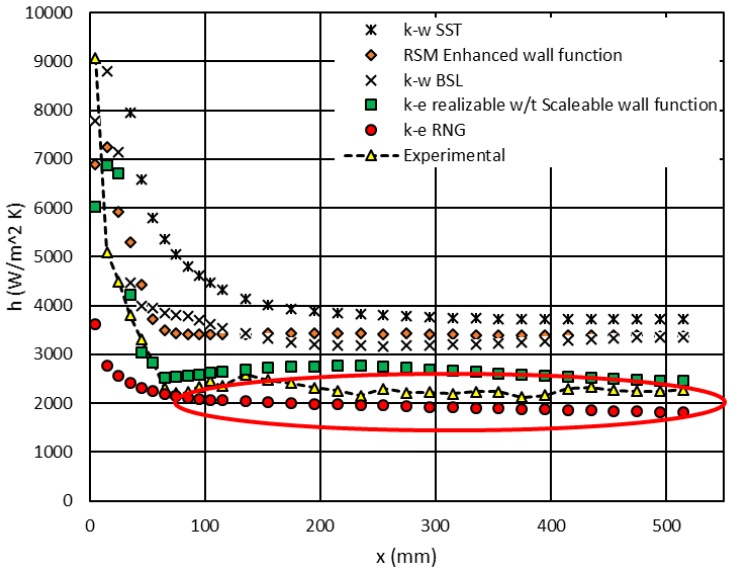


Figure 37: Different turbulence models compared to experimental results for a target Reynolds number of 7500.

The transport equations used in the solver that describe this turbulence model is listed below:

$$\frac{\partial}{\partial t}(\rho k) + \frac{\partial}{\partial x_i}(\rho k u_i) = \frac{\partial}{\partial x_j}\left(\alpha_k \mu_{eff} \frac{\partial k}{\partial x_j}\right) + G_k + G_b - \rho\varepsilon \tag{36}$$

$$\frac{\partial}{\partial t}(\rho \varepsilon) + \frac{\partial}{\partial x_i}(\rho \varepsilon u_i) = \frac{\partial}{\partial x_j}\left(\alpha_\varepsilon \mu_{eff} \frac{\partial \varepsilon}{\partial x_j}\right) + C_{1\varepsilon}\frac{\varepsilon}{k}(G_k + C_{3\varepsilon}G_b) - C_{2\varepsilon}\rho\frac{\varepsilon^2}{k} - R_\varepsilon \tag{37}$$

Where $\mu_{eff}$ is the effective viscosity and the inverse effective Prandtl numbers for $k$ and $\varepsilon$ are represented by $\alpha_k$ and $\alpha_\varepsilon$, respectively. The values for the constants are $C_{1\varepsilon} = 1.42$ and $C_{2\varepsilon} = 1.68$. $G_b$ is the generation of turbulence kinetic energy due to buoyancy, which has the coefficient of expansion already substituted in, described as:

$$G_b = -\frac{1}{\rho}\left(\frac{\partial \rho}{\partial T}\right) g_i \frac{\mu_t}{Pr_t}\frac{\partial T}{\partial x_i} \tag{38}$$

$G_k$ is the turbulence kinetic energy from the mean velocity gradients:

$$G_k = -\rho\overline{u_i' u_j'}\frac{\partial u_j}{\partial x_i} \tag{39}$$

The differential equation for the calculation of the turbulent viscosity is written as:

$$d\left(\frac{\rho^2 k}{\sqrt{\varepsilon\mu}}\right) = 1.72\frac{\hat{v}}{\sqrt{\hat{v}^3 - 1 + C_v}}d\hat{v} \tag{40}$$

Where $C_v \approx 100$ and $\hat{v} = \frac{\mu_{eff}}{\mu}$.

The main change from the standard $k$ - $\varepsilon$ model is the additional term $R_\varepsilon$ described as:

$$R_\varepsilon = \frac{C_\mu \rho \eta^3 \left(1 - \frac{\eta}{\eta_0}\right)}{1 + \beta\eta^3}\frac{\varepsilon^2}{k} \tag{41}$$

Where $C_\mu = 0.0845$, $\eta = Sk/\varepsilon$, $\eta_0 = 4.38$ and $\beta = 0.012$.

The RNG $k$ - $\varepsilon$ turbulence model is similar to the standard $k$ - $\varepsilon$ although there are added refinements that suits this specific problem. The relevant refinements and applicability are discussed:

- The standard $k$ - $\varepsilon$model is a high Reynolds number turbulence model, due to the RNG theory, the effective viscosity is calculated such that the low Reynolds number effects are taken into account. This is very important as the Reynolds numbers tested was in a region of transition where the flow was not laminar but is considered to have low turbulence.
- The effect of swirl on the turbulence was taken into account, although there is no major swirling in the flow, there could be vortex effects trailing the turbulators as seen in literature (Wang & Zhao, 2015).

Buoyancy driven effects are also included in the model. Gravity ($g$) was set at 9.81 m/s$^2$ where the tube geometry was horizontal compared to gravity and the fluid properties are related to temperature. As was calculated in the experimental section, there was no influence from buoyancy effects on the heat transfer, but to keep consistent with the experimental setup, the buoyancy effects

are included in the model by including gravity and density being temperature dependent. As mentioned previously, the density change in the fluid from temperature changes is modelled.

A pressure-based solver was used to solve the equations where a coupled pressure-velocity algorithm was utilised. The numerical scheme consists of second order upwind schemes for the spatial discretisation of the governing equations.

The $k$ - $\varepsilon$ turbulence model has become very popular due to its comparatively low computational cost. One drawback of the model is the over-prediction of the turbulent eddy viscosity close to the wall. To overcome this drawback, the turbulence model was combined with a wall function to model the near-wall solution. There are many wall functions available with the RNG $k$ - $\varepsilon$ turbulence model but the specific one used was the Enhanced Wall Treatment (EWT) equation. This near-wall model uses a method that combines two-layers where if the near-wall mesh was fine enough, the viscosity affected region would be separated from the fully-turbulent region. To resolve the viscous sublayer, a near-wall model approach was taken where the near-wall region was resolved all the way down to the wall. Using this wall function and the near-wall model approach, the mesh should be fine enough to resolve the viscous sublayer sufficiently which typically means that $y^+ \approx 1$.

## 5.5. Mesh

A high-quality mesh is important in any numerical simulation and in this case the mesh was setup in such a way that there was high resolution around the turbulators and inflation layers on the walls. The fluid flows in an axial direction from the inlet to the outlet without complicated bends or flow, for this reason a hexahedral mesh was used. This sub-section covers the mesh details and the mesh dependence study is covered later in Section 6.2.

The mesh parameters were the same for all numerical tests and are listed in Table 9. As can be seen in the table, the body size of the cells are no more than 1 mm in size, which generally in the free stream away from the inflation layers. The mesh has a curvature normal angle of 12°, which can be described as the maximum allowable angle one element may span across a geometries curvature providing good mesh resolution close to the tube wall. This produces the needed mesh refinement around the turbulators. With the mesh around the turbulators sufficiently fine, the growth rate from the turbulators are set at 1.1 to produce a high-quality mesh that captures the flow behind the turbulators.

**Table 9: Mesh parameters used in simulations.**

| **Parameter** | **Value** |
|---|---|
| Body size | 1 mm |
| Curvature normal angle | 12° |
| Global growth rate | 1.10 |
| Inflation layers | 7 |
| Inflation growth rate | 1.19 (Smooth transition) |

As mentioned in the previous section, the $y^+$ value should be approximately 1 to capture the boundary layer sufficiently with this wall function. The inflation layers are used to capture the

boundary layer that was developing on the wall. There were 7 layers that have a smooth transition from inflation layer to the body's element size. The inflation layers produced a first layer thickness of approximately $5 \times 10^{-5}$ mm which will have $y^+ \approx 1$.

The combination of the mesh parameters with inflation layers are seen in Figure 38 where the green part is the fluid area and brown part is the solid tube area. There was a high mesh concentration around the turbulator to capture the flow leading and trailing the turbulator. The inflation layer gets compressed under the turbulator, this was necessary because if the inflation layer was removed from under the turbulator the $y^+$ value will jump to a value in the buffer region producing incorrect results. This effect was checked, and it was deemed necessary to have the inflation layer throughout the domain, the $y^+$ value will be smaller under the turbulator but will not be detrimental to the results.

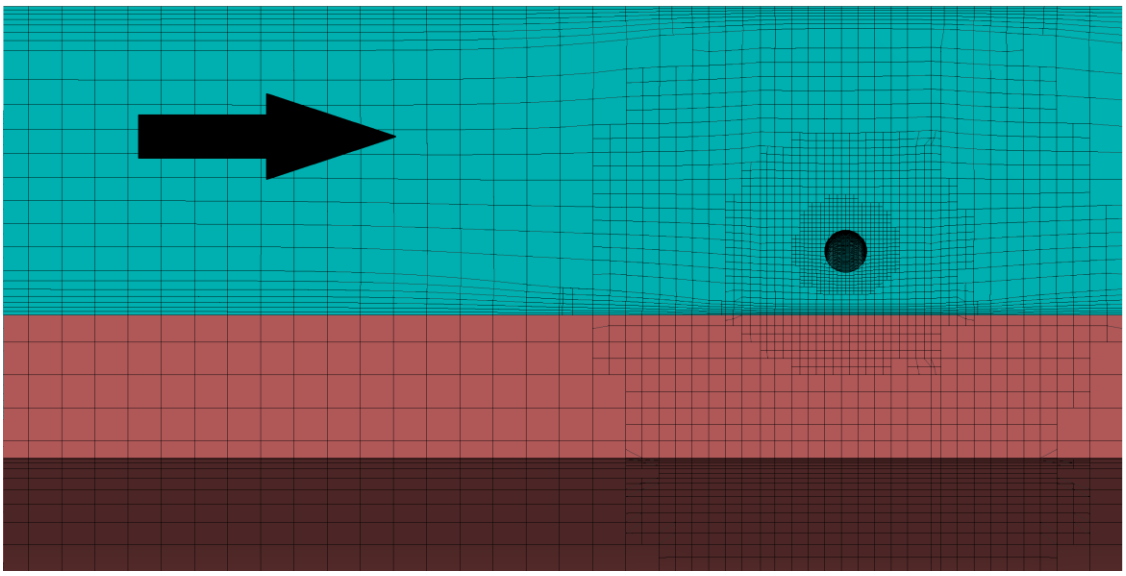

Figure 38: Mesh produced in the computational domain.

The mesh metrics of the mesh that was produced was inspected. The average orthogonality quality was 0.95, which is considered very good, the skewness was at $8.5962 \times 10^{-2}$ and was also good. The average aspect ratio was 2.4. The inflation layers had a larger aspect ratio, but this was in the stream-wise direction and would have still produced good results.

## 5.6. Calculation of heat transfer

To be able to make a comparison between the experimental and numerical results, the local heat transfer coefficient was calculated using the same method as was used in the experimental investigation. It was possible to do this as the inlet conditions of the numerical simulations are the same as the experimental investigations. To get a local temperature profile comparable to the processed images from the experimental section, the surface temperature results were exported from ANSYS into a comma delimited text file. From there a script was used to analyse the cell locations and take the average temperature of the cells in a designated area to produce the familiar local

temperatures, similar as to what was seen in the experimental section. The local heat transfer coefficient was then calculated in the same method as in the experimental section.

The amount of energy added to the annulus was also the same, using this method will produce results that can be directly compared to the experimental results as all the fluid properties are also the same experimentally and numerically. Although the local heat transfer coefficient at the turbulators locations were not visible experimentally, the results was seen numerically and information on what was happening at the turbulator can be investigated.

## 5.7. Chapter summary

In this chapter the computational domain used was created based on a simplified version of the experimental setup, this reduces the complexity of the flow problem. The boundary conditions and the models are setup in such a way so that the same conditions experienced in the experimental investigation can be used to calculate and compare the local Nusselt numbers directly. The RNG $k-\varepsilon$ turbulence model was used with the enhanced wall function to predict the correct boundary layer formation, for which the mesh was setup to utilise a near wall function with $y^+ \approx 1$.

# 6. Numerical validation and results

## 6.1. Introduction

With the numerical models setup and the test matrix defined, the mesh validation was done. With an independent mesh the results of all the numerical tests are covered and discussed. The optimisation results and discussion are done at the end of this chapter.

Due to the computational cost of this investigation, the models were run on a cluster called “Lengau”, using the facilities of the South African Centre for High Performance Computing (CHPC). The initial mesh and model parameters were setup using a local personal computer, after which the case was loaded onto the CHPC’s facilities. All of the models were run using 10 nodes with 24 cores each, giving a total core count of 240 cores used in solving the cases. The average run time for each turbulator case was approximately 45 minutes.

## 6.2. Mesh dependence investigation

A mesh dependence study was performed and was separated into two parts, one for the reference annulus without turbulators and one with the annulus with turbulators. This was done because of the different surface temperature profiles that these geometrical cases give. For the reference annulus, the mesh independence study was done by calculating the average Nusselt number of the annulus from where $x > 10D_h$. As previously mentioned, this is considered to be developed flow. Table 10 lists the results of the reference case with difference cell counts and for a target Reynolds number of 7 500 and 2 000. The difference in Nusselt number decreases as the cell count increases, indicating that the mesh was producing less of an effect on the results. The table lists the percentage difference from the previous mesh and for the finest mesh had a difference of 0.5% for both Reynolds numbers.

Table 10: Results of mesh independence study on the reference case.

| Target Reynolds number | 7500 | | 2000 | |
|---|---|---|---|---|
| Number of cells | Nu | Percentage difference from courser mesh | Nu | Percentage difference from courser mesh |
| 5 902 832 | 46.19 | 0.5% | 17.0 | 0.5% |
| 4 611 440 | 46.44 | 2.1% | 17.1 | 0.7% |
| 3 408 784 | 47.45 | 3.0% | 17.2 | 3.6% |
| 2 040 928 | 48.92 | 7.7% | 17.9 | -1.5% |
| 1 260 240 | 53.02 | | 17.6 | |

Figure 39 plots the results of the average Nusselt numbers shown in Table 10 with respect to the numerical cell count only for a Reynolds number of 7 500. It was seen that the Nusselt number decreases and reaches an asymptotic line as the cell count increases. The mesh was considered to be independent from a cell count of approximately 4.5 million cells. The mesh settings for the case where the mesh was considered independent was used for all the reference case models.

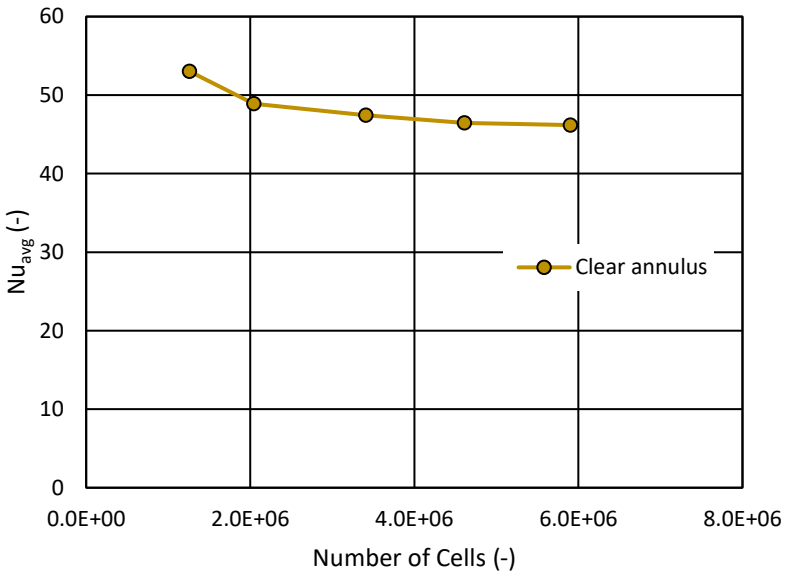


Figure 39: Reference annulus mesh independence study of Nusselt number vs the number of cells.

To do the mesh dependence study of the annulus with turbulators in, a different approach was taken. This was done because the turbulators cases produce two different temperature profiles with different cell counts but have the same average. As seen in Figure 40, the two curves of different cell counts produce a wave shape but the two meshes do not produce the same shape. This presents a problem when averaging the temperature or Nusselt number for a mesh independence study because the average temperature of the two meshes are approximately equal, even though there was clearly no independence. This means that even though it would seem like the Nusselt number was independent from the mesh, this was not the case.

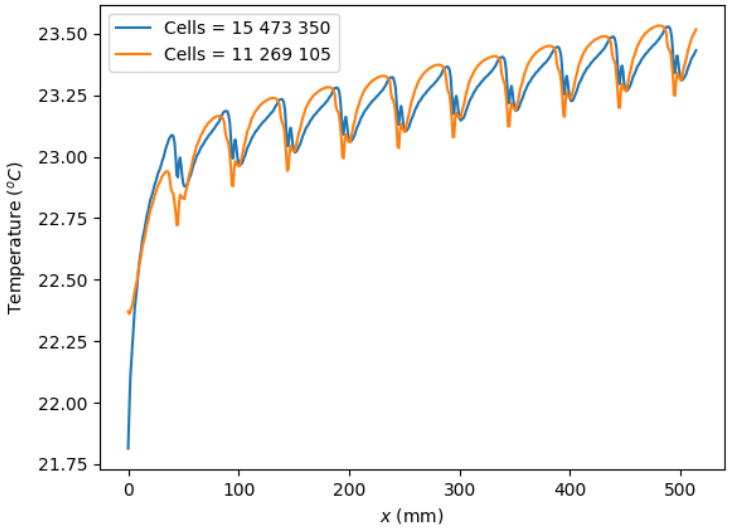


Figure 40: Surface temperature profiles of two meshes with different cell counts.

To check for mesh independence with the turbulator cases, the temperature profiles were compared with each other. Figure 41 shows four different cases with their cell count between approximately 11.3x10$^6$ cells and 16.8x10$^6$ cells. The profiles are for the location of a single turbulator and shows that the mesh was independent from approximately 15 million cells (compare the red and green lines). The temperature profile of the two highest cell counts are the same where the lower cell counts deviate from the high cell count shape. The shape is also similar to literature where there was a decrease in temperature below the turbulator due to accelerating fluid in the gap (Wang & Zhao, 2015).

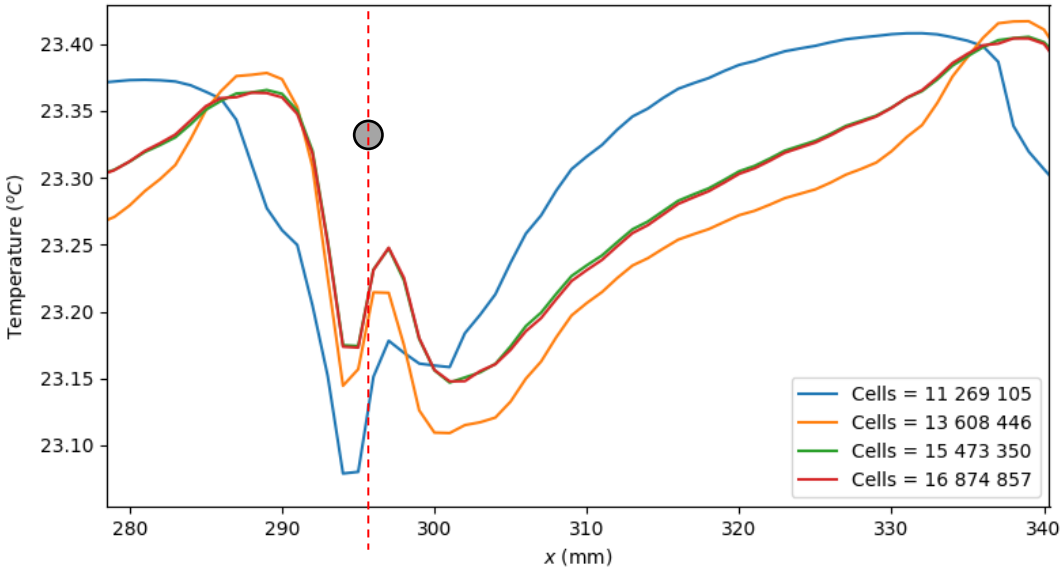


Figure 41: Surface temperature profiles with different mesh counts.

To ensure that the enhanced wall function has a mesh fine enough to captures the viscous sublayer, the $y^+$ values were checked. As covered in the previous chapter, the enhanced wall function was a near wall flow model and the near wall cells should be small enough to produce $y^+ \approx 1$. The $y^+$ for a

high Reynolds number was tested and the wall $y^+$ values are shown in Figure 42. It was seen that due to the inflation layers going under the turbulators, the $y^+$ values are below 1, whereas in the flow downstream of the turbulators the $y^+$ values are around 1.3. This satisfies the criteria that $y^+ \approx 1$ for this wall function

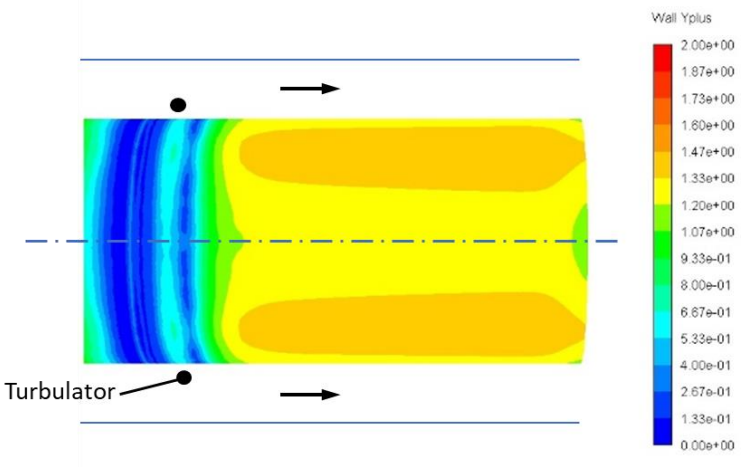


Figure 42: Y plus values on the inner tube of the numerical model at a Reynolds number of 6000.

## 6.3. Numerical test procedure

The geometry was parameterised to allow the geometry to be changed with ease to speed up the production of numerical cases. The geometry was then sent into the ANSYS Meshing where all cases of different geometries are meshed in the same way, with the same conditions, as described in Section 6.2. The newly created mesh was then inspected within the meshing program. Once the mesh was created and all the surfaces were named appropriately, the mesh was uploaded to the cluster, was loaded into ANSYS Fluent, and was run. The convergence criteria were set to be a minimum of 1e-04 for all cases using a journal file containing the instructions for Fluent.

Once a case was completed, an ASCII file of the wetted surface temperature was exported. The numerical data was processed so that the results were in the same format as the experimental data. To calculate the heat transfer coefficient, the processed numerical data uses the same method as the experimental investigation but there was no PVC film influencing the temperature as in the experimental setup.

There are two main goals for the numerical study, to adjust geometrical parameters to describe the impact that a change of geometrical parameters will have on the average and local heat transfer coefficients and characterise the heat transfer enhancement effect of ringed flow turbulators. The numerical test matrix seen in Table 11 is created with these goals in mind. As mentioned previously, the inlet velocities and temperature are the same values used in during the experimental investigation, this was done to be able to investigate the differences in results directly.

Table 11: Numerical test matrix.

| Reynolds number | Pitch (mm) | $d$ (mm) | $G$ (mm) | Inlet temperature (°C) | Heat flux (W/m²) |
|---|---|---|---|---|---|
| 7 627 | 50 | 0.5 | 0.25, 0.5, 1, 1.5, 2, 3, 4 | 21.28 | 4 994 |
| 6 102 | 50 | 0.5 | 0.25, 0.5, 1, 1.5, 2, 3, 4 | 21.08 | 4 994 |
| 4 071 | 50 | 0.5 | 0.25, 0.5, 1, 1.5, 2, 3, 4 | 20.91 | 4 994 |
| 2 030 | 50 | 0.5 | 0.25, 0.5, 1, 1.5, 2, 3, 4 | 20.70 | 4 994 |
| 7 627 | 50 | 1 | 0.25, 0.5, 1, 2, 3, 4 | 21.28 | 4 994 |
| 6 102 | 50 | 1 | 0.25, 0.5, 1, 2, 3, 4 | 21.08 | 4 994 |
| 4 071 | 50 | 1 | 0.25, 0.5, 1, 2, 3, 4 | 20.91 | 4 994 |
| 2 030 | 50 | 1 | 0.25, 0.5, 1, 2, 3, 4 | 20.70 | 4 994 |
| 7 627 | 50 | 1.5 | 0.25, 0.5, 1, 2, 3, 4 | 21.28 | 4 994 |
| 6 102 | 50 | 1.5 | 0.25, 0.5, 1, 2, 3, 4 | 21.08 | 4 994 |
| 4 071 | 50 | 1.5 | 0.25, 0.5, 1, 2, 3, 4 | 20.91 | 4 994 |
| 2 030 | 50 | 1.5 | 0.25, 0.5, 1, 2, 3, 4 | 20.70 | 4 994 |
| 7 627 | 50 | 2 | 0.25, 0.5, 0.75, 1, 1.5, 2, 3, 4 | 21.28 | 4 994 |
| 6 102 | 50 | 2 | 0.25, 0.5, 0.75, 1, 1.5, 2, 3, 4 | 21.08 | 4 994 |
| 4 071 | 50 | 2 | 0.25, 0.5, 0.75, 1, 1.5, 2, 3, 4 | 20.91 | 4 994 |
| 2 030 | 50 | 2 | 0.25, 0.5, 0.75, 1, 1.5, 2, 3, 4 | 20.70 | 4 994 |

The pitch was constant on all the geometries. This was the same pitch used in the experimental investigation. The reason for this was due to the direct effect of the turbulator's geometry on heat transfer and not the number of turbulators in the annulus. The turbulator diameter ($d$) was changed from 0.5 mm to 2 mm. The gap ($G$) between the turbulator and the wetted surface was adjusted from a gap of 0 mm to 4 mm, as the location of the turbulator plays an interesting role in heat transfer by disturbing and being placed in the different boundary layer regions.

## 6.4. Results

### 6.4.1. Reference annulus results

The numerical results for the reference annulus was compared with the experimental results of the reference annulus and to the correlation by Gnielinski (Gnielinski, 2015), shown in Equation 15, in Figure 43 for different Reynolds numbers. As before, because the Gnielinski correlation was not necessarily developed for a Reynolds number of 2 000, it is not shown in at this Reynolds number. The numerical Nusselt numbers were found to also decrease from a high Nusselt number to a lower Nusselt number where it remains constant. Just like the experimental cases, this decrease was due to the boundary layer developing. For all the Reynolds numbers tested, the numerical Nusselt numbers were lower than the experimental results at every point along the annulus. The percentage difference in Nusselt number from the experimental results for the Reynolds numbers of 2 000, 4 000, 6 000 and 7 500 was 26.7%, 27.6%, 20.6% and 15.5% respectively. The numerical results became closer to the experimental results as the Reynolds number increased and at a Reynolds number of 7500 the numerical results were within the experimental uncertainties at some points. The Gnielinski

correlation has Nusselt numbers that fit best with the numerical results for a Reynolds number of 4 000 but increases in error as the Reynolds number increases.

The local maxima or minima which were observed in the experimental results were not present in the numerical results. This could indicate that the localised peaks that are present in the experimental results were due to the inlet used as the inlet impinges on the surface of the inner tube, the trend of having a secondary local peak after the inlet is typically seen in jet impingement studies (Uddin, et al., 2013). Numerically the RNG k-ε turbulence model has a poor to fair secondary peak prediction ability so the peak was not expected in these numerical results (Zuckerman & Lior, 2006).

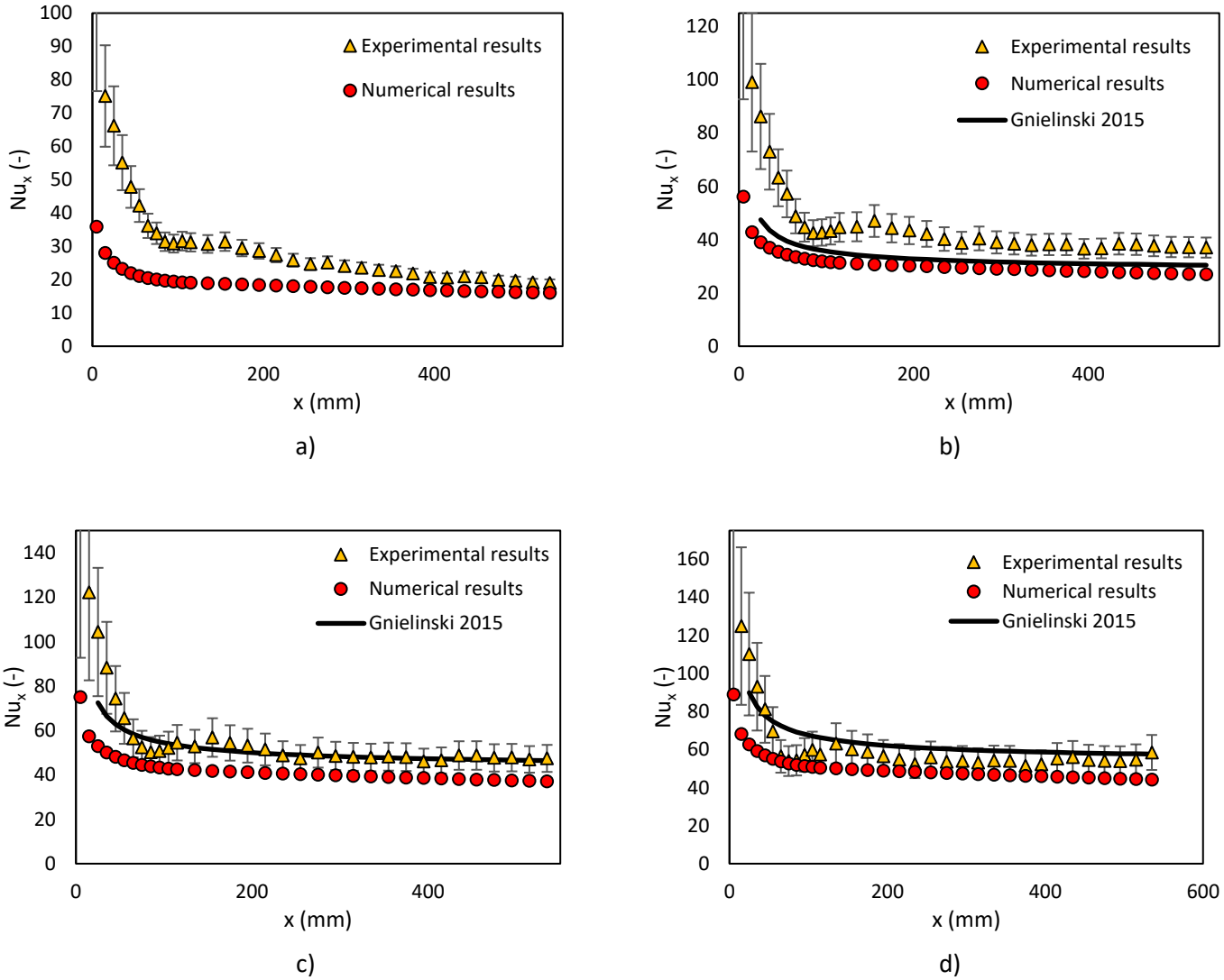


Figure 43: Numerical result comparison of reference annulus at Reynolds numbers of a) 2000, b) 4000, c) 6000, and d) 7500.

Combining the average Nusselt numbers of the reference annulus, again from where the flow was considered developed from where $x > 10D_h$, are plotted in Figure 44. The figure shows the experimental and numerical results increasing with the Reynolds numbers with the Gnielinski

correlation's Nusselt number increasing at a faster rate than the experimental and numerical results. It is important to note that as the Reynolds number increases, the numerical results start to fall within the experimental uncertainties as seen at a Reynolds number of 7 500.

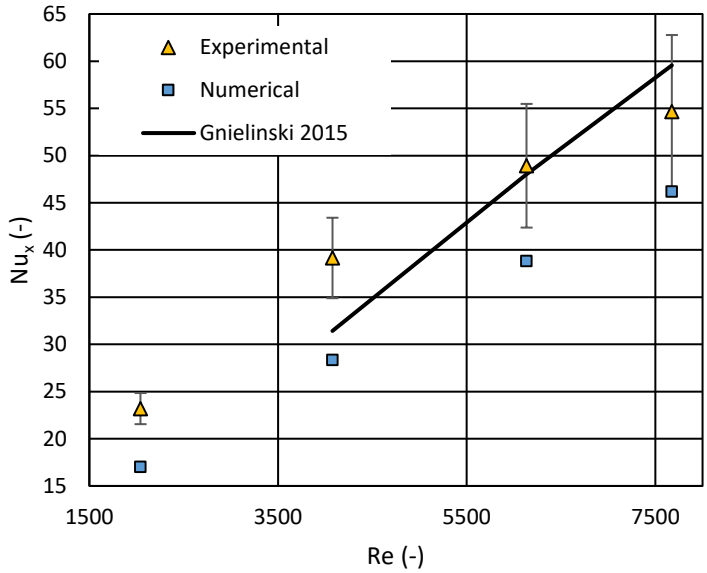


Figure 44: Average Nusselt numbers for the different Reynolds numbers tested.

Table 12 provides the Nusselt numbers for the numerical and experimental results in the reference annulus. It shows that as the Nusselt number increases, the percentage difference between the experimental and numerical results decreases, this is not as obvious when looking at the previous figure. The Reynolds numbers of this investigation was in a complicated region as it was not considered to be high Reynolds numbers and was also not very low to be in the laminar region. It is probable that the difference between the experimental and numerical results will be much smaller at higher Reynolds numbers as the flow will be deep in the turbulent flow regime, but in this study, there was not data in this region.

Table 12: Average Nusselt numbers comparing the numerical and experimental results of a reference annulus.

| **Reference annulus flow** | | | | |
|---|---|---|---|---|
| **Reynolds number** | **Numerical (Nu)** | **Experimental (Nu)** | **Difference from experimental results** | **Experimental uncertainty** |
| 7 675 | 46.2 | 54.7 | 15.5% | 17.0% |
| 6 135 | 38.8 | 48.9 | 20.6% | 15.3% |
| 4 077 | 28.4 | 39.2 | 27.6% | 12.5% |
| 2 043 | 17.0 | 23.2 | 26.7% | 8.3% |

### 6.4.2. Turbulator results

As with the reference annulus, the turbulator results show that the numerical Nusselt numbers for all Reynolds numbers are also underpredicted compared to the experimental results. Figure 45 shows the local Nusselt numbers at two Reynolds numbers, namely 2 000 and 6 000. At a Reynolds number

of 2 000, shown in Figure 45a, the numerical results show some similarities in trend as the experimental results, where there was a consistent wave like trend. Figure 45b however, shows that the numerical results have a smaller scatter compared to the experimental results.

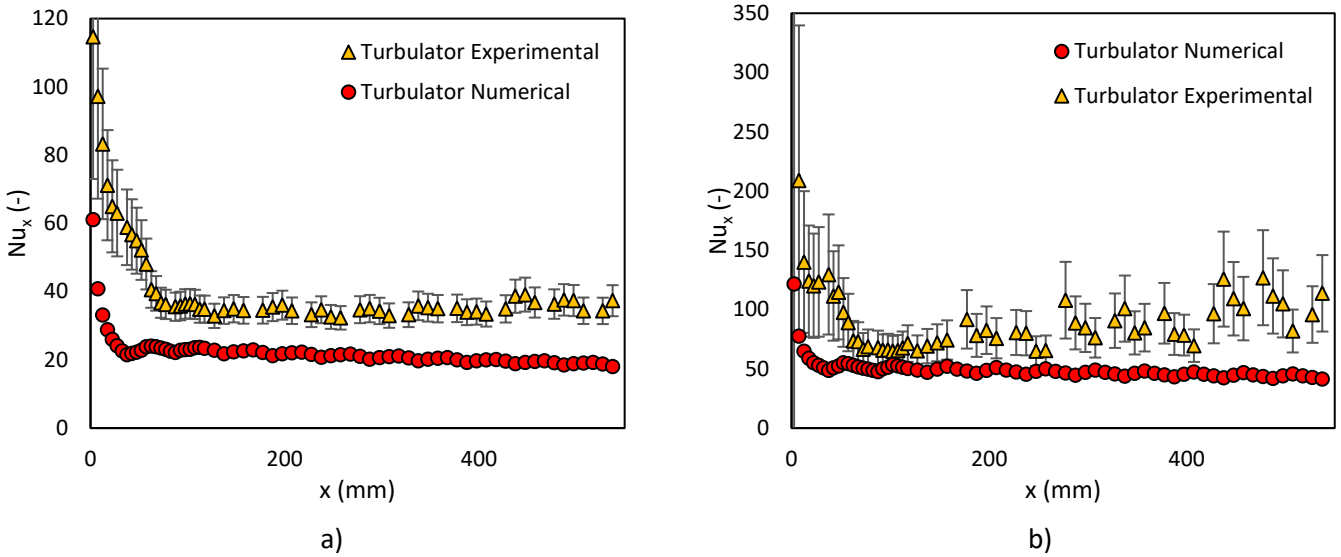


Figure 45: Local Nusselt numbers of the turbulator cases at Reynolds numbers of a) 2000 and b) 6000.

The average Nusselt numbers for the turbulator cases are plotted in Figure 46, both the numerical and experimental results produce trends that increase, but the experimental results have a larger gradient and increases at a higher rate than the numerical results. This produces a challenge to predict the relative performance during optimisation, but because the numerical turbulator cases are underpredicted the trends can still be found by using different Reynolds numbers with only the magnitude being incorrect.

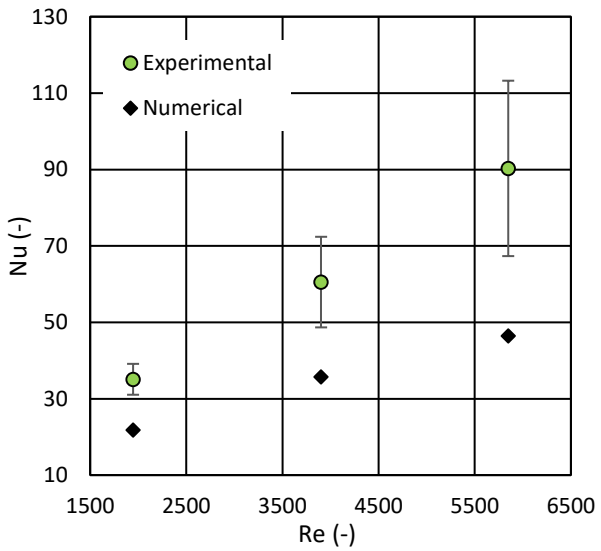


Figure 46: Average Nusselt numbers of the turbulator cases plotted with Reynolds number.

As with the reference annulus, there was a difference in Nusselt number between the numerical and experimental turbulator cases as seen in Table 13. The numerical results also underpredict the Nusselt numbers, but the percentage difference between the numerical and experimental Nusselt numbers increases with an increase in Reynolds numbers. This was opposite to what was seen in the reference annulus cases.

Table 13: Average Nusselt numbers of the turbulator cases.

| Turbulator flow | | | | |
|---|---|---|---|---|
| **Reynolds number** | **Numerical (Nu)** | **Experimental (Nu)** | **Difference from experimental results** | **Experimental uncertainty** |
| 5 848 | 46.48 | 90.29 | 48.5% | 26.7% |
| 3 902 | 35.76 | 60.53 | 40.9% | 19.4% |
| 1 946 | 21.87 | 35.08 | 37.7% | 11.5% |

Figure 47 shows the "Law of the wall" plot with the $u^+$ and $y^+$ values in the annular passage, at a Reynolds number of 6 000, of the outer tube wall and the inner tube wall. Looking at the plot it is clear that the bounded flow was a narrow passage where most of the flow was below a $y^+$ of 120. The flow was completely in the inner layer of the turbulent boundary layer on either side of the annulus. This could indicate the reason behind the underprediction of the Nusselt number as the turbulent viscosity was too low when bounded in this way. With the reference annulus the Nusselt number error was decreasing with an increase in Reynolds number, this was due to the smaller boundary layer forming with the higher flow velocity. A more complete boundary layer was formed with the outer layer having a larger effect being present in both inner and outer boundary layers.

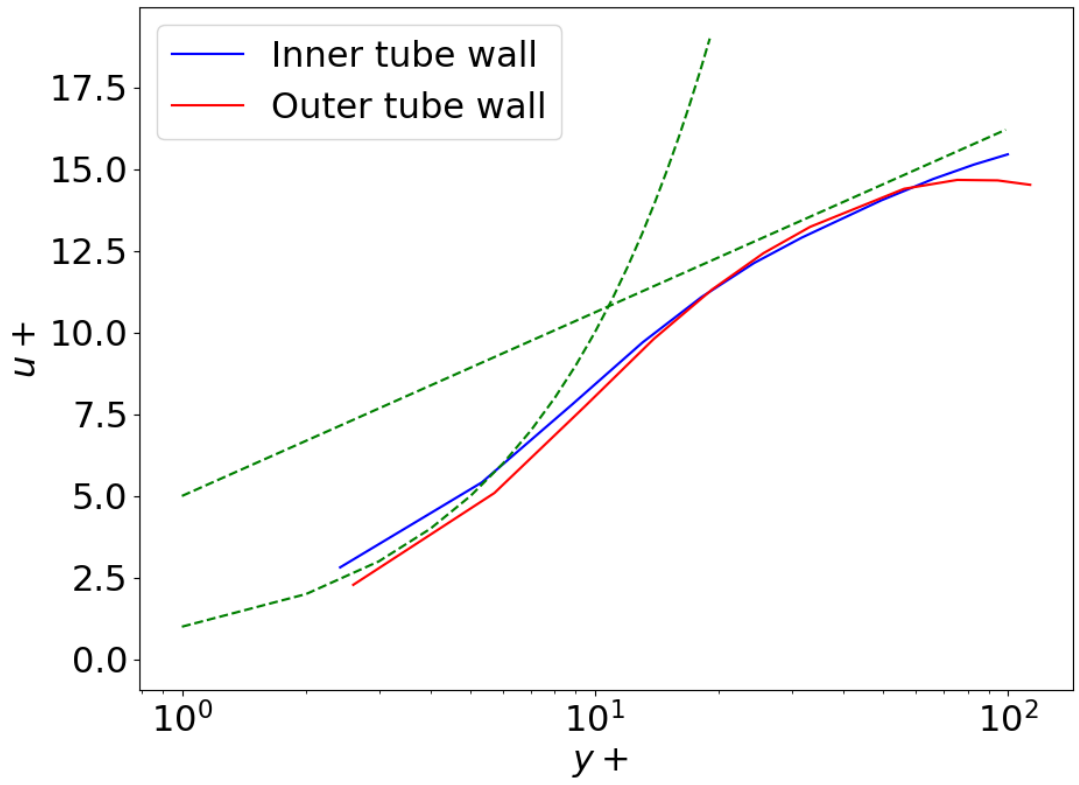


Figure 47: Numerical "Law of the wall" plot at a Reynolds number of 6000.

The discrepancies in Nusselt number results and the effects of the turbulators on surface temperature is also explained by this bounded problem. The turbulators in this case was specifically at a location where $y^+ \approx 30$, this is right on the edge between the buffer layer and the overlap layer. This causes the turbulators to perform poorly due to the wall function. It is good practice to ensure that the first layer $y^+$ value should not be in this buffer region or else large errors can occur (Moukalled, et al., 2016), and it is believed that this was the reason for the discrepancies between the numerical and experimental results.

At the lower Reynolds number of 2 000, the surface temperature shape was similar numerically to the experimental results. At the lower flow rate the turbulators interact more in the viscous sublayer of the boundary which the effects are better recorded compared to in the buffer region. This does not mean that an optimisation was not possible as was explained in the literature review that although CFD turbulence models do not always produce exactly the same results as seen in experimental results, it has been noted that optimisation can take place using CFD (Ferziger & Peric, 2002).

## 6.5. Combined experimental and numerical results

In this section the temperature profiles along the heated tube of the numerical and experimental results are compared. A direct comparison can be made of the effects of the turbulators by the shape of the temperature profiles. This was done using the temperature profiles and not the local Nusselt

numbers because the amplitudes of the temperature profiles are in the same order of magnitude compared to the Nusselt numbers.

To be able to do a comparison between the two results, the local temperatures are transformed and resized into a relative temperature, where the temperature shape is kept, and the average varies at the x-axis. This transformation is done by applying a linear curve fit to the data and the variation above or below the curve is plotted. Figure 48a shows the final transformed relative temperature profiles at a Reynolds number of 2 000. The relative shape of the numerical and experimental profiles shows good agreement with one another. Overall the peaks and troughs caused by the turbulators are in the same locations. This good agreement, as mentioned, also points to the numerical turbulators being in the viscous sublayer producing better results. The resolution of the experimental results was not high enough to see the local peak and trough directly at the turbulator locations.

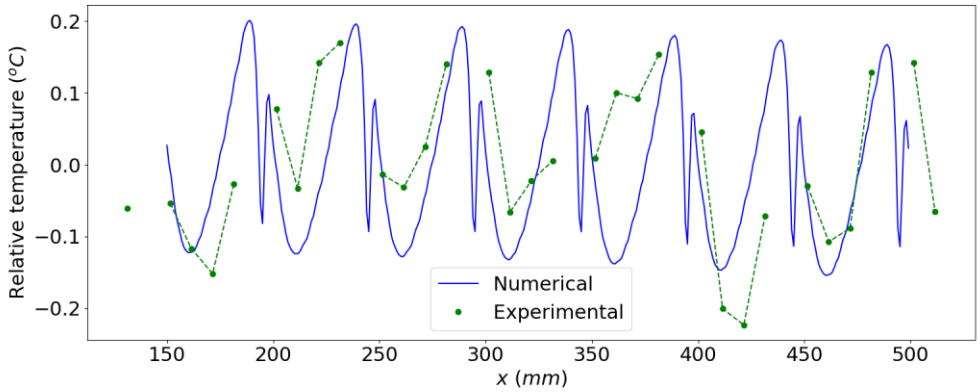


a)

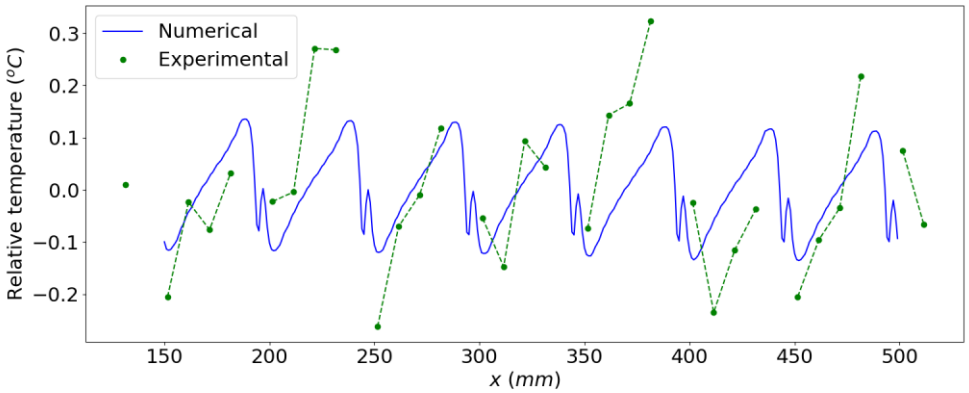


b)

**Figure 48: Normalised temperature distribution of the numerical and experimental results at Reynolds numbers of a) 2000 and b) 6000.**

Figure 48b shows the same adjustment but for a higher Reynolds number of 6 000. The profiles also have the similar trends with more points that are not in alignment with the rest of the profile. It is interesting to see that the wave size increases experimentally with a higher Reynolds number but decreases in the numerical results. This also points to the blending function in the buffer layer reducing the turbulator effects.

### 6.5.1. Optimisation

Optimisation will reveal the generalized effects the turbulators have on the numerical heat transfer coefficient. Although the numerical outputs are not fully in agreement with the experimental result in an absolute sense, we can still find a trend in the relative results that can indicate points of interest and can also be tested in the future. All the cases have the turbulators at a pitch of 50 mm, the only parameters that are changed was the gap, turbulator diameter and Reynolds number.

The first comparison was made by varying the gap size ($G$) at different Reynolds number for a turbulator diameter size ($d$) of 1 mm. The numerical results for this are shown in Figure 49. It can be seen that the turbulator gap size have little impact on the Nusselt number at a Reynolds number of 2 000, but the influence increases with Reynolds number. The highest Reynolds number tested, 7500, shows a minimum Nusselt number at a gap of around 2 mm. This minimum was present in the lower Reynolds numbers of 6 000 and 4 000 but was not as pronounced when the Reynolds number decreases. There was a maximum Nusselt number with small gap sizes and an increasing trend from the minimum at 2 mm as the gap increases, again this was more pronounced as the Reynolds number increases.

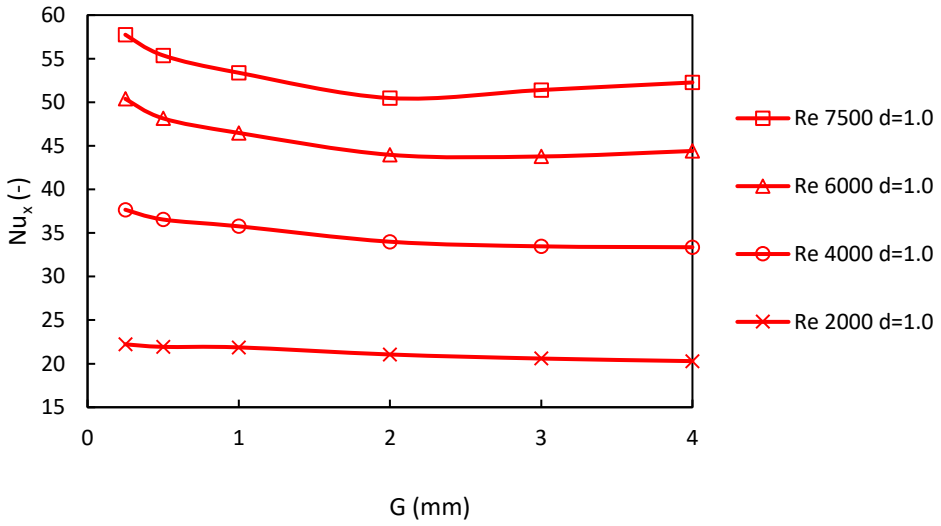


**Figure 49: Numerical results of the Nusselt number response from change in Reynolds number and gap size with turbulator diameter of 1 mm.**

Figure 50a shows the expected effect of the turbulator diameter and changing gap size on the Nusselt number at the low Reynolds number of 2 000. In this case, the turbulators with a diameter larger than 1 mm produce the same trend but the turbulator with a diameter of 0.5 mm deviates from this. Instead of increasing with the smaller gap, the Nusselt number decreases and the turbulator has less of an effect. This was also seen at higher Reynolds numbers in Figure 50b with a Reynolds number of 7 500. Although the Nusselt number does not decrease at this small diameter, it does not have as much of an influence. A larger turbulator diameter consistently produces higher Nusselt numbers, this was probably due to the fluid accelerating between the turbulator and heated wall due to the flow area contracting.

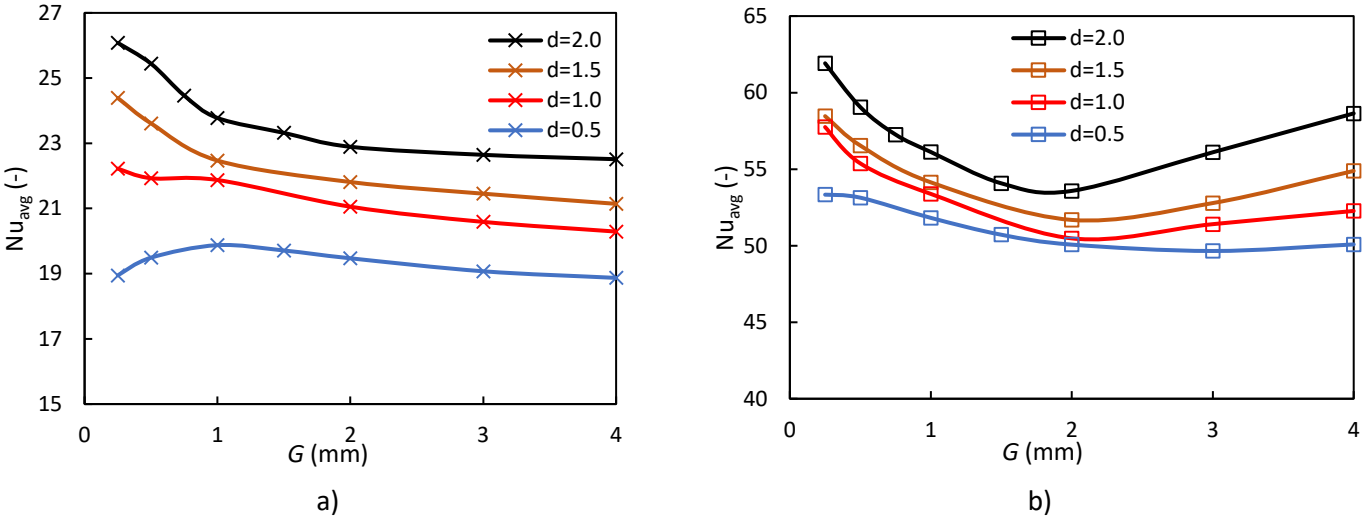


Figure 50: Nusselt number response from change in gap size at different turbulator diameters for Reynolds number a) 2000 and b) 7500.

By plotting all the heat transfer enhancement factor data points available in terms of $G/d$ on a single graph for a Reynolds number of 7 500 and 2 000 (shown in Figure 51) it can be observed that the highest enhancement factor for a Reynolds number of 7 500 and 2 000 was around a gap size of 0, but there was a hint of local peak around $1 < \frac{G}{d} < 3$ at the high Reynolds number. As seen in the literature, a single cylinder in a channel produced the highest Nusselt number in the range $1 < \frac{G}{d} < 3$ (Wang & Zhao, 2015). The results show good correlation to the literature at a $G/d > 1$, but at $G/d \approx 0$ the enhancement factor should decrease.

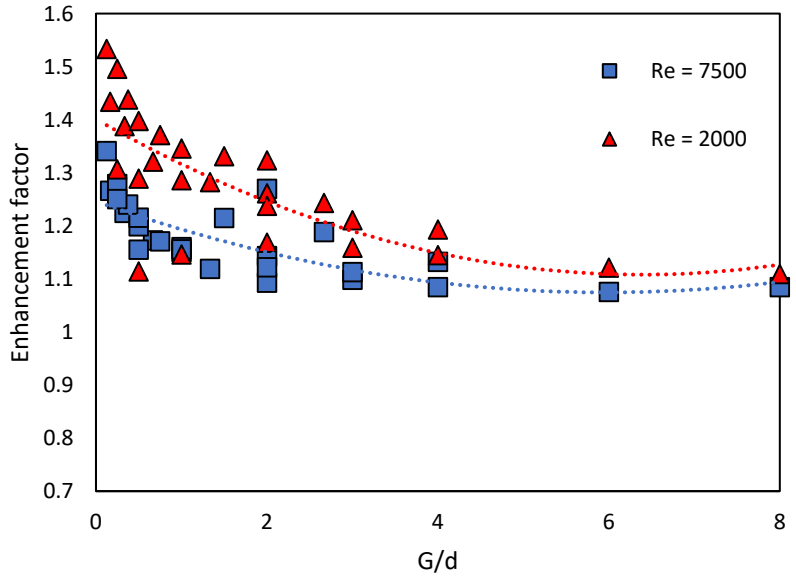


Figure 51: Comparison of G/d for a Reynolds number of 2000 and 7500.

The maximum Nusselt numbers produced was for a turbulator diameter of 2 mm and a gap size of 0.25 mm, for all the Reynolds numbers. As seen in Table 14, the increase in heat transfer factor has a maximum of 1.49 and of 1.34 for a Reynolds number of 2043 and 7675 respectively.

Table 14: Nusselt number results of the geometry that produces the maximum heat transfer.

| Numerical optimization | | | |
|---|---|---|---|
| **Reynolds number** | **Reference annulus (Nu)** | **Maximum turbulator (Nu)** | **% difference** |
| 7 675 | 46.19 | 61.9 | 25.4 |
| 6 135 | 38.82 | 53.8 | 27.8 |
| 4 077 | 28.35 | 41.6 | 31.9 |
| 2 043 | 17.01 | 26.1 | 34.8 |

There was clearly an improvement in Nusselt number when using turbulators in the annulus, but the trade-off was a larger pressure drop in the annulus. The increase in pumping power required can offset the gain in Nusselt number. As seen in Figure 52a, the numerical pressure drop was compared at a Reynolds number of 2 000 and Figure 52b has a Reynolds number of 7 500. At both Reynolds numbers the different turbulator diameters follow the same trends. The pressure drop was smallest when the gap was smallest and then increases with gap size. There was a peak pressure drop at a gap size of approximately 3 mm, where the pressure drop starts decreasing again. This indicates that the largest pressure drop was experienced when the turbulators are in the middle between the outer and inner tubes. Due to the largest Nusselt number being found at the lowest gap size, it is clear that the optimum performance of the annulus with turbulators is found when the turbulators are close to the inner wall.

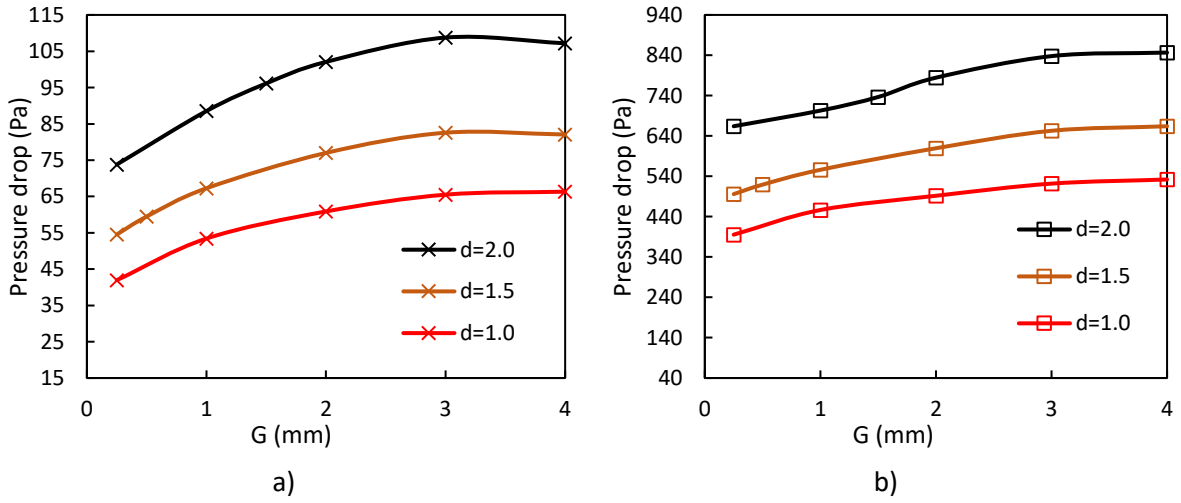


Figure 52: Pressure drop through annuli with turbulators present at a Reynolds number of a) 2000 and b) 7500.

## 6.6. Chapter summary

This chapter covered the numerical test procedure used with the results of the numerical simulations. The reference annulus did not show the local peaks as was present in the experimental results. When looking at the Nusselt number for the different numerical cases it is seen that the highest Nusselt number was at small gap size with the largest Nusselt number increase being 34.8% larger than the reference annulus. At these small gap sizes, the lowest pressure drop was also present, producing the optimum performance of the turbulators in an annulus.

# 7. Summary, future work and conclusion

## 7.1. Summary

The use of circular cross-sectional flow turbulators within an annulus was investigated experimentally and numerically. An experimental test setup was created to investigate the local heat transfer coefficients within an annulus using Liquid Crystal Thermography to map the temperature field on the inner tube's surface. Tests were completed for Reynolds numbers between 2 000 and 7 500 and the investigation was done on a reference annulus as well as an annulus with flow turbulators added. The use of turbulators produced an average heat transfer coefficient increase of 50% over the reference annulus.

Numerical models were developed using a simplified geometry of the annulus with the flow turbulators as well as for the reference annuli. Using the $RNG\ k-\varepsilon$ turbulence model with the enhanced wall function equation, a comparison was made between the experimental results and numerical results. The turbulence model underpredicted the Nusselt numbers in all the cases. This was attributed to the low Reynolds numbers used in this study producing bounded flow within the inner layer of turbulent boundary layers that was difficult to predict numerically.

The response on the Nusselt number due to changing geometrical conditions was also investigated numerically. Using different turbulator diameters and gap sizes as the parameters adjusted, it was found that at low Reynolds numbers the gap size did not have much of an influence in the Nusselt number although the maximum Nusselt numbers were found at small gap sizes. At higher Reynolds numbers a minimum Nusselt number was present when the gap was approximately 2 mm from the heated surface. Overall the best heat transfer occurred with large turbulators and smaller gap sizes. Looking at the pressure drop, the lowest pressure drop was present at small gap sizes in all the cases. The optimum overall performance will be found at small gap sizes that will produce the largest increase in Nusselt number with the lowest pressure drop through the annulus.

## 7.2. Conclusion

The local heat transfer coefficients in annular passages with the addition of flow turbulators was investigated. A set of turbulator ring inserts was successfully designed and constructed for the test setup. A direct comparison between the turbulator cases and the reference annuli was made with the increase in heat transfer due to the turbulators being characterised. Results showed that the experimental setup can reliably reproduce previous experiments, giving confidence in the results. From the experiments, it was clear that the use of eddy promotors in annuli can significantly increase of heat transfer coefficient. The general trend of the turbulators showed that the highest heat transfer coefficient was achieved directly behind the turbulators. The results showed that the local heat transfer coefficient was almost doubled with the addition of turbulators where the maximum improvement had a 1.85 times increase in heat transfer compared to an annulus without turbulators.

The numerical simulations developed under-predicted the Nusselt number at the low Reynolds numbers, with the difference between experimental results and numerical results decreasing as the

Reynolds number increased. This was attributed to the turbulence model not accurately resolving the flow due to the bounded nature of the boundary layer. Changing the turbulators geometrical parameters in the numerical model produced higher Nusselt numbers when the gap between the heated wall and turbulator ring was small. A minimum Nusselt number was present when the gap was approximately 2 mm at the higher Reynolds number, but the largest Nusselt number increase seen was 34.8%. Comparing the pressure drop in the annulus produced an optimum performance with small gap sizes, this had the largest Nusselt number increase and the lowest pressure drop.

An easy method to increase the performance of a tube-in-tube heat exchanger could be the addition of a single turbulator at the entrance region where there is a local minimum present. This will minimise the pressure drop experience but can still increase the heat transfer at the local minimum by a marginal amount.

# References


Agrawal, K. N., Kumar, A., Behabadi Akhavan, M. A. & Varma, H. K., 1998. Heat transfer augmentation by coiled wire inserts during forced convection condensation of R-22 inside horizontal tubes. *International Journal of Multiphase Flow,* 24(4), pp. 635-650.

Akansu, S. O., 2006. Heat transfers and pressure drops for porous-ring turbulators in a circular pipe. *Applied energy,* pp. 280-298.

Bashir, A. I., Everts, M. & Meyer, J. P., 2019. Influence of inlet contraction ratios on the heat transfer and pressure drop characteristics of single-phase flow in smooth circular tubes in the transitional flow regime. *Experimental Thermal and Fluid Science.*

Behnia, M., Parneix, S., Shabany, Y. & Durbin, P. A., 1999. Numerical study of turbulent heat transfer in confined and unconfined impinging jets.. *International journal of heat and fluid flow..*

Bouras, A., Djezzar, M. & Ghernoug, C., 2013. Numerical Simulation of Natural Convection between two elliptical cylinders: Influence of Rayleigh number and Prandtl number. *Energy Procedia,* Volume 36, pp. 788-797.

Cengel, Y. A. & Ghajar, A. J., 2010. *Heat and mass transfer Fundamentals and applications.* New York: Mc Graw Hill.

Choi, H. & Suzuki, K., 2005. Large eddy simulation of turbulent flow and heat transfer in a channel with one wavy wall. *Int. J. Heat Fluid Flow,* Volume 26, pp. 681-694.

Chung, Y. M. & Luo, K. H., 2002. Unsteady heat transfer analysis of an impinging jet.. *ASME journal of heat transfer..*

Ciampi, M., Faggiani, S., Grassi, W. & Tuoni, G., 1987. Mixed convecion heat transfer in horizontal, concentric annuli for transitional flow conditions. *International Journal of Heat and Mass Transfer,* 30(3), pp. 833-841.

Dirker, J. & Meyer, J. P., 2005. Convective heat transfer coefficients in concentric annuli. *Heat transfer engineering,* 26(2), pp. 38-44.

Ferziger, J. H. & Peric, M., 2002. *Computational Methods for Fluid Dynamics.* 3rd ed. Berlin; Heidelberg; New York; Barcelona; Hong Kong; London; Paris; Milan; Tokyo: Springer.

Francis, N. D., Itamura, M. T., Webb, S. W. & James, D. L., 2002. *CFD Calculation of Internal Natural Convection in the Annulus between Horizontal Concentric Cylinders,* Albuquerque,: Sandia National Laboratories.

Frank, M. W., 2006. *Viscous fluid flow.* 3rd ed. New York: McGraw-Hill.

Gao, F., Wang, H. & Wang, H., 2017. *Comparison of different turbulence models in simulating unsteady flow.* Jinan, China, Elsevier Ltd.

Gnielinski, V., 2015. Turbulent Heat Transfer in Annular Spaces—A New Comprehensive Correlation. *Heat transfer engineering.,* 36(9), pp. 787-789.

Haldar, S. C., 1998. Combined convection in developing flow through a horizontal concentric annulus. *Numerical heat transfer,* pp. 673-685.

Islam, N., Gaitonde, U. N. & Sharma, G. K., 2001. Mixed convection heat transfer in the entrance region of horizontal annuli. *International Journal of Heat and Mass Transfer,* Issue 44, pp. 2107-2120.

Jensen, M. V. & Walther, J. H., 2013. Numerical Analysis of Jet Impingement Heat Transfer at High Jet Reynolds Number and Large Temperature Difference.. *Heat transfer engineering..*

Kakade, V. U. & Lock, G. D., 2009. Accurate heat transfer measurements using thermochromic liquid crystal.. *International journal of heat and fluid flow..*

Kohlmeyer, B., Dirker, J. & Meyer, J., 2017. Local heat transfer coefficients at the inlet of an annular flow passage. *International Journal of Heat and Mass Transfer,* Volume 113, pp. 268-280.

Kongkaitpaiboon, V., Nanan, K. & Eiamsa-ard, S., 2010. Experimental investigation of convective heat transfer and pressure loss in a round tube fitted with circular-ring turbulators.. *Heat and mass transfer.*

Lu, G. & Wang, J., 2008. Experimental investigation on heat transfer characteristics of water flow in a narrow annulus. *Applied thermal engineering,* Volume 28, pp. 8-13.

Lundberg, R. E., McCuen, P. A. & Reynolds, W. C., 1963. Heat transfer in annular passages. Hydrodynamically developed laminar flow with arbitrarily prescribed wall temperatures or heat fluxes. *International Journal of Heat and Mass Transfer,* Volume 6, pp. 495-529.

Moffat, R. J., 1988. Describing the uncertainties in experimental results. *Experimental thermal and fluid science,* Volume 1, pp. 3-17.

Mohammed, H. A., Campo, A. & Saidur, R., 2010. Experimental study of forced and free convective heat transfer in the thermal entry region of horizontal concentric annuli.. *Heat and mass transfer..*

Moukalled, F., Mangani, L. & Darwish, M., 2016. *The finite volume method in computational fluid dynamics.* 113 ed. Switzerland: Springer.

Mozley, M. J., 1956. Predicting dynamics of concentric pipe heat exchangers. *Industrial & Engineering Chemistry,* 48(6), pp. 1035-1041.

Obot, N. T. & Esen, E. B., 1989. The role of transition in determining friction and heat transfer in smooth and rough passages.. *International journal of heat and mass transfer..*

Ozceyhan, V., Gunes, S., Buyukalaca, O. & Altuntop, N., 2008. Heat transfer enhancement in a tube using circular cross sectional rings separated from wall. *Applied Energy,* 85(10), pp. 988-1001.

Popiel, C. O. & Wojtkowiak, J., 1998. Simple formulas for thermophysical properties of liquid water for heat transfer calculations. *Heat transfer engineering,* 19(3), pp. 87-101.

Prinsloo, F. P. A., Dirker, J. & Meyer, J. P., 2014. HEAT TRANSFER AND PRESSURE DROP CHARACTERISTICS IN THE ANNULI OF TUBE-IN-TUBE HEAT EXCHANGERS (HORIZONTAL LAY-OUT). *International heat tnrasfer conference..*

Rahnama, M. & Farhadi, M., 2004. Effect of radial fins on two-dimensional turbulent natural convection in a horizontal annulus. *International Journal of Thermal Sciences,* Issue 43, pp. 255-264.

Saha, S. K., Gaitonde, U. N. & Date, A. W., 1989. Heat transfer and pressure drop characteristics of laminar flow in a circular tube fitted with regularly spaced twisted/tape elements. *Experimental Thermal and Fluid Science,* Volume 2, pp. 310-322.

Schulz, S. & Brack, S., 2015. On the effects of coating thickness in transient heat transfer experiments using thermochromic liquid crystals.. *Experimental thermal fluid science..*

Sheikholeslami, M., Ganji, D. D. & Gorji-Bandpy, M., 2016. Experimental and numerical analysis for effects of using conical ring on turbulent flow and heat transfer in a double pipe air to water heat exchanger. *Applied Thermal Engineering,* Volume 100, pp. 805-819.

Sheikholeslami, M., Gorji-Bandpy, M. & Ganji, D. D., 2016. Effect of discontinuous helical turbulators on heat transfer characteristics of double pipe water to air heat exchanger. *Energy Conversion and Management,* Volume 118, pp. 75-87.

Sheikholeslami, M., Gorji-Bandpy, M. & Ganji, D. D., 2016. Experimental study on turbulent flow and heat transfer in an air to water heat exchanger using perforated circular-ring. *Experimental Thermal and Fluid Science,* 70(1), pp. 185-195.

Smith, C. R., Sabatino, D. R. & Praisner, T. J., 2001. Temperature sensing with thermochromic liquid crystals. *Experiments in Fluids,* Volume 30, pp. 190-201.

Spalding, D. B., 1960. A single formula for the "law of the wall". *Journal of Applied Mechanics,* 28(3), pp. 455-458.

Sreenivasulu, T. & Prasad, B., 2009. Flow and heat transfer characteristics in an annulus wrapped with a helical wire. *International Journal of Thermal Sciences,* 48(7), pp. 1377-1391.

Swamee, P. K., Aggarwal, N. & Aggarwal, V., 2008. Optimum design of double pipe heat exchanger. *International journal of heat and mass transfer,* Volume 51, pp. 2260-2266.

Tanda, G., 2001. Heat transfer and pressure drop in a rectangular channel with diamond-shaped elements. *Int J Heat Mass Transfer,* p. 49:3529–41..

Uddin, N., Neumann, S. O. & Weigand, B., 2013. LES simulations of an impinging jet: On the origin of the secondary peak in the Nusselt number distribution. *International Journal of Heat and Mass Transfer,* Volume 57, pp. 356-368.

van der Westhuizen, J. E., Dirker, J. & Meyer, J. P., 2015. IMPLEMENTATION OF LIQUID CRYSTAL THERMOGRAPHY TO DETERMINE WALL TEMPERATURES AND HEAT TRANSFER COEFFICIENTS IN A TUBE-IN-TUBE HEAT EXCHANGER. *Experimental heat transfer..*

Van Zyl, W. R., Dirker, J. & Meyer, J. P., 2013. Single-Phase Convective Heat Transfer and Pressure Drop Coefficients in Concentric Annuli. *Heat transfer engineering..*

Vieira Neto, J. L. et al., 2011. CFD APPLIED TO TURBULENT FLOWS IN CONCENTRIC AND ECCENTRIC ANNULI WITH INNER SHAFT ROTATION. *THE CANADIAN JOURNAL OF CHEMICAL ENGINEERING,* Volume 89, pp. 636-646.

Vujisic, L. B., 1994. *Heat transfer at transition to turbulence in channel flows with eddy promotors.,* Massachusetts: s.n.

Wang, J. & Zhao, Y., 2015. Heat and fluid flow characteristics of a rectangular channel with a small diameter circular cylinder as vortex generator. *International journal of thermal sciences..*

Wiberg, R. & Lior, N., 2004. Errors in thermochromic liquid crystal thermometry. *Review of scientific intruments..*

Yakut, K., Sahin, B. & Canbazoglu, S., 2004. Performance and flow-induced vibration. *Applied Energy,* pp. 65-76.

Yeh, C.-L., 2002. Numerical investigation of the three-dimentional natural convection inside horizontal concentric annulus with specified wall temperature of heat flux. *International Journal of Heat and Mass Transfer,* Issue 42, pp. 775-784.

Zhang, Z., Yu, Z. & Fang, X., 2007. An experimental heat transfer study for helically flowing outside petal-shaped finned tubes with different geometrical parameters. *Applied Thermal Engineering,* 27(1), pp. 268-272.

Zuckerman, N. & Lior, N., 2006. Jet Impingement Heat Transfer: Physics, Correlations, and Numerical Modeling. *Advances in heat transfer..*

# Appendix A

## Local experimental heat transfer coefficients

| | Base Case (no turbulators) | | | | |
|---|---|---|---|---|---|
| | | Reynolds number | | | |
| | | 2043 | 4077 | 6135 | 7675 |
| x (mm) | 2.5 | 126.50 | 213.26 | 330.80 | 325.56 |
| | 7.5 | 94.58 | 132.28 | 161.88 | 171.57 |
| | 12.5 | 80.74 | 109.42 | 137.92 | 139.42 |
| | 17.5 | 70.41 | 90.94 | 110.00 | 113.56 |
| | 22.5 | 69.58 | 91.18 | 109.86 | 115.70 |
| | 27.5 | 63.17 | 81.90 | 99.46 | 105.68 |
| | 32.5 | 57.72 | 76.51 | 92.74 | 98.58 |
| | 37.5 | 52.79 | 69.86 | 84.19 | 88.56 |
| | 42.5 | 49.19 | 64.85 | 76.35 | 83.68 |
| | 47.5 | 46.53 | 61.67 | 72.31 | 79.15 |
| | 52.5 | 43.96 | 59.66 | 68.03 | 72.76 |
| | 57.5 | 40.65 | 54.87 | 63.06 | 66.75 |
| | 62.5 | 36.93 | 50.28 | 57.90 | 57.33 |
| | 67.5 | 35.41 | 47.41 | 55.09 | 55.84 |
| | 72.5 | 34.51 | 45.43 | 53.08 | 54.39 |
| | 77.5 | 33.34 | 43.95 | 51.80 | 53.88 |
| | 82.5 | 31.68 | 42.68 | 50.36 | 54.21 |
| | 87.5 | 31.09 | 42.14 | 49.99 | 54.87 |
| | 92.5 | 30.87 | 42.60 | 50.50 | 56.33 |
| | 97.5 | 30.77 | 42.80 | 50.88 | 58.62 |
| | 102.5 | 31.29 | 42.63 | 51.13 | 60.90 |
| | 107.5 | 31.80 | 43.90 | 53.14 | 59.36 |
| | 112.5 | 31.51 | 44.99 | 54.72 | 56.82 |
| | 117.5 | 30.89 | 44.22 | 54.22 | 58.55 |
| | 127.5 | 30.08 | 43.58 | 51.23 | 62.43 |
| | 137.5 | 31.31 | 46.14 | 54.39 | 64.80 |
| | 147.5 | 31.46 | 47.14 | 56.10 | 62.38 |
| | 157.5 | 31.31 | 46.85 | 57.50 | 58.95 |
| | 167.5 | 30.15 | 45.26 | 55.77 | 58.74 |
| | 177.5 | 28.81 | 43.35 | 53.01 | 59.74 |
| | 187.5 | 28.49 | 43.14 | 52.61 | 57.79 |
| | 197.5 | 28.68 | 43.67 | 53.64 | 56.22 |
| | 207.5 | 27.76 | 42.76 | 52.24 | 55.25 |
| | 217.5 | 26.90 | 41.56 | 50.65 | 55.44 |
| | 227.5 | 26.09 | 40.56 | 49.05 | 52.02 |
| | 237.5 | 25.56 | 39.86 | 48.37 | 53.98 |
| | 247.5 | 24.37 | 38.33 | 46.45 | 56.15 |
| | 257.5 | 24.95 | 39.26 | 48.28 | 56.99 |

| | Turbulators | | | | |
|---|---|---|---|---|---|
| | | Reynolds number | | | |
| | | 1946 | 3902 | 5848 | 7310 |
| x (mm) | 2.5 | 114.67 | 176.73 | 363.75 | 278.22 |
| | 7.5 | 97.23 | 131.45 | 209.03 | 185.08 |
| | 12.5 | 83.28 | 109.73 | 140.13 | 141.35 |
| | 17.5 | 71.18 | 95.55 | 123.98 | 119.22 |
| | 22.5 | 64.99 | 93.12 | 120.13 | 110.64 |
| | 27.5 | 63.01 | 92.40 | 123.35 | 111.64 |
| | 32.5 | | | | |
| | 37.5 | 58.83 | 91.02 | 129.59 | 120.67 |
| | 42.5 | 56.73 | 78.45 | 111.50 | 108.88 |
| | 47.5 | 54.91 | 78.09 | 114.52 | 105.99 |
| | 52.5 | 52.17 | 74.06 | 97.59 | 98.46 |
| | 57.5 | 48.07 | 67.13 | 89.08 | 90.16 |
| | 62.5 | 40.61 | 57.51 | 73.73 | 76.17 |
| | 67.5 | 39.47 | 55.89 | 72.94 | 74.27 |
| | 72.5 | 36.73 | 52.36 | 66.57 | 68.85 |
| | 77.5 | 36.24 | 52.44 | 68.67 | 69.51 |
| | 82.5 | | | | |
| | 87.5 | 35.56 | 54.05 | 68.01 | 70.79 |
| | 92.5 | 35.77 | 53.60 | 65.76 | 69.43 |
| | 97.5 | 36.37 | 53.68 | 66.16 | 69.13 |
| | 102.5 | 36.43 | 53.11 | 64.92 | 67.62 |
| | 107.5 | 36.23 | 52.63 | 65.41 | 67.94 |
| | 112.5 | 34.85 | 52.00 | 67.57 | 69.40 |
| | 117.5 | 34.84 | 52.23 | 71.32 | 72.18 |
| | 127.5 | 32.88 | 52.78 | 65.24 | 71.05 |
| | 137.5 | 34.42 | 55.34 | 69.16 | 73.58 |
| | 147.5 | 34.97 | 55.49 | 71.98 | 76.08 |
| | 157.5 | 34.49 | 54.74 | 74.33 | 79.06 |
| | 167.5 | | | | |
| | 177.5 | 34.53 | 60.76 | 91.77 | 89.59 |
| | 187.5 | 35.45 | 59.47 | 78.22 | 81.37 |
| | 197.5 | 36.01 | 60.29 | 82.61 | 84.25 |
| | 207.5 | 34.38 | 55.02 | 75.82 | 80.72 |
| | 217.5 | | | | |
| | 227.5 | 33.21 | 56.79 | 80.67 | 86.47 |
| | 237.5 | 34.67 | 56.53 | 80.05 | 83.70 |
| | 247.5 | 32.57 | 50.60 | 64.93 | 68.61 |
| | 257.5 | 32.30 | 49.03 | 65.47 | 70.24 |

| | | | | | |
|---|---|---|---|---|---|
| 267.5 | 25.16 | 40.30 | 49.62 | 54.47 |
| 277.5 | 25.12 | 40.56 | 50.41 | 54.19 |
| 287.5 | 24.20 | 39.12 | 48.67 | 54.83 |
| 297.5 | 23.93 | 38.81 | 48.32 | 54.75 |
| 307.5 | 23.61 | 38.42 | 48.06 | 53.98 |
| 317.5 | 23.43 | 38.53 | 48.14 | 53.87 |
| 327.5 | 22.99 | 38.04 | 47.86 | 54.41 |
| 337.5 | 22.80 | 37.81 | 47.73 | 55.76 |
| 347.5 | 22.40 | 37.92 | 47.70 | 55.42 |
| 357.5 | 22.57 | 38.44 | 48.67 | 54.70 |
| 367.5 | 22.09 | 38.51 | 48.39 | 51.90 |
| 377.5 | 21.59 | 37.86 | 47.57 | 52.71 |
| 387.5 | 20.72 | 36.40 | 45.77 | 52.66 |
| 397.5 | 20.89 | 36.69 | 46.31 | 53.81 |
| 407.5 | 20.45 | 36.49 | 46.17 | 55.38 |
| 417.5 | 20.73 | 36.90 | 46.78 | 57.52 |
| 427.5 | 20.71 | 38.02 | 47.96 | 58.19 |
| 437.5 | 21.24 | 38.91 | 49.42 | 56.58 |
| 447.5 | 20.96 | 38.61 | 49.25 | 55.35 |
| 457.5 | 20.52 | 37.90 | 48.17 | 56.31 |
| 467.5 | 19.89 | 37.35 | 47.40 | 55.39 |
| 477.5 | 20.05 | 37.98 | 47.86 | 55.25 |
| 487.5 | 19.69 | 37.17 | 47.63 | 54.79 |
| 497.5 | 19.70 | 37.29 | 47.85 | 55.81 |
| 507.5 | 19.10 | 37.07 | 46.90 | 54.82 |
| 517.5 | 19.12 | 37.26 | 47.00 | 57.62 |
| 527.5 | 18.77 | 36.49 | 46.63 | 58.52 |
| 537.5 | 19.15 | 37.53 | 48.17 | 62.12 |

| | | | | | |
|---|---|---|---|---|---|
| 267.5 | | | | |
| 277.5 | 34.68 | 65.32 | 107.92 | 102.24 |
| 287.5 | 34.99 | 61.27 | 88.77 | 90.02 |
| 297.5 | 34.31 | 56.39 | 84.55 | 82.17 |
| 307.5 | 32.95 | 52.82 | 76.20 | 75.56 |
| 317.5 | | | | |
| 327.5 | 33.21 | 59.71 | 90.62 | 88.56 |
| 337.5 | 35.81 | 64.18 | 100.82 | 96.23 |
| 347.5 | 35.28 | 56.65 | 80.32 | 81.49 |
| 357.5 | 34.98 | 55.53 | 84.75 | 83.40 |
| 367.5 | | | | |
| 377.5 | 35.07 | 64.25 | 96.90 | 98.25 |
| 387.5 | 33.94 | 56.96 | 79.39 | 82.64 |
| 397.5 | 34.11 | 54.78 | 78.49 | 80.07 |
| 407.5 | 33.41 | 52.37 | 69.57 | 71.67 |
| 417.5 | | | | |
| 427.5 | 34.92 | 64.28 | 96.51 | 100.22 |
| 437.5 | 38.62 | 74.87 | 125.70 | 117.67 |
| 447.5 | 39.08 | 69.46 | 109.15 | 108.46 |
| 457.5 | 36.77 | 62.73 | 100.84 | 95.88 |
| 467.5 | | | | |
| 477.5 | 36.32 | 70.75 | 126.88 | 113.93 |
| 487.5 | 37.55 | 68.88 | 111.49 | 103.06 |
| 497.5 | 37.34 | 65.60 | 104.81 | 95.55 |
| 507.5 | 34.36 | 57.26 | 81.92 | 82.75 |
| 517.5 | | | | |
| 527.5 | 34.32 | 65.89 | 95.82 | 101.95 |
| 537.5 | 37.30 | 73.25 | 113.71 | 109.71 |

## Local numerical heat transfer coefficients

| | Reference Case (no turbulators) | | | | |
|---|---|---|---|---|---|
| | | Reynolds number | | | |
| | | 2043 | 4077 | 6135 | 7675 |
| $x$ (mm) | 5 | 35.85 | 56.13 | 74.95 | 88.79 |
| | 15 | 27.97 | 42.83 | 57.32 | 68.03 |
| | 25 | 25.06 | 39.04 | 52.85 | 62.65 |
| | 35 | 23.18 | 36.90 | 50.01 | 59.17 |
| | 45 | 21.96 | 35.45 | 48.02 | 56.79 |
| | 55 | 21.07 | 34.32 | 46.48 | 54.97 |
| | 65 | 20.43 | 33.44 | 45.31 | 53.60 |
| | 75 | 19.98 | 32.79 | 44.44 | 52.60 |
| | 85 | 19.65 | 32.27 | 43.77 | 51.82 |
| | 95 | 19.38 | 31.85 | 43.22 | 51.20 |
| | 105 | 19.18 | 31.52 | 42.80 | 50.72 |
| | 115 | 19.03 | 31.28 | 42.48 | 50.35 |
| | 135 | 18.87 | 31.01 | 42.14 | 49.95 |
| | 155 | 18.68 | 30.70 | 41.75 | 49.51 |
| | 175 | 18.51 | 30.44 | 41.42 | 49.14 |
| | 195 | 18.34 | 30.20 | 41.12 | 48.80 |
| | 215 | 18.17 | 29.96 | 40.83 | 48.46 |
| | 235 | 18.00 | 29.73 | 40.54 | 48.14 |
| | 255 | 17.84 | 29.50 | 40.26 | 47.82 |
| | 275 | 17.68 | 29.28 | 39.99 | 47.52 |
| | 295 | 17.53 | 29.07 | 39.73 | 47.23 |
| | 315 | 17.38 | 28.87 | 39.48 | 46.94 |
| | 335 | 17.24 | 28.67 | 39.24 | 46.66 |
| | 355 | 17.10 | 28.48 | 39.00 | 46.39 |
| | 375 | 16.97 | 28.30 | 38.76 | 46.12 |
| | 395 | 16.84 | 28.11 | 38.54 | 45.86 |
| | 415 | 16.71 | 27.93 | 38.31 | 45.60 |
| | 435 | 16.59 | 27.76 | 38.08 | 45.35 |
| | 455 | 16.46 | 27.59 | 37.87 | 45.10 |
| | 475 | 16.35 | 27.42 | 37.65 | 44.86 |
| | 495 | 16.23 | 27.25 | 37.44 | 44.62 |
| | 515 | 16.11 | 27.08 | 37.23 | 44.37 |
| | 535 | 16.00 | 26.92 | 37.03 | 44.14 |

| | Turbulators | | | | |
|---|---|---|---|---|---|
| | | Reynolds number | | | |
| | | 1946 | 3902 | 5848 | 7310 |
| $x$ (mm) | 5 | 64.84 | 94.9 | 121.8 | 142.1 |
| | 15 | 39.18 | 55.54 | 71.35 | 83.58 |
| | 25 | 29.13 | 42.84 | 57.27 | 67.85 |
| | 35 | 24.75 | 38.3 | 51.91 | 61.44 |
| | 45 | 23.15 | 37.53 | 50.58 | 59.57 |
| | 55 | 23.73 | 39.39 | 52.98 | 62.22 |
| | 65 | 25.45 | 41.69 | 53.69 | 61.59 |
| | 75 | 25.2 | 40.2 | 51.25 | 58.39 |
| | 85 | 24.26 | 38.4 | 49.29 | 56.36 |
| | 95 | 24.1 | 38.35 | 49.7 | 57.13 |
| | 105 | 24.5 | 39.78 | 51.93 | 59.84 |
| | 115 | 25.13 | 40.8 | 51.97 | 59.01 |
| | 135 | 24.25 | 38.53 | 49.13 | 55.89 |
| | 155 | 23.78 | 38.32 | 49.82 | 57.26 |
| | 175 | 24.23 | 39.17 | 49.92 | 56.67 |
| | 195 | 22.96 | 36.82 | 47.72 | 54.78 |
| | 215 | 23.4 | 38.31 | 49.96 | 57.45 |
| | 235 | 22.97 | 36.89 | 47.26 | 53.86 |
| | 255 | 22.58 | 36.75 | 47.97 | 55.25 |
| | 275 | 23.02 | 37.57 | 48.14 | 54.78 |
| | 295 | 21.88 | 35.42 | 46.09 | 53.02 |
| | 315 | 22.26 | 36.73 | 48.11 | 55.43 |
| | 335 | 21.9 | 35.49 | 45.69 | 52.2 |
| | 355 | 21.52 | 35.33 | 46.32 | 53.48 |
| | 375 | 21.94 | 36.08 | 46.45 | 53.03 |
| | 395 | 20.9 | 34.1 | 44.57 | 51.4 |
| | 415 | 21.26 | 35.35 | 46.51 | 53.73 |
| | 435 | 20.92 | 34.18 | 44.21 | 50.66 |
| | 455 | 20.59 | 34.04 | 44.81 | 51.84 |
| | 475 | 20.96 | 34.74 | 44.95 | 51.45 |
| | 495 | 20.03 | 32.95 | 43.26 | 50.02 |
| | 515 | 20.34 | 34.05 | 44.98 | 52.09 |
| | 535 | 20.02 | 32.94 | 42.83 | 49.2 |

## Average turbulator numerical Nusselt numbers

| | Reynolds number: | 1946 | | 3902 | | 5848 | | 7310 | |
|---|---|---|---|---|---|---|---|---|---|
| $d$ (mm) | $G$ (mm) | Nu | Enhancement factor | Nu | Enhancement factor | Nu | Enhancement factor | Nu | Enhancement factor |
| 0.5 | 0.25 | 18.95 | 1.114 | 32.86 | 1.159 | 44.88 | 1.156 | 53.33 | 1.155 |
| 0.5 | 0.5 | 19.49 | 1.146 | 33.03 | 1.165 | 44.90 | 1.156 | 53.13 | 1.150 |
| 0.5 | 1 | 19.87 | 1.168 | 33.05 | 1.166 | 44.51 | 1.147 | 51.82 | 1.122 |
| 0.5 | 1.5 | 19.71 | 1.159 | 32.59 | 1.150 | 43.62 | 1.124 | 50.71 | 1.098 |
| 0.5 | 2 | 19.47 | 1.145 | 32.32 | 1.140 | 43.14 | 1.111 | 50.07 | 1.084 |
| 0.5 | 3 | 19.07 | 1.121 | 31.83 | 1.123 | 42.62 | 1.098 | 49.65 | 1.075 |
| 0.5 | 4 | 18.87 | 1.109 | 31.61 | 1.115 | 42.60 | 1.097 | 50.08 | 1.084 |
| 1 | 0.25 | 22.22 | 1.306 | 37.67 | 1.329 | 50.39 | 1.298 | 57.75 | 1.250 |
| 1 | 0.5 | 21.93 | 1.289 | 36.54 | 1.289 | 48.15 | 1.240 | 55.37 | 1.199 |
| 1 | 1 | 21.87 | 1.286 | 35.76 | 1.262 | 46.48 | 1.197 | 53.38 | 1.156 |
| 1 | 2 | 21.05 | 1.238 | 33.99 | 1.199 | 43.97 | 1.133 | 50.48 | 1.093 |
| 1 | 3 | 20.59 | 1.210 | 33.47 | 1.180 | 43.78 | 1.128 | 51.40 | 1.113 |
| 1 | 4 | 20.29 | 1.193 | 33.36 | 1.177 | 44.41 | 1.144 | 52.27 | 1.132 |
| 1.5 | 0.25 | 24.39 | 1.434 | 39.92 | 1.408 | 51.20 | 1.319 | 58.46 | 1.266 |
| 1.5 | 0.5 | 23.61 | 1.388 | 37.96 | 1.339 | 49.10 | 1.265 | 56.54 | 1.224 |
| 1.5 | 1 | 22.47 | 1.321 | 36.11 | 1.274 | 46.93 | 1.209 | 54.14 | 1.172 |
| 1.5 | 2 | 21.81 | 1.282 | 34.72 | 1.225 | 44.85 | 1.155 | 51.68 | 1.119 |
| 1.5 | 3 | 21.45 | 1.261 | 34.31 | 1.210 | 45.09 | 1.161 | 52.78 | 1.143 |
| 1.5 | 4 | 21.14 | 1.243 | 34.50 | 1.217 | 46.31 | 1.193 | 54.88 | 1.188 |
| 2 | 0.25 | 26.08 | 1.533 | 41.60 | 1.467 | 53.85 | 1.387 | 61.91 | 1.341 |
| 2 | 0.5 | 25.44 | 1.496 | 39.56 | 1.396 | 50.91 | 1.311 | 59.05 | 1.278 |
| 2 | 0.75 | 24.46 | 1.438 | 38.67 | 1.364 | 49.70 | 1.280 | 57.26 | 1.240 |
| 2 | 1 | 23.78 | 1.398 | 37.49 | 1.322 | 48.48 | 1.249 | 56.12 | 1.215 |
| 2 | 1.5 | 23.32 | 1.371 | 36.72 | 1.295 | 47.05 | 1.212 | 54.07 | 1.171 |
| 2 | 2 | 22.89 | 1.346 | 35.90 | 1.266 | 46.87 | 1.207 | 53.58 | 1.160 |
| 2 | 3 | 22.65 | 1.331 | 36.12 | 1.274 | 47.72 | 1.229 | 56.10 | 1.215 |
| 2 | 4 | 22.51 | 1.323 | 36.61 | 1.291 | 49.27 | 1.269 | 58.64 | 1.270 |

## Average turbulator numerical pressure drop

| | | Pressure drop (Pa) | |
|---|---|---|---|
| | | Reynolds number | |
| $d$ (mm) | $G$ (mm) | 1946 | 7310 |
| 1 | 0.25 | 41.95 | 395.344 |
| 1 | 1 | 53.42 | 456.48 |
| 1 | 2 | 60.88 | 491.78 |
| 1 | 3 | 65.5 | 521.85 |
| 1 | 4 | 66.32 | 532.13 |
| 1.5 | 0.25 | 54.53 | 495.93 |
| 1.5 | 0.5 | 59.47 | 519.35 |
| 1.5 | 1 | 67.27 | 556.17 |
| 1.5 | 2 | 77 | 609.51 |
| 1.5 | 3 | 82.56 | 652.84 |
| 1.5 | 4 | 82.06 | 664.05 |
| 2 | 0.25 | 73.8 | 664.14 |
| 2 | 1 | 88.53 | 702.86 |
| 2 | 1.5 | 96.13 | 736.57 |
| 2 | 2 | 102.06 | 784.5 |
| 2 | 3 | 108.77 | 837.89 |
| 2 | 4 | 107.19 | 846.68 |